Universidade de Évora
2009

Cristina Maria Mendes Andrade

The Large-scale Empirical Forcing Function

186 125

Orientador: Professor Doutor João Alexandre Medina Corte-Real
Co-Orientador: Professor Doutor João Carlos Andrade Santos

℘

A todos os que tornaram este trabalho uma realidade quero expressar o meu agradecimento. Em especial ao meu orientador Professor Doutor Corte-Real e ao meu co-orientador Professor Doutor João Santos pela confiança, disponibilidade amiga e atenção dispensadas.

Ao colega e amigo Professor Doutor João Patrício pela sua sempre pronta colaboração nas enumeras peripécias informáticas e também como responsável pelo C^3 do Instituto Politécnico de Tomar, sem o qual não teria sido possível realizar a enorme parte computacional deste trabalho. Ao amigo Professor Doutor Joaquim Pinto pelas palavras de estímulo e colaboração. A todos os colegas da área pelo seu apoio.

Aos estimados arguentes e membros do júri pelos seus valorosos comentários e sugestões.

Agradeço ainda à minha família e amigos pelo encorajamento e apoio nas horas de maior desânimo.

Resumo

A Equação média temporal da vorticidade potencial do fluxo atmosférico em coordenadas isobáricas pode incluir explicitamente um termo (interno) atmosférico forçador do fluxo perturbado. De facto, desprezando nesta equação de balanço os termos não lineares, este forçamento pode ser expresso matematicamente por uma única função denominada Função Empírica Forçadora (EFF), correspondente à derivada material da vorticidade potencial média temporal. Mais, a EFF pode ser decomposta na soma de sete componentes, que individualmente representam mecanismos forçadores de natureza diferente. Estes mecanismos incluem as componentes diabáticas associadas com o forçamento radiativo, a libertação de calor latente e dissipação pelo atrito, bem como, componentes relacionadas com os transportes transientes perturbados de entalpia e momento linear. Todos estes factores quantificam o papel das perturbações transientes no forçamento da circulação atmosférica. Com o objectivo de compreender a importância da EFF no diagnóstico das anomalias de larga-escala da circulação atmosférica, é analisada a relação entre a EFF e a ocorrência de cristas anticiclónicas intensas na zona Este do Atlântico Norte, consideradas frequentemente precursoras de secas na zona Oeste da Península Ibérica. Para tais eventos, o padrão da EFF apresenta no Atlântico Norte uma clara estrutura dipolar; forçamento ciclónico (anti-ciclónico) de vorticidade potencial no sentido ascendente (descendente) da crista anormalmente intensa. Os resultados apontam igualmente para uma maior relevância das componentes que se relacionam com processos diabáticos. Por último, estes resultados enfatizam a relevância da EFF no diagnóstico de anomalias de larga-escala, e fornecem igualmente uma melhor compreensão das interacções entre os diferentes mecanismos físicos.

Abstract

The time-mean potential vorticity equation of the atmospheric flow on isobaric surfaces can explicitly include an atmospheric (internal) forcing term of the eddy flow. In fact, neglecting some non-linear terms in this balance equation, this forcing can be mathematically expressed as a single function, called Empirical Forcing Function (EFF), which is equal to the material derivative of the time-mean potential vorticity. Furthermore, the EFF can be decomposed as a sum of seven components, each one representing a forcing mechanism of different nature. These mechanisms include diabatic components associated with the radiative forcing, latent heat release and frictional dissipation, and components related to transient eddy transports of heat and momentum. All these factors quantify the role of the transient eddies in forcing the atmospheric circulation. In order to assess the relevance of the EFF in diagnosing large-scale anomalies in the atmospheric circulation, the relationship between the EFF and the occurrence of strong anticyclonic ridges over the Eastern North Atlantic is analysed, which are often precursors of severe droughts over Western Iberia. For such events, the EFF pattern depicts a clear dipolar structure over the North Atlantic; cyclonic (anticyclonic) forcing of potential vorticity is found upstream (downstream) of the anomalously strong ridges. Results also show that the most significant components are related to the diabatic processes. Lastly, these results highlight the relevance of the EFF in diagnosing large-scale anomalies, also providing some insight into their interaction with different physical mechanisms.

Resumo da Tese

Portugal encontra-se localizado no extremo ocidental da Europa, na Península Ibérica. Dada a sua localização o regime de precipitação é altamente variável e caracteriza-se por uma grande sazonalidade. A precipitação máxima ocorre durante o Inverno (Dezembro a Fevereiro), sendo embora de destacar as contribuições do final de Outono e início da Primavera. Consequentemente, os Invernos extremamente secos ou extremamente chuvosos tendem a ter um forte impacto na disponibilidade de água. Deste modo, grandes deficits de precipitação são frequentemente precursores de secas severas e extremas. Devido a esta vulnerabilidade, com um grande impacto ambiental, económico e social, é de grande importância entender os mecanismos de larga-escala que se encontram ligados à ocorrência destas secas. É pois com base neste objectivo que o estudo descrito neste trabalho se baseia.

O fluxo médio temporal da atmosfera pode ser considerado como um regime forçado que se encontra condicionado por diversos factores, tais como, fontes e sumidouros de entalpia, orografia e contrastes térmicos à superfície. Contudo, as perturbações do escoamento médio temporal induzem fluxos locais transientes de entalpia e momento linear que são elementos importantes nos mecanismos forçadores da circulação geral atmosférica. De facto, estas perturbações são essenciais para a compreensão do ciclo da energética da atmosfera, dado serem responsáveis pela transformação contínua da energia potencial disponível média zonal em energia potencial disponível das perturbações, que por sua vez, por processos baroclínicos se transforma em energia cinética perturbada que se converte por processos barotrópicos em energia cinética média zonal do movimento, consequência de processos de dissipação ligados ao atrito.

A vorticidade potencial é frequentemente utilizada em estudos diagnósticos da circulação atmosférica, sendo comummente escrita na sua formulação original, em superfícies isentrópicas, mas também podendo ser referida a um sistema de coordenadas em que a coordenada vertical é a pressão (sistema p). A formulação matemática da equação da vorticidade potencial em coordenadas isobáricas é revisitada no primeiro capítulo. Após algumas aproximações matemáticas obtém-se uma versão linearizada daquela equação, onde os vários termos forçadores são explicitados e representados individualmente. O termo forçador da vorticidade potencial assimétrica é expresso como uma única função, designada por Função Forçadora Empírica (EFF). Esta função pode ser decomposta numa soma de sete componentes que representam diferentes contribuições físicas (associadas a processos diabáticos e de transportes perturbados de entalpia e momento linear) para o termo forçador total da equação de balanço. Este desenvolvimento segue a formulação original devida a Saltzman. Por forma a ilustrar

a aplicabilidade da EFF no diagnóstico de anomalias atmosféricas de larga-escala, um '*case study*' é apresentado no terceiro capítulo deste trabalho, focando o estabelecimento de cristas de altas pressões sobre o Atlântico Norte. A influência das cristas de altas pressões intensas no Atlântico Norte no sistema atmosférico das latitudes médias, é previamente analisado.

Os deficits severos de precipitação em Portugal estão relacionados com padrões anómalos da circulação atmosférica de larga-escala no Atlântico Norte. A intensificação das perturbações de larga-escala levam a condições atmosféricas que não são favoráveis ao estabelecimento de mecanismos geradores de precipitação em Portugal. Com o objectivo de isolar padrões anómalos de larga-escala sobre o Atlântico Norte, em particular cristas anticiclónicas intensas a Oeste da Península Ibérica, foram considerados um conjunto de seis Invernos extremamente secos e seis Invernos extremamente chuvosos. Os compósitos destes Invernos para diversas variáveis e campos atmosféricos foram analisados ao longo da primeira e segunda secções do terceiro capítulo e denominam-se por 'Invernos Secos (Chuvosos)'. As suas anomalias foram analisadas por intermédio da diferença entre os Invernos Secos e os Chuvosos. Na última secção do terceiro capítulo, os campos de seis componentes da Função Forçadora (a componente associada ao atrito (quinta) não é calculada) e a própria Função Forçadora foram analisadas.

Para os Invernos Secos o campo médio do geopotencial apresenta quer aos 500 quer aos 300 hPa uma crista bem definida sobre o Atlântico Norte, enquanto que para os Invernos Chuvosos o padrão é quase zonal. Este resultado é igualmente suportado pelo campo da anomalia da vorticidade potencial. A existência de um eixo quase vertical da anomalia máxima da altura do geopotencial médio zonal para os Invernos Secos sugere uma estrutura quase barotrópica equivalente para aquela crista. A presença de um núcleo quente intenso na crista a Oeste da Península Ibérica é claramente desfavorável para a ocorrência de precipitação em Portugal. Esta crista intensa bloqueia por um lado, a propagação para leste dos sistemas frontais provenientes do Atlântico, levando a um desvio para Nordeste do '*storm track*' no Atlântico Norte. Por outro lado, a sua estrutura barotrópica equivalente, leva a uma clara diferenciação entre os jactos subtropical e polar. O jacto subtropical sofre nas latitudes médias uma separação em dois ramos na zona Este da América do Norte. Esta separação é acompanhada por uma intensificação da componente meridional da circulação média troposférica, intensificação normalmente acompanhada de bloqueio na vizinhança das Ilhas Britânicas. Os transportes de entalpia e de humidade específica apresentam um desvio para Nordeste nos Invernos Secos. Este desvio é igualmente observado nos padrões da taxa de precipitação e água precipitável, contrastando com o padrão quase zonal dos Invernos Chuvosos. As regiões de intensidade máxima dos transportes de entalpia estão concentradas nas zonas preferenciais do '*storm track*', sugerindo ainda o desvio dos transportes de humidade, o bloqueio dos sistemas transientes pela crista intensa. Também o padrão dos transportes zonais de momento linear está em concordância com a presença de uma crista anticiclónica intensa nos Invernos Secos.

A Função Forçadora Empírica é aplicada como ferramenta de diagnóstico das perturbações estacionárias de larga-escala associadas à ocorrência de cristas anticiclónicas intensas no Atlântico Norte, consideradas como precursoras da ocorrência de secas severas na zona Oeste da Península Ibérica. Os resultados mostram, que o padrão da EFF é dinamicamente coerente com a configuração do campo do geopotencial. Para os Invernos em estudo, o padrão da forçadora apresenta uma estrutura dipolar sobre o Atlântico Norte contribuindo para a manutenção de vorticidade potencial ciclónica (anticiclónica) na região ascendente (descendente) da crista anticiclónica anormalmente intensa. A análise individual das componentes da EFF revelou que de entre as seis componentes calculadas, a componente mais importante ao longo da troposfera é a primeira. Esta componente está associada ao aquecimento diabático, excluindo-se o calor latente. Contudo, a componente associada ao calor latente (segunda componente) é igualmente importante na baixa troposfera, enquanto os fluxos horizontais transientes de entalpia (terceira componente) e de momento linear (sexta componente) são importantes na alta troposfera. Estas componentes quando comparadas com as associadas aos fluxos verticais (quarta e sétima componentes) são claramente dominantes em magnitude. Deste modo, numa primeira aproximação o padrão da EFF pode ser estimado por intermédio da primeira componente. Numa segunda aproximação, a estimativa da EFF pode ser melhorada na baixa (alta) troposfera por intermédio da inclusão da segunda (terceira e sexta) componente.

Na interpretação dos padrões da EFF algumas considerações devem ser tidas em conta. Embora alguns processos internos estejam incluídos na definição da EFF, os mecanismos forçadores externos da circulação atmosférica, tais como os efeitos topográficos, os fluxos diabáticos na camada limite não são incorporados nesta definição. De facto, estes processos só podem ser incluídos como condições fronteira. Tendo em consideração que a formulação da EFF deriva da equação da vorticidade potencial média temporal sobre um período relativamente longo de tempo (ie, uma estação), a análise da EFF só permite um diagnóstico das condições dinâmicas, não podendo ser utilizada no estudo da geração (desenvolvimento) das anomalias. Nesta análise só se pode afirmar que a EFF (ou componente da EFF) pode ou não contribuir para a manutenção de uma perturbação estacionária específica. Mesmo tendo em consideração as limitações referidas, a análise efectuada por intermédio da EFF permite compreender as diferentes contribuições dos processos atmosféricos internos que mantêm as anomalias médias temporais axialmente assimétricas do fluxo atmosférico.

Contents

List of Figures xv

List of Tables xxv

List of Symbols xxvii

1 Introduction 1

2 Data and Methodology 5
- 2.1 Theoretical development of the Empirical Forcing Function 5
  - 2.1.1 Potential Vorticity 5
  - 2.1.2 Fundamental equations and deduction of the Empirical Forcing Function 6
  - 2.1.3 Empirical Forcing Function components 11
- 2.2 Data and methodology 13

3 Results 19
- 3.1 Dynamical mechanisms of the North Atlantic atmospheric circulation: preliminary analysis 19
  - 3.1.1 Precipitation rate and Precipitable water 19
  - 3.1.2 Sea level pressure 22
  - 3.1.3 Mean Geopotential height 24
  - 3.1.4 Storm Track 29
  - 3.1.5 Potential temperature 30
  - 3.1.6 Horizontal transports of enthalpy 31
  - 3.1.7 Horizontal transports of momentum 34
  - 3.1.8 Horizontal transports of humidity 37
  - 3.1.9 Wind fields and the jet stream 40
- 3.2 Dynamical analysis of the precursors of the EFF components 44
  - 3.2.1 Horizontal and vertical divergences of enthalpy 44
  - 3.2.2 Horizontal and vertical divergences of humidity 49
  - 3.2.3 Rates of heat addition 54
  - 3.2.4 Vorticity fields 56
- 3.3 Empirical Forcing Function: A Case Study 62
  - 3.3.1 The first and second components of the EFF 62

3.3.2 The third and fourth components of the EFF 66
3.3.3 The sixth and seventh components of the EFF 69
3.3.4 The Empirical Forcing Function 72

4 Discussion and Conclusions **77**

References **81**

Index **90**

List of Figures

2.1 Geographical extension of the Euro-Atlantic sector 14
2.2 Map of Portugal and station's locations (from Mapping Specialists, Lda). . . 15

3.1 Winter composite of the precipitation rates (shading) in 10^{-5} mm.day^{-1} in the North Atlantic sector between 20°N-80°N and 100°W-40°E for (a) dry winters, (b) wet winters, and (c) winter climatology. 20
3.2 Difference of the precipitation rates between dry and wet winters (contours) in 10^{-5} mm.day^{-1} and the corresponding p-values of the Student's t-test (shading) in the North Atlantic sector between 20°N-80°N and 100°W-40°E. 21
3.3 Winter composite of the precipitable water (shading) in mm in the North Atlantic sector between 20°N-80°N and 100°W-40°E for (a) dry winters, (b) wet winters, and (c) winter climatology. 22
3.4 Difference of the precipitable water between dry and wet winters (contours) in mm and the corresponding p-values of the Student's t-test (shading) in the North Atlantic sector between 20°N-80°N and 100°W-40°E. 22
3.5 Winter composite of the mean sea level pressure (shading) in 10^2 Pa in the North Atlantic sector between 20°N-80°N and 100°W-40°E for (a) dry winters, (b) wet winters, and (c) winter climatology. 23
3.6 Difference of the mean sea level pressure between dry and wet winters (contours) in 10^2 Pa and the corresponding p-values of the Student's t-test (shading) in the North Atlantic sector between 20°N-80°N and 100°W-40°E. 23
3.7 Winter composite of the mean geopotential field in gpm at 300 hPa over the Northern Hemisphere between 20°N-85°N for (a) dry winters, and (b) wet winters. 24
3.8 Difference of the mean geopotential field between dry and wet winters (contours) in gpm at 300 hPa and the corresponding p-values of the Student's t-test (shading) over the Northern Hemisphere between 20°N-85°N. 25
3.9 Cross-section of the zonal-mean (60°W-0°E) winter composite of the mean geopotential field in gpm over the Northern Hemisphere sector between 0°N-85°N for (a) dry winters, and (b) wet winters. 25
3.10 Cross-section of the zonal-mean (60°W-0°E) difference of the mean geopotential field between dry and wet winters (contours) in gpm and the corresponding p-values of the Student's t-test (shading) over the Northern Hemisphere between 0°N-85°N. 26

3.11 Cross-section of the zonal-mean (60^oW-0^oE) difference of the mean geopotential field and its hemispheric mean (shading) in gpm and the corresponding winter mean omega-vertical velocity (contours) in Pa.s^{-1} over the Northern Hemisphere between 0^oN-85^oN for (a) dry winters, and (b) wet winters. . . . 26

3.12 Cross-section of the zonal-mean (60^oW-0^oE) difference of the mean geopotential field and its hemispheric mean (contours) in gpm and the corresponding p-values of the Student's t-test (shading) over the Northern Hemisphere between 0^oN-85^oN. 27

3.13 EOF1 of the mean geopotential field in the North Atlantic sector between 20^oN-85^oN and 100^oW-40^oE for (a) dry winters (90.3% explained variance), (b) wet winters (90.3% explained variance), and (c) dry-wet winters (90.0% explained variance), and the corresponding mean geopotential field in 10^2 gpm at 300 hPa 27

3.14 Chronogram of the normalized PC1 of the dry-wet winters mean geopotential field in 10^2 gpm in the North Atlantic sector between 20^oN-85^oN and 100^oW-40^oE. 28

3.15 Mean geopotential field obtained from PC1 in the North Atlantic sector between 20^oN-85^oN and 100^oW-40^oE for the (a) positive composite, and (b) negative composite. 28

3.16 Winter composite of the storm track (shading) in gpm at 500 hPa, and the corresponding mean geopotential height field (contours) in 10^2 gpm in the North Atlantic sector between 20^oN-85^oN and 100^oW-40^oE for (a) dry winters, (b) wet winters, (c) winter climatology, and (d) the difference between dry and wet winters. 29

3.17 Cross-sections of the mean-meridional (60^oW-0^oE) potential temperature in K in the Northern Hemisphere between 0^oN-85^oN for (a) dry winters, and (b) wet winters. 30

3.18 Cross-section of the mean-meridional (60^oW-0^oE) difference of the potential temperature between dry and wet winters (contours) in K and the corresponding p-values of the Student's t-test (shading) over the Northern Hemisphere between 0^oN-85^oN. 31

3.19 Winter composite of the total horizontal transports of enthalpy in 10^2 K.m.s^{-1} at 300 hPa in the North Atlantic sector between 20^oN-80^oN and 100^oW-40^oE for (a) dry winters, and (b) wet winters. Shading represents the intensity of the fluxes, and arrows represent the horizontal fluxes. 32

3.20 Difference of the total horizontal transports of enthalpy between dry and wet winters (contours) in 10^2 K.m.s^{-1} at 300 hPa and the corresponding p-values of the Student's t-test (shading) in the North Atlantic sector between 20^oN-80^oN and 100^oW-40^oE. 33

3.21 Winter composite of the transient horizontal transports of enthalpy in K.m.s^{-1} at 300 hPa in the North Atlantic sector between 20^oN-80^oN and 100^oW-40^oE for (a) dry winters, and (b) wet winters. Shading represents the intensity of the fluxes, and arrows represent the horizontal fluxes. 34

3.22 Difference of the transient horizontal transports of enthalpy between dry and wet winters (contours) in K.m.s^{-1} at 300 hPa and the corresponding p-values of the Student's t-test (shading) in the North Atlantic sector between 20^oN-80^oN and 100^oW-40^oE. 34

3.23 Winter composite of the horizontal convergence of the transports of enthalpy in K.s^{-1} at 300 hPa in the North Atlantic sector between 20°N-80°N and 100°W-40°E for (a) dry winters, and (b) wet winters. Shading represents the intensity of the fluxes, and arrows represent the horizontal fluxes. 35
3.24 Winter composite total horizontal transports of zonal momentum in 10^{2} m^{2}.s^{-2} at 300 hPa in the North Atlantic sector between 20°N-80°N and 100°W-40°E for (a) dry winters, and (b) wet winters. Shading represents the intensity of the fluxes, and arrows represent the horizontal fluxes. 35
3.25 Difference of the total horizontal transports of momentum between dry and wet winters (contours) in 10^{2} m^{2}.s^{-2} at 300 hPa and the corresponding p-values of the Student's t-test (shading) in the North Atlantic sector between 20°N-80°N and 100°W-40°E. 35
3.26 Winter composite transient horizontal transports of zonal momentum in 10^{2} m^{2}.s^{-2} at 300 hPa in the North Atlantic sector between 20°N-80°N and 100°W-40°E for (a) dry winters, and (b) wet winters. Shading represents the intensity of the fluxes, and arrows represent the horizontal fluxes. 36
3.27 Difference of the transient horizontal transports of momentum between dry and wet winters (contours) in 10^{2} m^{2}.s^{-2} at 300 hPa and the corresponding p-values of the Student's t-test (shading) in the North Atlantic sector between 20°N-80°N and 100°W-40°E. 36
3.28 Winter composite of the mean kinetic energy (contours) and transient mean kinetic energy (shading) in 10^{1} m^{2}.s^{-2} at 300 hPa in the North Atlantic sector between 20°N-80°N and 100°W-40°E for (a) dry winters, and (b) wet winters. 37
3.29 Difference of the transient mean kinetic energy between dry and wet winters (contours) in 10^{1} m^{2}.s^{-2} at 300 hPa and the corresponding p-values of the Student's t-test (shading) in the North Atlantic sector between 20°N-80°N and 100°W-40°E. 37
3.30 Winter composite of the total horizontal transports of specific humidity in 10^{-1} g.kg^{-1}.m.s^{-1} at 300 hPa in the North Atlantic sector between 0°N-80°N and 100°W-40°E for (a) dry winters, and (b) wet winters. Shading represents the intensity of the fluxes, and arrows represent the horizontal fluxes. 38
3.31 Difference of the total horizontal transports of specific humidity between dry and wet winters (contours) in 10^{-1} g.kg^{-1}.m.s^{-1} at 300 hPa and the corresponding p-values of the Student's t-test (shading) in the North Atlantic sector between 0°N-80°N and 100°W-40°E. 38
3.32 Winter composite of the transient-eddy horizontal transports of specific humidity in 10^{-1} g.kg^{-1}.m.s^{-1} at 300 hPa in the North Atlantic sector between 0°N-80°N and 100°W-40°E for (a) dry winters, and (b) wet winters. Shading represents the intensity of the fluxes, and arrows represent the horizontal fluxes. 39
3.33 Difference of the transient-eddy horizontal transports of specific humidity between dry and wet winters (contours) in 10^{-1} g.kg^{-1}.m.s^{-1} at 300 hPa and the corresponding p-values of the Student's t-test (shading) in the North Atlantic sector between 0°N-80°N and 100°W-40°E. 39
3.34 Winter composite of the specific humidity advection in 10^{-1} g.kg^{-1}.day^{-1} at 300 hPa in the North Atlantic sector between 20°N-60°N and 80°W-20°E for (a) dry winters, and (b) wet winters. Shading represents the intensity of the fluxes, and arrows represent the horizontal fluxes. 40

3.35 General configuration of the polar and subtropical jet streams (from NASA). 40
3.36 Winter composite of the streamlines and wind intensity in $m.s^{-1}$ at 300 hPa over the Northern Hemisphere between 0°N-85°N for (a) dry winters, and (b) wet winters. Shading represents the wind intensity, and arrows represent the streamlines. 41
3.37 Difference of the streamlines and wind intensity between dry and wet winters (contours) in $m.s^{-1}$ at 300 hPa and the corresponding p-values of the Student's t-test (shading) over the Northern Hemisphere between 0°N-85°N. 41
3.38 Cross-sections of the winter composites of the zonal-mean wind component in $m.s^{-1}$ at 300 hPa in the North Atlantic sector between 0°N-85°N and 60°W-0°E for (a) dry winters, and (b) wet winters. 42
3.39 Difference of the winter composites of the zonal-mean wind component between dry and wet winters (contours) in $m.s^{-1}$ at 300 hPa and the corresponding p-values of the Student's t-test (shading) in the North Atlantic sector between 0°N-85°N and 60°W-0°E. 42
3.40 Winter composite of the vertically-averaged (500 – 300 hPa) mean horizontal divergence of enthalpy (shading) in 10^{-4} $m.K.s^{-2}$ and the corresponding mean geopotential field (contours) in 10^2 gpm in the North Atlantic sector between 20°N-65°N and 100°W-40°E for (a) dry winters, (b) wet winters, and (c) winter climatology. 44
3.41 Difference of the vertically-averaged (500–300 hPa) mean horizontal divergence of enthalpy between dry and wet winters (contours) in 10^{-4} $m.K.s^{-2}$ and the corresponding p-values of the Student's t-test (shading) in the North Atlantic sector between 20°N-80°N and 100°W-40°E. 45
3.42 Zonal cross-sections of the meridional-mean (20°N-60°N) of the mean horizontal divergence of enthalpy at 500 – 300 hPa in 10^{-5} $m.K.s^{-2}$ in the North Atlantic between 100°W-20°E for (a) dry winters, and (b) wet winters, and at 1000 – 500 hPa in 10^{-4} $m.K.s^{-2}$ for (c) dry winters, and (d) wet winters. . . 45
3.43 Zonal cross-section of the difference of the meridional-mean (20°N-60°N) of the mean horizontal divergence of enthalpy between dry and wet winters (contours) at (a) 500 – 300 hPa in 10^{-5} $m.K.s^{-2}$, and (b) 1000 – 500 hPa in 10^{-4} $m.K.s^{-2}$ and the corresponding p-values of the Student's t-test (shading) in the North Atlantic sector between 100°W-20°E. 45
3.44 Winter composite of the vertically-averaged (500 – 300 hPa) mean vertical transports of enthalpy (shading) in 10^{-4} $m.K.s^{-2}$ and the corresponding mean geopotential field (contours) in 10^2 gpm in the North Atlantic sector between 20°N-65°N and 100°W-40°E for (a) dry winters, (b) wet winters, and (c) winter climatology. 46
3.45 Difference of the vertically-averaged (500 – 300 hPa) mean vertical transports of enthalpy between dry and wet winters (contours) in 10^{-4} $m.K.s^{-2}$ and the corresponding p-values of the Student's t-test (shading) in the North Atlantic sector between 20°N-80°N and 100°W-40°E. 46
3.46 Winter composite of the vertically-averaged (500–300 hPa) mean eddy-horizontal divergence of enthalpy (shading) in 10^{-6} $m.K.s^{-2}$ and the corresponding mean geopotential field (contours) in 10^2 gpm in the North Atlantic sector between 20°N-80°N and 100°W-40°E for (a) dry winters, (b) wet winters, and (c) winter climatology. 47

3.47 Difference of the vertically-averaged (500 – 300 hPa) mean eddy-horizontal divergence of enthalpy between dry and wet winters (contours) in 10^{-6} m.K.s^{-2} and the corresponding p-values of the Student's t-test (shading) in the North Atlantic sector between 20°N-80°N and 100°W-40°E. 47

3.48 Winter composite of the vertically-averaged (500 – 300 hPa) mean eddy-vertical transports of enthalpy (shading) in 10^{-6} m.K.s^{-2} and the corresponding mean geopotential field (contours) in 10^{2} gpm in the North Atlantic sector between 20°N-80°N and 100°W-40°E for (a) dry winters, (b) wet winters, and (c) winter climatology. 48

3.49 Difference of the vertically-averaged (500 – 300 hPa) mean eddy-vertical transports of enthalpy between dry and wet winters (contours) in 10^{-6} m.K.s^{-2} and the corresponding p-values of the Student's t-test (shading) in the North Atlantic sector between 20°N-80°N and 100°W-40°E. 48

3.50 Winter composite of the vertically-averaged (500 – 300 hPa) mean divergence of enthalpy (shading) in 10^{-5} m.K.s^{-2} and the corresponding mean geopotential field (contours) in 10^{2} gpm in the North Atlantic sector between 20°N-65°N and 100°W-40°E for (a) dry winters, (b) wet winters, and (c) winter climatology. 48

3.51 Difference of the vertically-averaged (500 – 300 hPa) mean divergence of enthalpy between dry and wet winters (contours) in 10^{-5} m.K.s^{-2} and the corresponding p-values of the Student's t-test (shading) in the North Atlantic sector between 20°N-80°N and 100°W-40°E. 49

3.52 Winter composite of the vertically-averaged (500 – 300 hPa) mean horizontal divergence of humidity (shading) in 10^{-10} m.s^{-2} and the corresponding mean geopotential field (contours) in 10^{2} gpm in the North Atlantic sector between 20°N-80°N and 100°W-40°E for (a) dry winters, (b) wet winters, and (c) winter climatology. 49

3.53 Difference of the vertically-averaged (500 – 300 hPa) mean horizontal divergence of humidity between dry and wet winters (contours) in 10^{-10} m.s^{-2} and the corresponding p-values of the Student's t-test (shading) in the North Atlantic sector between 20°N-80°N and 100°W-40°E. 50

3.54 Zonal cross-sections of the meridional-mean (20°N-60°N) of the mean horizontal divergence of humidity at 500 – 300 hPa in 10^{-10} m.s^{-2} in the North Atlantic between 100°W-20°E for (a) dry winters, and (b) wet winters, and at 1000 – 500 hPa in 10^{-9} m.s^{-2} for (c) dry winters, and (d) wet winters. 50

3.55 Zonal cross-section of the difference of the meridional-mean (20°N-60°N) horizontal divergence of humidity between dry and wet winters (contours) at (a) 500 – 300 hPa in 10^{-10} m.s^{-2}, and at (b) 1000 – 500 hPa in 10^{-9} m.s^{-2} and the corresponding p-values of the Student's t-test (shading) in the North Atlantic sector between 100°W-20°E. 51

3.56 Winter composite of the vertically-averaged (500 – 300 hPa) mean vertical transports of humidity (shading) in 10^{-10} m.s^{-2} and the corresponding mean geopotential field (contours) in 10^{2} gpm in the North Atlantic sector between 20°N-80°N and 100°W-40°E for (a) dry winters, (b) wet winters, and (c) winter climatology. 51

3.57 Difference of the vertically-averaged (500 – 300 hPa) mean vertical transports of humidity between dry and wet winters (contours) in 10^{-10} m.s^{-2} and the corresponding p-values of the Student's t-test (shading) in the North Atlantic sector between 20°N-80°N and 100°W-40°E. 52

3.58 Winter composite of the vertically-averaged (500–300 hPa) mean eddy-horizontal divergence of humidity (shading) in 10^{-10} m.s^{-2} and the corresponding mean geopotential field (contours) in 10^2 gpm in the North Atlantic sector between 20°N-80°N and 100°W-40°E for (a) dry winters, (b) wet winters, and (c) winter climatology. 52

3.59 Difference of the vertically-averaged (500 – 300 hPa) mean eddy-horizontal divergence of humidity between dry and wet winters (contours) in 10^{-10} m.s^{-2} and the corresponding p-values of the Student's t-test (shading) in the North Atlantic sector between 20°N-80°N and 100°W-40°E. 53

3.60 Winter composite of the vertically-averaged (500–300 hPa) mean eddy-vertical transports of humidity (shading) in 10^{-10} m.s^{-2}, and the corresponding mean geopotential field (contours) in 10^2 gpm in the North Atlantic sector between 20°N-80°N and 100°W-40°E for (a) dry winters, (b) wet winters, and (c) winter climatology. 53

3.61 Difference of the vertically-averaged (500 – 300 hPa) mean eddy-vertical transports of humidity between dry and wet winters (contours) in 10^{-10} m.s^{-2} and the corresponding p-values of the Student's t-test (shading) in the North Atlantic sector between 20°N-80°N and 100°W-40°E. 53

3.62 Winter composite of the vertically-averaged (500–300 hPa) mean divergence of humidity (shading) in 10^{-10} m.s^{-2}, and the corresponding mean geopotential field (contours) in 10^2 gpm in the North Atlantic sector between 20°N-80°N and 100°W-40°E for (a) dry winters, (b) wet winters, and (c) winter climatology. 54

3.63 Difference of the vertically-averaged (500 – 300 hPa) mean divergence of humidity between dry and wet winters (contours) in 10^{-10} m.s^{-2} and the corresponding p-values of the Student's t-test (shading) in the North Atlantic sector between 20°N-80°N and 100°W-40°E. 54

3.64 Winter composite of the vertically-averaged (500 – 300 hPa) total rate of heat addition (shading) in 10^{-2} J.s^{-1}, and the corresponding mean geopotential field (contours) in 10^2 gpm in the North Atlantic sector between 20°N-80°N and 100°W-40°E for (a) dry winters, (b) wet winters, and (c) winter climatology. 55

3.65 Difference of the vertically-averaged (500 – 300 hPa) total rate of heat addition between dry and wet winters (contours) in 10^{-2} J.s^{-1} and the corresponding p-values of the Student's t-test (shading) in the North Atlantic sector between 20°N-80°N and 100°W-40°E. 55

3.66 Winter composite of the vertically-averaged (500 – 300 hPa) rate of heat addition, per unit mass, due to condensation (shading) in 10^{-3} J.s^{-1}, and the corresponding mean geopotential field (contours) in 10^2 gpm in the North Atlantic sector between 20°N-80°N and 100°W-40°E for (a) dry winters, (b) wet winters, and (c) winter climatology. 56

3.67 Difference of the vertically-averaged (500 – 300 hPa) rate of heat addition, per unit mass, due to condensation between dry and wet winters (contours) in 10^{-3} J.s^{-1} and the corresponding p-values of the Student's t-test (shading) in the North Atlantic sector between 20°N-80°N and 100°W-40°E. 56

3.68 Winter composite of the vertical component of the relative vorticity (shading) in 10^{-6} s^{-1} at 300 hPa in the North Atlantic sector between 0°N-80°N and 100°W-40°E for (a) dry winters, (b) wet winters, and (c) winter climatology. . 57

3.69 Difference of the vertical component of the relative vorticity between dry and wet winters (contours) in 10^{-6} s^{-1} at 300 hPa and the corresponding p-values of the Student's t-test (shading) in the North Atlantic sector between 0°N-80°N and 100°W-40°E. 57

3.70 Winter composite of the mean meridional gradient of the absolute vorticity (shading) in 10^{-11} $m^{-1}.s^{-1}$ at 300 hPa in the North Atlantic sector between 0°N-80°N and 100°W-40°E for (a) dry winters, and (b) wet winters. 58

3.71 Difference of the mean meridional gradient of the absolute vorticity between dry and wet winters (contours) in 10^{-11} $m^{-1}.s^{-1}$ at 300 hPa and the corresponding p-values of the Student's t-test (shading) in the North Atlantic sector between 0°N-80°N and 100°W-40°E. 58

3.72 Winter composite of the absolute vorticity (shading) in 10^{-5} s^{-1} at 300 hPa and the corresponding mean geopotential field (contours) in 10^2 gpm in the North Atlantic sector between 0°N-80°N and 100°W-40°E for (a) dry winters, (b) wet winters, and (c) difference between dry and wet winters. 59

3.73 Difference of the absolute vorticity between dry and wet winters (contours) in 10^{-5} s^{-1} at 300 hPa and the corresponding p-values of the Student's t-test (shading) in the North Atlantic sector between 0°N-80°N and 100°W-40°E. . 59

3.74 Winter composite of the potential vorticity (shading) in 10^{-4} s^{-1} at 300 hPa and the corresponding mean geopotential field (contours) in 10^2 gpm in the North Atlantic sector between 20°N-80°N and 100°W-40°E for (a) dry winters, (b) wet winters, and (c) difference between dry and wet winters. 59

3.75 Difference of the potential vorticity between dry and wet winters (contours) in 10^{-4} s^{-1} at 300 hPa and the corresponding p-values of the Student's t-test (shading) in the North Atlantic sector between 20°N-80°N and 100°W-40°E. . 60

3.76 Winter composite of the potential vorticity advection (shading) in 10^{-10} s^{-1} at 300 hPa and the corresponding mean geopotential field (contours) in 10^2 gpm in the North Atlantic sector between 20°N-80°N for (a) dry winters, and (b) wet winters. 60

3.77 Difference of the potential vorticity advection between dry and wet winters (contours) in 10^{-10} s^{-1} at 300 hPa and the corresponding p-values of the Student's t-test (shading) in the North Atlantic sector between 20°N-80°N and 100°W-40°E. 61

3.78 Zonal cross-sections of the difference of the meridional-mean (35°N-50°N) of the first EFF component pattern between dry and wet winters for the North Atlantic between 80°W-20°E at (a) 500 – 300 hPa in 10^{-10} s^{-2}, and at (b) 1000 – 500 hPa in 10^{-9} s^{-2}. 63

3.79 Vertically-averaged (500 – 300 hPa) first EFF component (shading)in 10^{-10} s^{-2} and the corresponding mean geopotential field (contours) in 10^2 gpm in the North Atlantic between 30°N-60°N and 80°W-20°E for (a) dry winters (b) wet winters (c) winter climatology, and (d) difference between dry and wet winters. 63

3.80 Vertically-averaged (1000 – 500 hPa) first EFF component (shading) in 10^{-9} s^{-2} and the corresponding mean geopotential field (contours) in 10^2 gpm in the North Atlantic between 30°N-60°N and 80°W-20°E for (a) dry winters (b) wet winters (c) winter climatology, and (d) difference between dry and wet winters. 64

3.81 Difference of the vertically-averaged first EFF component between dry and wet winters (contours) at (a) 500 – 300 hPa in 10^{-10} s^{-2}, and at (b) 1000 – 500 hPa in 10^{-9} s^{-2} and the corresponding p-values of the Student's t-test (shading) in the North Atlantic between 30°N-60°N and 80°W-20°E. 64

3.82 Zonal cross-sections of the difference of the meridional-mean (35°N-50°N) of the second EFF component pattern between dry and wet winters in the North Atlantic between 80°W-20°E at (a) 500 – 300 hPa in 10^{-11} s^{-2}, and at (b) 1000 – 500 hPa layer in 10^{-10} s^{-2}. 65

3.83 Vertically-averaged (500–300 hPa) second EFF component (shading) in 10^{-11} s^{-2} and the corresponding mean geopotential field (contours) in 10^2 gpm in the North Atlantic between 30°N-60°N and 80°W-20°E for (a) dry winters (b) wet winters (c) winter climatology, and (d) difference between dry and wet winters. 65

3.84 Difference of the vertically-averaged (500 – 300 hPa) second EFF component between dry and wet winters (contours) in 10^{-11} s^{-2}, and the corresponding p-values of the Student's t-test (shading) in the North Atlantic between 30°N-60°N and 80°W-20°E. 66

3.85 Zonal cross-sections of the difference of the meridional-mean (35°N-50°N) of the third EFF component pattern between dry and wet winters in the North Atlantic between 80°W-20°E at (a) 500 – 300 hPa in 10^{-11} s^{-2}, and at (b) 1000 – 500 hPa in 10^{-11} s^{-2}. 66

3.86 Vertically-averaged (500 – 300 hPa) third EFF component (shading) in 10^{-11} s^{-2} and the corresponding mean geopotential field (contours) in 10^2 gpm in the North Atlantic between 30°N-60°N and 80°W-20°E for (a) dry winters (b) wet winters (c) winter climatology, and (d) difference between dry and wet winters. 67

3.87 Vertically-averaged (1000–500 hPa) third EFF component (shading) in 10^{-11} s^{-2} and the corresponding mean geopotential field (contours) in 10^2 gpm in the North Atlantic between 30°N-60°N and 80°W-20°E for (a) dry winters (b) wet winters (c) winter climatology, and (d) difference between dry and wet winters. 68

3.88 Difference of the vertically-averaged third EFF component between dry and wet winters (contours) at (a) 500 – 300 hPa in 10^{-11} s^{-2}, and at (b) 1000 – 500 hPa in 10^{-11} s^{-2} and the corresponding p-values of the Student's t-test (shading) in the North Atlantic between 30°N-60°N and 80°W-20°E. 68

3.89 Zonal cross-sections of the difference of the meridional-mean (35°N-50°N) of the fourth EFF component pattern between dry and wet winters in the North Atlantic between 80°W-20°E at (a) 500 – 300 hPa in 10^{-12} s^{-2}, and at (b) 1000 – 500 hPa in 10^{-11} s^{-2}. 69

3.90 Vertically-averaged (500–300 hPa) fourth EFF component (shading) in 10^{-11} s^{-2} and the corresponding mean geopotential field (contours) in 10^2 gpm in the North Atlantic between 30°N-60°N and 80°W-20°E for (a) dry winters (b) wet winters (c) winter climatology, and (d) difference between dry and wet winters. 69

3.91 Zonal cross-sections of the difference of the meridional-mean (35^{o}N-50^{o}N) of the sixth EFF component pattern between dry and wet winters in the North Atlantic between 80^{o}W-20^{o}E at (a) 500 – 300 hPa in 10^{-11} s^{-2}, and at (b) 1000 – 500 hPa in 10^{-11} s^{-2}. 70
3.92 Vertically-averaged (500 – 300 hPa) sixth EFF component (shading) in 10^{-11} s^{-2} and the corresponding mean geopotential field (contours) in 10^2 gpm in the North Atlantic between 30^{o}N-60^{o}N and 80^{o}W-20^{o}E for (a) dry winters (b) wet winters (c) winter climatology, and (d) difference between dry and wet winters. 70
3.93 Zonal cross-sections of the difference in the meridional-mean (35^{o}N-50^{o}N) of the seventh EFF component pattern between dry and wet winters in the North Atlantic between 80^{o}W-20^{o}E at (a) 500 – 300 hPa in 10^{-12} s^{-2}, and at (b) 1000 – 500 hPa in 10^{-12} s^{-2}. 71
3.94 Vertically-averaged (500 – 300 hPa) seventh EFF component (shading) in 10^{-12} s^{-2} and the corresponding mean geopotential field (contours) in 10^2 gpm in the North Atlantic between 30^{o}N-60^{o}N and 80^{o}W-20^{o}E for (a) dry winters (b) wet winters (c) winter climatology, and (d) difference between dry and wet winters. 71
3.95 Vertically-averaged (500 – 300 hPa) sum of second, third and sixth EFF component (shading) in 10^{-11} s^{-2} and the corresponding mean geopotential field (contours) in 10^2 gpm in the North Atlantic between 30^{o}N-60^{o}N and 80^{o}W-20^{o}E for (a) dry winters (b) wet winters (c) winter climatology, and (d) difference between dry and wet winters. 72
3.96 Vertically-averaged (1000 – 500 hPa) sum of second, third and sixth EFF component (shading) in 10^{-11} s^{-2} and the corresponding mean geopotential field (contours) in 10^2 gpm in the North Atlantic between 30^{o}N-60^{o}N and 80^{o}W-20^{o}E for (a) dry winters (b) wet winters (c) winter climatology, and (d) difference between dry and wet winters. 73
3.97 Zonal cross-sections of the difference of the meridional-mean (35^{o}N-50^{o}N) of the EFF pattern between dry and wet winters in the North Atlantic between 80^{o}W-20^{o}E at (a) 500 – 300 hPa in 10^{-10} s^{-2}, and at (b) 1000 – 500 hPa in 10^{-9} s^{-2}. 74
3.98 Vertically-averaged (500 – 300 hPa) EFF (shading) in 10^{-10} s^{-2} and the corresponding mean geopotential field (contours) in 10^2 gpm in the North Atlantic between 30^{o}N-60^{o}N and 80^{o}W-20^{o}E for (a) dry winters (b) wet winters (c) winter climatology, and (d) difference between dry and wet winters. 74
3.99 Vertically-averaged (1000 – 500 hPa) EFF (shading) in 10^{-9} s^{-2} and the corresponding mean geopotential field (contours) in 10^2 gpm in the North Atlantic between 30^{o}N-60^{o}N and 80^{o}W-20^{o}E for (a) dry winters (b) wet winters (c) winter climatology, and (d) difference between dry and wet winters. 75
3.100 Difference of the vertically-averaged EFF between dry and wet winters (contours) at (a) 500 – 300 hPa in 10^{-10} s^{-2}, and at (b) 1000 – 500 hPa in 10^{-9} s^{-2}, and the corresponding p-values of the Student's t-test (shading) in the North Atlantic between 30^{o}N-60^{o}N and 80^{o}W-20^{o}E. 75

List of Tables

2.1 List of variables and respective units 14
2.2 List of the geographical locations of the four Portuguese stations used in this study 15
2.3 List of the extremely dry and extremely wet winters 15

List of Symbols

The following notation was used in the text.

λ	Longitude
φ	Latitude
p	Pressure
t	Time
$a = 6.371 \times 10^6$ m	Mean radius of the earth
$\Omega = 7.292 \times 10^{-5}$ rad s^{-1}	Angular velocity of the Earth
$g = 9.80$ ms^{-2}	Apparent gravity acceleration
$u = a \cos\varphi \frac{d\lambda}{dt}$	Zonal wind component
$v = a\frac{d\varphi}{dt}$	Meridional wind component
$\mathbf{v} = u\mathbf{i} + u\mathbf{j}$	Horizontal wind vector
$\omega = \frac{dp}{dt}$	Omega vertical wind component
$\Phi = gz$	Geopotential
T	Air temperature
$c_p = 1004$ J kg^{-1} K^{-1}	Specific heat at constant pressure
$R = 287$ J kg^{-1} K^{-1}	Gas constant for dry air
F_λ	Specific zonal frictional force
F_φ	Specific meridional frictional force
q	Specific humidity
$\dot{q}_F$	Specific diabatic heating rate due to conduction and friction
$\dot{q}_R$	Specific diabatic heating rate due to radiation
$\dot{q}_L$	Specific diabatic heating rate due to latent heat release
Γ	Static stability parameter
Θ	Empirical forcing function
ff_n	n-th component of the empirical forcing function
$Q = \dot{q} = \dot{q}_F + \dot{q}_R + \dot{q}_L$	Total rate of heat addition
Π	Potential vorticity
η	Absolute vorticity
ζ	Relative vorticity
f	Planetary vorticity

P	Precipitation rate
E	Evaporation rate
R_0	Surface runoff
W	Precipitable water
θ	Potential temperature
$\overline{(\ )}$	Time-mean
$(\ )' = (\ ) - \overline{(\ )}$	Departure from time-mean
$[\ ]$	Zonal-mean
$(\ )^* = (\ ) - [\ ]$	Departure from zonal-mean
$\{\ \}$	Areolar-mean

Chapter 1
Introduction

Portugal is located in the western portion of Europe in the Iberian Peninsula between 37°-42°N and 6.5°-9.5°W. Due to its location the precipitation regime is highly unbalanced and is characterized by a strong seasonal behaviour. The maximum rainfall occurs in winter (December to February; hereafter DJF), despite the contributions of late autumn and early spring. As a result, extremely wet or extremely dry winters tend to have strong impacts on water availability and management practices [García-Herrera et al., 2007]. Severe precipitation deficits in Portugal are largely related to anomaly patterns in the North Atlantic large-scale atmospheric flow. The dependence of winter precipitation on the North Atlantic Oscillation (NAO), and baroclinic wave activity associated to circulation weather types or weather regimes has been the subject of several studies [Corte-Real et al., 1995; Fernandez et al., 2003; Goodess and Jones, 2002; Santos et al., 2005, 2007a; Trigo and Da Camara, 2000; Ulbrich and Christoph, 1999a; Wang, 2002; Wiin-Nielsen, 2003].

Severe precipitation deficits in Portugal result from a enhancement of the stationary wave pattern of the atmospheric large-scale circulation over the North Atlantic. This enhancement of the large-scale stationary eddies leads to atmospheric conditions that are clearly unfavourable to the establishment of rain-generating mechanisms over Portugal. Therefore severe precipitation deficits are often precursors of severe or extreme drought episodes. Due to this vulnerability, with great environmental, economical and social significance, it is of great importance to better understand the large-scale mechanisms that are linked to the occurrence of such droughts.

The temporal mean flow of the atmosphere can be regarded as a forced regime that is conditioned by several factors, such as, heat release, topography and surface thermal contrasts [Trewartha and Horn, 1980; Wallace and Hobbs, 2006]. However, eddies embedded in the time-mean flow induce local transient heat and momentum fluxes that are key forcing mechanisms of the general atmospheric circulation. In fact, such eddies are essential for explaining the energy cycle of the atmosphere, as they continuously transform zonal-mean available potential energy into eddy and zonal-mean kinetic energy of the flow that is ultimately dissipated through cascading frictional dissipation processes [e.g., Peixoto and Oort, 1992]. The key role played by the eddy transports concerning the maintenance of large-scale atmospheric anomalies through their interaction with the zonal-mean flow has been already demonstrated in many previous studies [e.g., Andrade et al., 2008c, d; Black, 1998; Edmon et al., 1980;

Holopainen et al., 1982; Hoskins and Valdes, 1990; Lau and Nath, 1991; Rodríguez-Puebla et al., 2001; Santos and Corte-Real, 2006; Santos and Leite, 2009a].

Vorticity is a widely used property when describing the dynamical characteristics of the flow, and its equation is commonly used for diagnosis and prediction of fluid motions [Holton, 2004; Hoskins et al., 1985]. Potential vorticity is a quantity that combines vorticity and static stability and verifies an invertibility principle that can be stated as follows [Bluestein, 1993]: if the distribution of potential vorticity is known, then vorticity, static stability and wind field can also be determined, providing the required boundary conditions and a balance condition. The concept of potential vorticity is often used in the study of the atmospheric circulation, particularly when considering an adiabatic frictionless flow [Salby and Roger, 1996]; in this case it is materially conserved (local rate of change is entirely balanced by advection). Therefore, potential vorticity is commonly written in its original formulation on isentropic surfaces [Ertel, 1962]. However, many subsequent studies have also used the potential vorticity defined on isobaric surfaces [e.g., Hartmann, 1977; Lau and Wallace, 1979]. In fact, potential vorticity is also materially conserved when using the quasi-geostrophic formulation of the potential vorticity under the quasi-geostrophic assumptions and following the geostrophic wind on an isobaric surface [Holton, 2004].

The mathematical formulation of the potential vorticity equation in isobaric coordinates is revisited in this study. Some mathematical approximations and rearrangements are undertaken so as to obtain a linearised version of the balance equation, where various forcing terms are explicitly and independently represented. The forcing term of the stationary-eddy (asymmetric) potential vorticity balance is expressed as a single function, called the Empirical Forcing Function (hereafter EFF). This function can be in turn decomposed as a sum of seven components that represent different physical contributions (associated with diabatic processes and transient eddy enthalpy and momentum transports) to the total forcing term of the balance equation. This development closely follows the original formulation undertaken by Saltzman [1962]. In order to illustrate the applicability of the EFF in diagnosing large-scale atmospheric anomalies, a case study focusing on the establishment of ridges over the Eastern North Atlantic is presented. As already mentioned, previous studies have shown that the frequency and persistence of such events are often associated with droughts over western Iberia [García-Herrera et al., 2007; Hanson et al., 2007; Santos and Leite, 2009a; Santos et al., 2007a].

The influence of those enhanced ridges over the Eastern North Atlantic in the mid-latitude weather systems is also tested here. In fact, these systems have their origin in processes predicted under the theory of baroclinic instability and their development is closely associated with the above referred forcing mechanisms. Such extra-tropical migratory systems follow a path in the belt of the prevailing westerly winds and derive their existence and growth from the conversion of available potential energy to kinetic energy by reducing the temperature gradients, lifting mid-latitude warm air and sinking cold polar air [Charney, 1947; Eady, 1949]. They also play a central role in the angular momentum budget of the atmosphere and are primarily responsible for maintaining the westerlies against surface friction [Peixoto and Oort, 1992]. One common measure of synoptic activity is the 'storm track', which Blackmon [1976] defined as the standard deviation of the bandpass-filtered (2-6 days) variability at 500 hPa, thus representing the sequence of westward propagating upper air troughs and ridges as the tropospheric counterparts of surface cyclones and high pressure systems [Blackmon et al., 1984a, b; Wallace and Gutzler, 1981; Wallace et al., 1988]. This variable has been widely used to quantify synoptic activity, both for observational and model data sets [e.g., Chang and Fu, 2002; Chang, 2009; Hoskins and Valdes, 1990; Stephenson and Held, 1993; Ulbrich et al., 2008; Yin, 2005].

In this study, the objectives are two-fold. First, it is intended to present the mathematical development of the EFF, and secondly, to demonstrate its relevance in diagnosing large-scale anomaly patterns by considering a pertinent case study.

The structure of this thesis is as follows:

in Section 2 it is presented

> the theoretical and mathematical development of the EFF and its components,
>
> as well as, the data and methodologies;

in Section 3 results obtained for the selected case study are presented, in the following sequence:

> first, the dynamical mechanisms of the North Atlantic circulation are discussed,
>
> second, the dynamical analysis of the precursors fields of the EFF components, is carried out and
>
> third, the Empirical Forcing Function is analysed

finally, in Section 4 the main results are discussed.

Chapter 2
Data and Methodology

2.1 Theoretical development of the Empirical Forcing Function

2.1.1 Potential Vorticity

The main purpose of dynamic meteorology is to achieve a better understanding of the large-scale atmospheric motions in terms of its physical governing laws. In this framework, the concept of potential vorticity is useful in the study of the atmospheric circulation, mainly when considering an adiabatic flow or isentropic coordinates [Salby and Roger, 1996], where this quantity is materially conserved (local rate of change entirely balanced by advection). Since for extratropical synoptic-scale motions, the horizontal velocity is nearly geostrophic, this approximation is called as quasi-geostrophic. The mathematical development of the Empirical Forcing Function (EFF) is achieved from the development of the potential vorticity equation, therefore a brief description of this concept is undertaken since there are different forms of potential vorticity.

The vorticity is defined as the rotational part of the velocity vector

$$\zeta = \nabla \times \mathbf{c}. \tag{2.1}$$

For the quasi-horizontal motions of the atmosphere, the component of the planetary vorticity normal to the earth's surface is the Coriolis parameter

$$f = 2\Omega \sin\varphi. \tag{2.2}$$

The vertical component of the absolute vorticity is given by

$$\eta = f + \zeta_z, \tag{2.3}$$

where $\zeta_z = \frac{\partial v}{\partial x} - \frac{\partial u}{\partial y}$ is the vertical component of the relative vorticity.

Many studies make use of the original formulation of the potential vorticity by Ertel [1962] in θ coordinates, i.e., the Ertel's potential vorticity

$$\Pi_\theta = (\zeta_\theta + f)\left(-\frac{\partial \theta}{\partial p}\right) \tag{2.4}$$

where ζ_θ is the relative vorticity defined on isentropic surfaces, θ potential temperature and p pressure. This definition is also considered a good approximation for adiabatic and frictionless flow.

It can be shown that the isentropic potential vorticity can also be written in the form

$$\Pi_v = -g\left(\zeta_\theta + f\right)\frac{\partial\theta}{\partial p} \tag{2.5}$$

where g is the acceleration of gravity.

In several studies on large-scale general circulation [Hartmann, 1977; Lau and Wallace, 1979; Savijärvi, 1978] the relative vorticity defined on pressure surfaces ζ_p was used instead of ζ_θ. Therefore from equation (2.4) the following definition in isobaric coordinates can be achieved

$$\Pi_p = \left(\zeta_p + f\right)\left(-\frac{\partial\theta}{\partial p}\right). \tag{2.6}$$

Since the meteorological measurements are commonly defined at constant pressure levels, the application of this equation is straightforward. There are other approximations of the potential vorticity, however, as mentioned before the potential vorticity is the basis of the EFF development. Under the isobaric quasi-geostrophic assumption

$$\left(\frac{\partial}{\partial t} + \mathbf{v}_g \bullet \nabla\right)\Pi = 0 \tag{2.7}$$

the potential vorticity is defined as

$$\Pi = \eta + f\frac{\partial}{\partial p}\left(\frac{T}{\Gamma}\right) \tag{2.8}$$

where $f\frac{\partial}{\partial p}\left(\frac{T}{\Gamma}\right)$ is the normalized static stability designated as stretching vorticity, and Γ the static stability given by

$$\Gamma = \frac{T}{\theta}\frac{\partial\theta}{\partial p} = \frac{\partial T}{\partial p} - \frac{RT}{C_p p}. \tag{2.9}$$

After the analysis of Γ in the different isobaric levels, constant values of the static stability for each level were used. This procedure was also followed by Saltzman [1962] and Savijärvi [1978].

2.1.2 Fundamental equations and deduction of the Empirical Forcing Function

The mathematical development of the Empirical Forcing Function involves fundamental equations and definitions and it was first presented by Saltzman [1962]. The following notation is used in the development; $\overline{(\ )}$ represents the time-mean, $(\ )'$ time-mean departure, $[\ ]$ represents the zonal-mean and $(\ )^*$ the zonal-mean departure. Considering the time-mean primitive equations of motion in the p-system, after Reynolds decomposition the zonal momentum balance equation can be written as

$$\frac{\partial \overline{u}}{\partial t} + \overline{\mathbf{v}} \bullet \nabla \overline{u} + \overline{\omega} \frac{\partial \overline{u}}{\partial p} = \left(f + \tfrac{\overline{u} \tan \varphi}{a}\right) \overline{v} - \tfrac{1}{a \cos \varphi} \tfrac{\partial \overline{\Phi}}{\partial \lambda} + \overline{X} \tag{2.10}$$

and the meridional momentum balance equation as

$$\frac{\partial \overline{v}}{\partial t} + \overline{\mathbf{v}} \bullet \nabla \overline{v} + \overline{\omega} \frac{\partial \overline{v}}{\partial p} = -\left(f + \tfrac{\overline{u} \tan \varphi}{a}\right) \overline{u} - \tfrac{1}{a} \tfrac{\partial \overline{\Phi}}{\partial \varphi} + \overline{Y} \tag{2.11}$$

from which the variables, $\overline{X}$ and $\overline{Y}$, can be defined as

$$\overline{X} = \overline{F_\lambda} - \left(\frac{1}{a \cos \varphi} \frac{\partial \overline{u'^2}}{\partial \lambda} + \frac{1}{a \cos \varphi} \frac{\partial}{\partial \varphi} \overline{u'v'} \cos \varphi + \frac{\partial \overline{u'\omega'}}{\partial p} - \frac{\overline{u'v'} \tan \varphi}{a}\right), \tag{2.12}$$

$$\overline{Y} = \overline{F_\varphi} - \left(\frac{1}{a \cos \varphi} \frac{\partial \overline{u'v'}}{\partial \lambda} + \frac{1}{a \cos \varphi} \frac{\partial}{\partial \varphi} \overline{v'^2} \cos \varphi + \frac{\partial \overline{v'\omega'}}{\partial p} + \frac{\overline{u'^2} \tan \varphi}{a}\right). \tag{2.13}$$

The time-mean energy equation, also after Reynolds decomposition, can be written as follows

$$\frac{\partial \overline{T}}{\partial t} + \overline{\mathbf{v}} \bullet \nabla \overline{T} + \overline{\omega} \frac{\partial \overline{T}}{\partial p} = \frac{R}{p c_p} \overline{\omega} \overline{T} + \overline{Q} \tag{2.14}$$

the variable $\overline{Q}$ can be defined as

$$\overline{Q} = \tfrac{\overline{\dot{q}_R + \dot{q}_F + \dot{q}_L}}{c_p} - \left(\frac{1}{a \cos \varphi} \frac{\partial}{\partial \lambda} \overline{u'T'} + \frac{1}{a \cos \varphi} \frac{\partial}{\partial \varphi} \overline{v'T'} \cos \varphi + \frac{\partial}{\partial p} \overline{\omega'T'} - \frac{R}{p c_p} \overline{\omega'T'}\right) \tag{2.15}$$

where $\dot{q}_R$, $\dot{q}_F$ and $\dot{q}_L$ are, respectively, the rates of heat addition per unit mass due to radiation, conduction and friction and to latent heat release. Now consider the time-mean continuity equation

$$\frac{\partial \overline{\omega}}{\partial p} + \nabla \bullet \overline{\mathbf{v}} = 0, \tag{2.16}$$

and the time-mean hydrostatic equation

$$\frac{\partial \overline{\Phi}}{\partial p} = -\frac{R\overline{T}}{p}. \tag{2.17}$$

From the potential vorticity definition (2.8), after applying the local time-derivative, the next equality is obtained

$$\frac{\partial \Pi}{\partial t} = \frac{\partial \eta}{\partial t} + \frac{\partial}{\partial t}\left(f \frac{\partial}{\partial p}\left(\frac{T}{\Gamma}\right)\right) \tag{2.18}$$

as well as the following vectorial decomposition

$$\mathbf{v} \bullet \nabla \Pi = \mathbf{v} \bullet \nabla \eta + \mathbf{v} \bullet \nabla \left(f \frac{\partial}{\partial p}\left(\frac{T}{\Gamma}\right)\right). \tag{2.19}$$

From the following vorticity equation

$$\frac{\partial \eta}{\partial t} + \mathbf{v} \bullet \nabla \eta + \omega \frac{\partial \eta}{\partial p} + \eta \nabla \bullet \mathbf{v} + \mathbf{k} \nabla \omega \times \frac{\partial \mathbf{v}}{\partial p} - \mathbf{k} \bullet \nabla \times F = 0, \tag{2.20}$$

and adding the terms $\frac{\partial}{\partial t}\left(f\frac{\partial}{\partial p}\left(\frac{T}{\Gamma}\right)\right) + v \bullet \nabla\left(f\frac{\partial}{\partial p}\left(\frac{T}{\Gamma}\right)\right)$ to equation (2.20), the following equality is obtained

$$\begin{aligned}&\tfrac{\partial \eta}{\partial t} + \mathbf{v} \bullet \nabla \eta + \omega \tfrac{\partial \eta}{\partial p} + \eta \nabla \bullet \mathbf{v} + \mathbf{k} \nabla \omega \times \tfrac{\partial \mathbf{v}}{\partial p} - \mathbf{k} \bullet \nabla \times F + \tfrac{\partial}{\partial t}\left(f\tfrac{\partial}{\partial p}\left(\tfrac{T}{\Gamma}\right)\right) + \\ &\quad \mathbf{v} \bullet \nabla\left(f\tfrac{\partial}{\partial p}\left(\tfrac{T}{\Gamma}\right)\right) = \frac{\partial}{\partial t}\left(f\frac{\partial}{\partial p}\left(\frac{T}{\Gamma}\right)\right) + \mathbf{v} \bullet \nabla\left(f\frac{\partial}{\partial p}\left(\frac{T}{\Gamma}\right)\right).\end{aligned} \tag{2.21}$$

The following relations are going to be integrated during the mathematical development of the EFF. Let us considered the absolute vorticity equation, η, from which the next equalities are obtained

$$\begin{aligned}\omega\frac{\partial \eta}{\partial p} &= \omega\frac{\partial(\zeta + f)}{\partial p} \\ &= \omega\frac{\partial \zeta}{\partial p}\end{aligned} \tag{2.22}$$

and

$$\begin{aligned}\eta \nabla \bullet \mathbf{v} &= (\zeta + f)\nabla \bullet \mathbf{v} \\ &= -\zeta\frac{\partial \omega}{\partial p} - f\frac{\partial \omega}{\partial p}.\end{aligned} \tag{2.23}$$

From the potential vorticity definition (2.8) the following conditions are attained

$$\frac{\partial}{\partial t}\left(f\frac{\partial}{\partial p}\left(\frac{T}{\Gamma}\right)\right) = f\frac{\partial}{\partial t}\left(\frac{1}{\Gamma}\frac{\partial T}{\partial p}\right) - f\frac{\partial}{\partial t}\left(\frac{T}{\Gamma^2}\frac{\partial \Gamma}{\partial p}\right), \tag{2.24}$$

$$\mathbf{v} \bullet \nabla \Pi = \mathbf{v} \bullet \nabla \eta + \mathbf{v} \bullet \nabla\left(f\frac{\partial}{\partial p}\left(\frac{T}{\Gamma}\right)\right), \tag{2.25}$$

$$\mathbf{v} \bullet \nabla\left(f\frac{\partial}{\partial p}\left(\frac{T}{\Gamma}\right)\right) = f\mathbf{v} \bullet \nabla\frac{\partial}{\partial p}\left(\frac{T}{\Gamma}\right) + \frac{\partial}{\partial p}\left(\frac{T}{\Gamma}\right)\mathbf{v} \bullet \nabla f, \tag{2.26}$$

and

$$\mathbf{v} \bullet \nabla\left(f\frac{\partial}{\partial p}\left(\frac{T}{\Gamma}\right)\right) = f\mathbf{v} \bullet \nabla\left(\frac{1}{\Gamma}\frac{\partial T}{\partial p}\right) - f\mathbf{v} \bullet \nabla\left(\frac{T}{\Gamma^2}\frac{\partial \Gamma}{\partial p}\right). \tag{2.27}$$

Let us also considered the following equalities

$$\frac{\partial}{\partial p}\left(\frac{T}{\Gamma}\right)\mathbf{v} \bullet \nabla f = -\frac{T}{\Gamma^2}\frac{\partial \Gamma}{\partial p}\mathbf{v} \bullet \nabla f, \tag{2.28}$$

$$f\frac{\partial}{\partial p}\left(\frac{1}{\Gamma}\mathbf{v} \bullet \nabla T\right) = \frac{f}{\Gamma}\frac{\partial \mathbf{v}}{\partial p} \bullet \nabla T + \frac{f}{\Gamma}\mathbf{v} \bullet \frac{\partial}{\partial p}\nabla T - f\mathbf{v} \bullet \nabla\left(\frac{T}{\Gamma^2}\frac{\partial \Gamma}{\partial p}\right), \tag{2.29}$$

$$-\frac{f\mathbf{v}}{\Gamma^2}\frac{\partial}{\partial p}(T \bullet \nabla\Gamma) = -f\frac{\partial}{\partial p}\left(\frac{T}{\Gamma^2}\mathbf{v} \bullet \nabla\Gamma\right) + f\frac{T}{\Gamma^2}\frac{\partial \mathbf{v}}{\partial p} \bullet \nabla\Gamma, \tag{2.30}$$

and

$$\frac{\partial}{\partial p}\left(\frac{T}{\Gamma}\mathbf{v} \bullet \nabla f\right) = f\mathbf{v} \bullet \nabla\left(\frac{1}{\Gamma}\frac{\partial T}{\partial p}\right) - \frac{f}{\Gamma}\mathbf{v} \bullet \frac{\partial}{\partial p}\nabla T. \tag{2.31}$$

From the energy conservation equation (2.14)

$$\omega = \frac{Q}{\Gamma c_p} - \frac{1}{\Gamma}\left(\frac{\partial T}{\partial t} + \mathbf{v} \bullet \nabla T\right). \tag{2.32}$$

Let us remind that from vorticity equation (2.20) the following equality (2.21) was attained

$$\underbrace{\frac{\partial \eta}{\partial t}}_{(2.18)} + \underbrace{\mathbf{v} \bullet \nabla\eta}_{(2.19)} + \omega\frac{\partial \eta}{\partial p} + \eta\nabla \bullet \mathbf{v} + \mathbf{k}\nabla\omega \times \frac{\partial \mathbf{v}}{\partial p} - \mathbf{k} \bullet \nabla \times F +$$

$$\underbrace{\frac{\partial}{\partial t}\left(f\frac{\partial}{\partial p}\left(\frac{T}{\Gamma}\right)\right)}_{(2.18)} + \underbrace{\mathbf{v} \bullet \nabla\left(f\frac{\partial}{\partial p}\left(\frac{T}{\Gamma}\right)\right)}_{(2.19)} = \frac{\partial}{\partial t}\left(f\frac{\partial}{\partial p}\left(\frac{T}{\Gamma}\right)\right) + \mathbf{v} \bullet \nabla\left(f\frac{\partial}{\partial p}\left(\frac{T}{\Gamma}\right)\right).$$

therefore

$$\frac{\partial \Pi}{\partial t} + \mathbf{v} \bullet \nabla\Pi = \frac{\partial}{\partial t}\left(f\frac{\partial}{\partial p}\left(\frac{T}{\Gamma}\right)\right) + \mathbf{v} \bullet \nabla\left(f\frac{\partial}{\partial p}\left(\frac{T}{\Gamma}\right)\right) - \underbrace{\omega\frac{\partial \eta}{\partial p}}_{(2.22)} -$$

$$\underbrace{\eta\nabla \bullet \mathbf{v}}_{(2.23)} - \mathbf{k}\nabla\omega \times \frac{\partial \mathbf{v}}{\partial p} + \mathbf{k} \bullet \nabla \times F \tag{2.33}$$

after substituting the expressions

$$\frac{\partial \Pi}{\partial t} + \mathbf{v} \bullet \nabla\Pi = \underbrace{\frac{\partial}{\partial t}\left(f\frac{\partial}{\partial p}\left(\frac{T}{\Gamma}\right)\right)}_{(2.24)} + \underbrace{\mathbf{v} \bullet \nabla\left(f\frac{\partial}{\partial p}\left(\frac{T}{\Gamma}\right)\right)}_{(2.26)} -$$

$$\omega\frac{\partial \zeta}{\partial p} + \zeta\frac{\partial \omega}{\partial p} + \underbrace{f\frac{\partial \omega}{\partial p}}_{(2.32)} - \mathbf{k}\nabla\omega \times \frac{\partial \mathbf{v}}{\partial p} + \mathbf{k} \bullet \nabla \times F, \tag{2.34}$$

consequently

$$\frac{\partial \Pi}{\partial t} + \mathbf{v} \bullet \nabla\Pi = -f\frac{\partial}{\partial p}\left(\frac{T}{\Gamma^2}\frac{\partial \Gamma}{\partial t}\right) + f\frac{\partial}{\partial p}\left(\frac{1}{\Gamma}\frac{\partial T}{\partial t}\right) + \underbrace{f\mathbf{v} \bullet \nabla\frac{\partial}{\partial p}\left(\frac{T}{\Gamma}\right)}_{(2.27)} +$$

$$\underbrace{\frac{\partial}{\partial p}\left(\frac{T}{\Gamma}\right)\mathbf{v} \bullet \nabla f}_{(2.28)} - \omega\frac{\partial \zeta}{\partial p} + \zeta\frac{\partial \omega}{\partial p} + f\frac{\partial}{\partial p}\left(\frac{Q}{\Gamma}\right) - f\frac{\partial}{\partial p}\left(\frac{1}{\Gamma}\frac{\partial T}{\partial t}\right) -$$

$$\underbrace{f\frac{\partial}{\partial p}\left(\frac{1}{\Gamma}\mathbf{v} \bullet \nabla T\right)}_{(2.29)} - \mathbf{k}\nabla\omega \times \frac{\partial \mathbf{v}}{\partial p} + \mathbf{k} \bullet \nabla \times F, \tag{2.35}$$

from which after some simplifications the next equality is attained

$$\frac{\partial \Pi}{\partial t} + \mathbf{v} \bullet \nabla \Pi = -f \frac{\partial}{\partial p}\left(\frac{T}{\Gamma^2}\frac{\partial \Gamma}{\partial t}\right) + \underbrace{f \mathbf{v} \bullet \nabla \left(\frac{1}{\Gamma}\frac{\partial T}{\partial p}\right)}_{(2.31)} - \underbrace{\frac{f}{\Gamma^2}\mathbf{v} \bullet \frac{\partial T}{\partial p}\nabla \Gamma}_{(2.30)} - \omega \frac{\partial \zeta}{\partial p} +$$
$$\zeta \frac{\partial \omega}{\partial p} + f \frac{\partial}{\partial p}\left(\frac{Q}{\Gamma}\right) - \frac{f}{\Gamma}\frac{\partial \mathbf{v}}{\partial p} \bullet \nabla T - \underbrace{\frac{f}{\Gamma}\mathbf{v} \bullet \frac{\partial}{\partial p}\nabla T}_{(2.31)} - \mathbf{k}\nabla \omega \times \frac{\partial \mathbf{v}}{\partial p} + \mathbf{k} \bullet \nabla \times F, \qquad (2.36)$$

as well as,

$$\frac{\partial \Pi}{\partial t} + \mathbf{v} \bullet \nabla \Pi = -f \frac{\partial}{\partial p}\left(\frac{T}{\Gamma^2}\frac{\partial \Gamma}{\partial t}\right) + \frac{\partial}{\partial p}\left(\frac{T}{\Gamma}\right)\mathbf{v} \bullet \nabla f - f \frac{\partial}{\partial p}\left(\frac{T}{\Gamma^2}\mathbf{v} \bullet \nabla \Gamma\right) + f \frac{T}{\Gamma^2}\frac{\partial \mathbf{v}}{\partial p} \bullet \nabla \Gamma -$$
$$\omega \frac{\partial \zeta}{\partial p} + \zeta \frac{\partial \omega}{\partial p} + f \frac{\partial}{\partial p}\left(\frac{Q}{\Gamma}\right) - \frac{f}{\Gamma}\frac{\partial \mathbf{v}}{\partial p} \bullet \nabla T - \mathbf{k}\nabla \omega \times \frac{\partial \mathbf{v}}{\partial p} + \mathbf{k} \bullet \nabla \times F. \qquad (2.37)$$

After taking the time-mean average, the time-mean potential vorticity equation is then attained

$$\frac{\partial \overline{\Pi}}{\partial t} + \overline{\mathbf{v}} \bullet \nabla \overline{\Pi} = \Theta + \overline{\zeta}\frac{\partial \overline{\omega}}{\partial p} - \overline{\omega}\frac{\partial \overline{\zeta}}{\partial p} - \mathbf{k}\nabla \overline{\omega} \times \frac{\partial \overline{\mathbf{v}}}{\partial p} + \frac{\partial}{\partial p}\left(\frac{\overline{T}}{\overline{\overline{\Gamma}}}\overline{\mathbf{v}} \bullet \nabla f\right) -$$
$$\frac{f}{\overline{\overline{\Gamma}}}\frac{\partial \overline{\mathbf{v}}}{\partial p} \bullet \nabla \overline{T} + f \frac{\overline{T}}{\overline{\overline{\Gamma}}^2}\frac{\partial \overline{\mathbf{v}}}{\partial p} \bullet \nabla \overline{\Gamma} - f \frac{\partial}{\partial p}\left(\frac{\overline{T}}{\overline{\overline{\Gamma}}^2}\overline{\mathbf{v}} \bullet \nabla \overline{\Gamma}\right) - f \frac{\partial}{\partial p}\left(\frac{\overline{T}}{\overline{\overline{\Gamma}}^2}\frac{\partial \overline{\Gamma}}{\partial t}\right), \qquad (2.38)$$

where Θ is defined as

$$\begin{aligned} \Theta &= f \frac{\partial}{\partial p}\left(\frac{\overline{Q}}{\overline{\overline{\Gamma}}}\right) + \mathbf{k} \bullet \nabla \times \overline{F} \\ &= f \frac{\partial}{\partial p}\left(\frac{\overline{Q}}{\overline{\overline{\Gamma}}}\right) + \frac{1}{a \cos \varphi}\left(\frac{\partial \overline{Y}}{\partial \lambda} - \frac{\partial \overline{X}\cos \varphi}{\partial \varphi}\right). \qquad (2.39) \end{aligned}$$

In (2.39), $\overline{Q}$ is the sum of the diabatic heating terms related to transient temperature fluxes, whereas $\overline{X}$ and $\overline{Y}$ are the sum of the frictional dissipative components with the terms related to transient momentum fluxes.

Noting that the second member of equation (2.38) is the sum of Θ with non-linear terms, as follows

$$\begin{aligned} \frac{\partial \overline{\Pi}}{\partial t} + \overline{\mathbf{v}} \bullet \nabla \overline{\Pi} &= f \frac{\partial}{\partial p}\left(\frac{\overline{Q}}{\overline{\overline{\Gamma}}}\right) + \mathbf{k} \bullet \nabla \times \overline{F} + \text{non-linear terms} \\ &= \Theta + \text{non-linear terms}. \qquad (2.40) \end{aligned}$$

Now considering only the stationary-eddy (asymmetric) components in equation (2.38) and neglecting all non-linear asymmetric terms, the equation of the stationary-eddy potential vorticity is obtained

$$\begin{aligned} \frac{\partial \overline{\Pi}^*}{\partial t} &\approx -\left(\overline{\mathbf{v}} \bullet \nabla \overline{\Pi}\right)^* + f \frac{\partial}{\partial p}\left(\frac{\overline{Q}}{\overline{\overline{\Gamma}}}\right)^* + \frac{1}{a \cos \varphi}\left(\frac{\partial \overline{Y}}{\partial \lambda} - \frac{\partial}{\partial \varphi}\overline{X}\cos \varphi\right)^* \\ \frac{\partial \overline{\Pi}^*}{\partial t} &\approx -\left(\overline{\mathbf{v}} \bullet \nabla \overline{\Pi}\right)^* + \Theta^* \qquad (2.41) \end{aligned}$$

where Θ^* is the Empirical Forcing Function (EFF).

According to Saltzman [1962], this approximation is reasonable when means are taken over a sufficiently long time period, such as an entire season. In this case, the term can be interpreted as a forcing term of the stationary-eddy potential vorticity and is also called EFF. Since the local derivative of the stationary-eddy potential vorticity also tends to be neglected when considering an entire season (steady-state), the EFF tends to be balanced by advection, i.e., the advection pattern tends to be in phase opposition with the EFF pattern. Having in mind these assumptions, it should be stressed that the analysis of the EFF is essentially a diagnostic tool, not enabling studies of the development of the anomalies (onset/decay).

It is still worth emphasizing that the external forcing mechanisms of the atmospheric circulation (boundary conditions), such as topographic effects, diabatic fluxes at the lower atmospheric boundary are not incorporated in this definition. In fact, only internal (mechanical and thermal) processes are taken into consideration in the EFF formulation. Since these internal processes interact through positive and negative feedback mechanisms with the mean flow, they cannot be considered as independent forcing entities of the atmospheric flow. For instance, positive eddy feedback mechanisms have shown to play a key role in the reinforcement of teleconnection patterns, such as the North Atlantic Oscillation [Rivière, 2009].

2.1.3 Empirical Forcing Function components

In order to differentiate the contributions of the different processes to the total forcing, the EFF can be expressed as a sum of seven components. In this way,

$$\Theta^* = \sum_{n=1}^{7} ff_n(\lambda, \varphi, p). \tag{2.42}$$

Therefore, regions of positive (negative) values of ff_n represent a cyclonic (anticyclonic) forcing of the stationary-eddy potential vorticity. Moreover, since a local increase in $\overline{\Pi}^*$ is associated with the development of a trough, regions of positive values of ff_n are associated to cyclonic circulation. On the other hand, a local decrease in $\overline{\Pi}^*$ is associated with ridge developments, and therefore associated to anticyclonic circulation. As previously explained, in order to achieve a steady-state atmosphere, the sum of the seven components Θ^* must be in phase opposition with the potential vorticity advections. Therefore, cyclonic vorticity tends to be advected into the negative EFF regions, whereas anticyclonic vorticity tends to be advected into the positive EFF regions under a stationary regime. It should be noted the possibility that large scale potential vorticity anomalies set up without being caused by any underlying forcing mechanism; in such case, under steady conditions, those anomalies will not be advected by the atmospheric flow, with the consequence that they would remain undetected by the present analysis. This possibility deserves further investigation, which falls outside the scope of this study. In the present work it is assumed that the onset of circulations resulting in dry or wet winters in continental Portugal is due to forcing effects which reflect on different patterns of the EFF.

Substituting (2.12), (2.13) and (2.15) in (2.39) and taking the zonal-mean departure the formal breakdown of the EFF (2.42) is achieved The mathematical formulation of each component is as follows:

$$ff_1 = \frac{f}{c_p}\frac{\partial}{\partial p}\left(\frac{\overline{\dot{q}_R + \dot{q}_F}}{\overline{\Gamma}}\right)^* \tag{2.43}$$

is the component associated to friction and diabatic heating,

$$ff_2 = \frac{f}{c_p}\frac{\partial}{\partial p}\left(\frac{\overline{\dot{q}_L}}{\overline{\Gamma}}\right)^* \tag{2.44}$$

is the component associated to latent heat release,

$$ff_3 = -f\frac{\partial}{\partial p}\left(\frac{1}{\overline{\overline{\Gamma}}}\left(\frac{\partial\overline{u'T'}}{\partial\lambda} + \frac{\partial}{\partial\varphi}\overline{v'T'}cos\varphi\right)\right)^* \tag{2.45}$$

is the component associated to the differential divergence of the horizontal transient-eddy transports of enthalpy,

$$ff_4 = -f\frac{\partial}{\partial p}\left(\frac{1}{\overline{\overline{\Gamma}}}\left(\frac{\partial\overline{\omega'T'}}{\partial p} - \frac{R}{c_p p}\overline{\omega'T'}\right)\right)^* \tag{2.46}$$

is the component associated to the differential divergence of the vertical transient-eddy transports of enthalpy,

$$ff_5 = \frac{1}{acos\varphi}\left(\frac{\partial\overline{F}_\varphi}{\partial\lambda} - \frac{\partial\overline{F}_\lambda}{\partial\varphi}cos\varphi\right)^* = (\mathbf{k}.\nabla\times\overline{F})^* \tag{2.47}$$

is the component associated to friction,

$$\begin{aligned} ff_6 &= -\frac{1}{a^2cos\varphi}\left(\frac{1}{cos\varphi}\frac{\partial}{\partial\lambda}\left(\frac{\partial\overline{u'v'}}{\partial\lambda} + \frac{\partial\overline{v'}^2\cos\varphi}{\partial\varphi} + \overline{u'}^2\sin\varphi\right) -\right. \\ &- \left.\frac{\partial}{\partial\varphi}\left(\frac{\partial\overline{u'}^2}{\partial\lambda} + \frac{\partial}{\partial\varphi}\overline{u'v'}cos\varphi - \overline{u'v'}sin\varphi\right)\right)^* \end{aligned} \tag{2.48}$$

is the component associated to the eddy horizontal transports of momentum,

$$ff_7 = -\frac{1}{acos\varphi}\frac{\partial}{\partial p}\left(\frac{\partial\overline{v'\omega'}}{\partial\lambda} - \frac{\partial}{\partial\varphi}\overline{u'\omega'}cos\varphi\right)^* \tag{2.49}$$

is the component associated to the eddy vertical transports of momentum.

For the second component, the rate of heat addition per unit mass due to condensation, $\dot{q}_L$, was calculated indirectly from the water vapour continuity equation,

$$\begin{aligned} \overline{\dot{q}_L} &= -L\left(\frac{\partial\overline{q}}{\partial t} + \overline{\mathbf{v}\bullet\nabla q} + \overline{\omega\frac{\partial q}{\partial p}}\right) \\ &= -L\left(\frac{\partial\overline{q}}{\partial t} + \overline{\nabla\bullet\mathbf{v}q} + \frac{\partial\overline{\omega q}}{\partial p}\right) \approx -L\left(\overline{\nabla\bullet\mathbf{v}q} + \frac{\partial\overline{\omega q}}{\partial p}\right) \\ \overline{\dot{q}_L} &\approx -L\left(\frac{1}{a\cos\varphi}\frac{\partial\overline{uq}}{\partial\lambda} + \frac{1}{a\cos\varphi}\frac{\partial\overline{vq}}{\partial\varphi} + \frac{1}{a\cos\varphi}\frac{\partial\overline{u'q'}}{\partial\lambda} + \frac{1}{a\cos\varphi}\frac{\partial\overline{v'q'}}{\partial\varphi}\cos\varphi + \right. \\ &\left.\frac{\partial\overline{\omega q}}{\partial p} + \frac{\partial\overline{\omega'q'}}{\partial p}\right). \end{aligned} \tag{2.50}$$

For the first component, the sum of the rates of heat addition per unit mass due to radiation and due to conduction and friction $\dot{q}_R$ and $\dot{q}_F$, respectively, were indirectly computed from the energy conservation equation (2.14) and (2.50), following a similar development. As such,

$$\overline{\dot{q}_L + \dot{q}_R + \dot{q}_F} \approx c_p \left(\frac{1}{a\cos\varphi}\frac{\partial \overline{u}\overline{T}}{\partial\lambda} + \frac{1}{a\cos\varphi}\frac{\partial \overline{v}\overline{T}\cos\varphi}{\partial\varphi} + \frac{1}{a\cos\varphi}\frac{\partial \overline{u'T'}}{\partial\lambda} + \right.$$
$$\left. \frac{1}{a\cos\varphi}\frac{\partial \overline{v'T'}\cos\varphi}{\partial\varphi} + \frac{\partial \overline{\omega}\overline{T}}{\partial p} + \frac{\partial \overline{\omega'T'}}{\partial p} - \frac{R}{pc_p}\overline{\omega}\overline{T} - \frac{R}{pc_p}\overline{\omega'T'} \right), \tag{2.51}$$

consequently

$$\overline{\dot{q}_R + \dot{q}_F} = \overline{\dot{q}_L + \dot{q}_R + \dot{q}_F} - \overline{\dot{q}_L}. \tag{2.52}$$

It is worth mentioning that due to the impossibility of obtaining reliable estimates of the fifth component, related to the frictional effects, the EFF considered here is the sum of the remaining six components.

2.2 Data and methodology

The study uses NCEP/NCAR reanalysis [Kistler et al., 2001] for all computations. Originally, this data has a resolution of T62 and is available on a 2.5^o x 2.5^o grid. Only data over the Northern hemisphere and up to 70 hPa is considered in this present study. The selected atmospheric parameters (variables) are listed in Table 2.1. Daily means for the period 1957-2008 (data previous to 1957 is considered less reliable) are computed from the original 6-hourly data. Climate-mean values refer to averages calculated using the standard reference period from 1961 to 1990 [WMO, 1996]. Since the application of the EFF is based on the fundamental assumption that the atmospheric properties (e.g., transient transports) are averaged over a relatively long time period, the time-means in all equations presented in the previous section refer to an entire winter period (DJF). The corresponding departures are then computed on a daily basis after seasonal correction (departures relative to the mean calendar day). All partial derivatives were computed using centered finite differences and one-sided differences at the boundaries.

Although computations were performed for the entire Northern Hemisphere, as winter-mean ridges over the Eastern North Atlantic are the selected illustrative case study, the analyses presented here focus preferentially on a spatial domain over a Euro-Atlantic sector (Fig. 2.1) which can be considered large enough for this study.

Table 2.1: List of variables and respective units

Data (field)	Units
wind components u, v	m.s^{-1}
vertical velocity omega, ω	Pa.s^{-1}
air temperature, T	K
specific humidity, q	Kg.Kg^{-1}
geopotential height, g	gpm
precipitable water, W	Kg.m^{-2}
precipitation rate, R	Kg.m^{-2}.s^{-1}
sea mean level pressure, $MSLP$	Pa

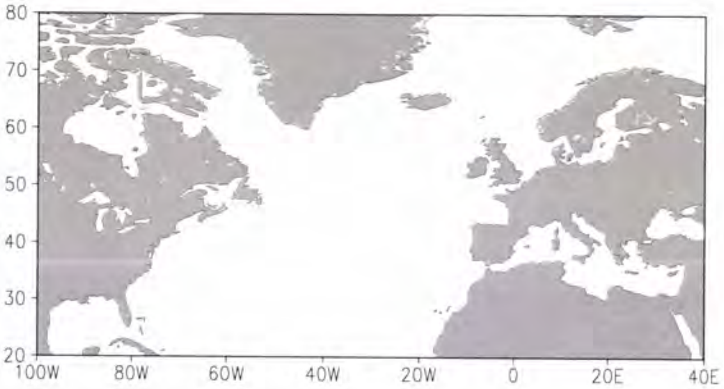

Figure 2.1: Geographical extension of the Euro-Atlantic sector

One main purpose of this study is to illustrate the applicability of the EFF patterns in diagnosing large-scale anomalies and in the identification of the physical forcing mechanisms that explain their occurrence. Aiming at isolating large-scale anomaly patterns over the North Atlantic, in particular strong anticyclonic ridges westwards of Iberia that are associated with severe precipitation deficits over Portugal, a set of six extremely dry and six extremely wet winters were considered from a previous study [Santos et al., 2009b]. In the latter study, a dataset of daily precipitation from ECA (European Climate Assessment & Dataset) [Tank et al., 2002] was used. In particular, area-mean winter precipitation time series from 1945 to 2006, from data recorded at four meteorological stations in Portugal (Table 2.2): Bragança, Porto, Lisboa and Beja (Fig. 2.2), was computed. The accumulated winter precipitation values were computed separately and then the average of the four time series was taken.

Table 2.2: List of the geographical locations of the four Portuguese stations used in this study

Station	Longitude	Latitude	Elevation (m)
Bragança	6°44'W	41°48'N	690
Porto	8°36'W	41°08'N	93
Lisboa	9°09'W	38°43'N	77
Beja	7°52'W	38°01'N	246

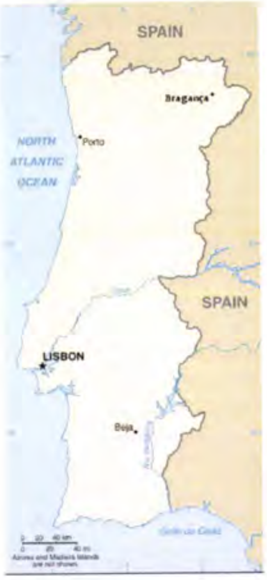

Figure 2.2: Map of Portugal and station's locations (from Mapping Specialists, Lda).

Severe winter precipitation extremes were considered when the total precipitation anomaly was equal to or lower the 10-th percentile, and equal to or higher than the 90-th percentile computed for the full time period. The selected extremely dry and extremely wet winters are presented in Table 2.3. These winters are considered as 'dry (wet) winters' and their specific large-scale anomalies are analysed by compositing the differences between the dry and the wet winters.

Table 2.3: List of the extremely dry and extremely wet winters

Extremely dry winters	Extremely wet winters
1980-81	1978-79
1982-83	1995-96
1991-92	1965-66
1999-00	2000-01
2001-02	1976-77
2004-05	1962-63

The Student's t-test is applied in order to assess the statistical significance of the differences. The t-statistic, introduced by William Gosset in 1908, is a hypothesing test that follows a Student's t distribution if the null hypothesis is true.

Considering two independent samples X and Y, normally distributed, the null hypothesis states that both samples have the same mean. In these conditions the test statistic t is given by

$$t = \frac{\overline{X} - \overline{Y}}{\sqrt{\frac{Var(X)}{N_X} + \frac{Var(Y)}{N_Y}}} \tag{2.53}$$

where $\overline{X}$ and $\overline{Y}$ are the sample means, $Var(X)$ and $Var(Y)$ are the samples variances and N_X and N_Y are the samples sizes. As already stated, under the null hypothesis the test statistic, follows a t-Student distribution and consequently the differences in the means can be attributed to random sampling. Only values statistically significant at confidence levels equal to or above 90% are considered.

The majority of the applications of Principal Component Analysis (PCA) to atmospheric data have involved analysis of certain fields. The most common are the geopotential heights, temperatures and precipitation. The goal of this analysis is usually to explore the joint space and time variations contained in a large number of variables in the dataset. Each time series of principal components will be uncorrelated with the time series of all the other principal components (PC). The eigenvectors can be displayed graphically in a quite informative way [Wilks, 1995]. Each eigenvector element, usually called Empirical Orthogonal Function (EOF), can be plotted on a map at the same location as its corresponding data value, and this field of eigenvector elements can itself be displayed with smooth contours in the same way as ordinary meteorological fields. Since the EOFs has been widely applied to the Northern Hemisphere atmospheric circulation in previous studies [Barnston and Livezey, 1987; Jollife, 1995; Richman, 1986; Santos et al., 2005, 2007b; Sheridan, 2003; Trigo and Da Camara, 2000; Wallace and Gutzler, 1981] further details will not be considered here.

Since this thesis is devoted to the analysis of the atmospheric circulation mechanisms related to the occurrence of extremes in the winter precipitation over Portugal during the period of 1945 to 2008, this analyses is undertaken also through Empirical Orthogonal Functions (EOF). Daily geopotential mean values for the entire winter season (DJF) in the Euro-Atlantic sector between 20°N-85°N and 100°W-40°E, were considered for the dry (6 winters in Table 2.3) and wet winters (6 winters in Table 2.3) separately, but also for the conjoint series of both dry and wet winters (12 winters, hereafter dry-wet winters). Therefore, the dry and wet winters series have 542 time instants, whereas the dry-wet winters series have 1080 time instants. The choice of the significant modes was made using the logarithmic eigenspectrum, i.e., LEV (logarithmic eigenvalue) diagram. The LEV diagram displays a sharp transition between the signal modes and the noise modes. Therefore, a straight line is fitted to the sequence of higher order eigenvalues. The lower order eigenvalues that are clearly above the straight line are considered to be signal modes.

In order to quantify the synoptic wave activity, a simple approach after Blackmon [1976] and Blackmon et al. [1977] is used, where it is defined as the standard deviation of the bandpass filtered variability of the 500 hPa height field, commonly referred to as 'storm track'. It was originally defined as the standard deviation of the band-pass (2-6 days) filtered variability of 500 hPa geopotential heights, thus representing the sequence of westward propagating upper air troughs and ridges as the tropospheric counterparts of surface cyclones and high pressure systems [Blackmon et al., 1984a, b; Wallace and Gutzler, 1981; Wallace et al., 1988]. The storm track results from Pinto et al. [2007] are considered here, which compute storm track activity from 2.5-8 day bandpass filtered 500 hPa geopotential height standard deviation [Christoph et al., 1995]. The use of the Murakami recursive filter permits a faster determination of the results and produces equivalent results to those obtained with the Blackmon filter [c.f. Christoph et al., 1995]. This variable also includes some variability associated with high-pressure systems (which typically have longer time scales). Bandpass filtering is only applied for storm track computation, as raw daily data is used in all other fields presented here.

Chapter 3
Results

3.1 Dynamical mechanisms of the North Atlantic atmospheric circulation: preliminary analysis

The occurrence of severe precipitation deficits over the Iberian Peninsula and in particular over Portugal is due to the lack of rainfall during several months of the winter half of the year [Santos et al., 2009b; Trigo and Da Camara, 2000]. During the winter season, precipitation is mainly related to transient low-pressure systems entering the continent from the North Atlantic. The North Atlantic Oscillation pattern is largely related, to the preferred locations of the storm track trajectories. However, other large-scale modes of atmospheric circulation are also relevant to the precipitation over these regions [Andrade et al., 2007, 2009a, b; Lolis et al., 2008; Qian et al., 2000; Sáenz et al., 2001]. Indeed, the strength and location of the North Atlantic ridge is of the utmost importance in the study of the conditions that can trigger drought episodes in Portugal. It is well known that during the winter half of the year, the precipitation in Portugal is largely controlled by the large-scale atmospheric circulation [Rodríguez-Puebla et al., 1998; Von Storch et al., 1993]. The severest winter precipitation deficits in Portugal, selected in the previous chapter, are the result of an enhanced stationary wave pattern over the Northern Atlantic. Therefore, a diagnosis of the main forcing mechanisms that contribute to the generation and maintenance of a strong or weak North Atlantic ridge is essential in this analysis.

In this section, the study of the main forcing dynamical mechanisms that generate and maintain the anomalous flow is performed through a preliminary analysis of several relevant basic fields. Their interpretation will enable the identification and quantification of the contributions made by both transient and stationary eddy transports that underlie the contrasting dynamical structures.

3.1.1 Precipitation rate and Precipitable water

Vast quantities of water, in its various phases, are continuously circulating in the atmosphere, although the substance itself does not vary appreciably in the main earth reservoirs. Its complex system of transport in its many forms and through many stages is usually referred to as the hydrological cycle.

The hydrological cycle has two major branches, the terrestrial and the atmospheric. The classical equation of hydrology is attained as a water balance requirement for the terrestrial branch of the hydrological cycle. Applying the principle of continuity to a specific region, for a certain period of time and taking a space average over a large region, the balance equation for the terrestrial branch can be reduced to

$$\{\overline{P}\} = \{\overline{E}\} - \{\overline{R_0}\}, \tag{3.1}$$

where P is the precipitation rate, E is the evaporation rate and R_0 is the surface runoff (Peixoto and Oort, 1996).

The formulation of the atmospheric branch of the hydrological cycle is based on the balance requirements of water vapour in the atmosphere. The amount of water vapour contained in a unit area column of air which extends from the earth's surface to the atmosphere's top, referred to as precipitable water, is given by the expression

$$W(\lambda, \varphi, t) = \int_0^{p_0} \frac{q}{g}\, dp. \tag{3.2}$$

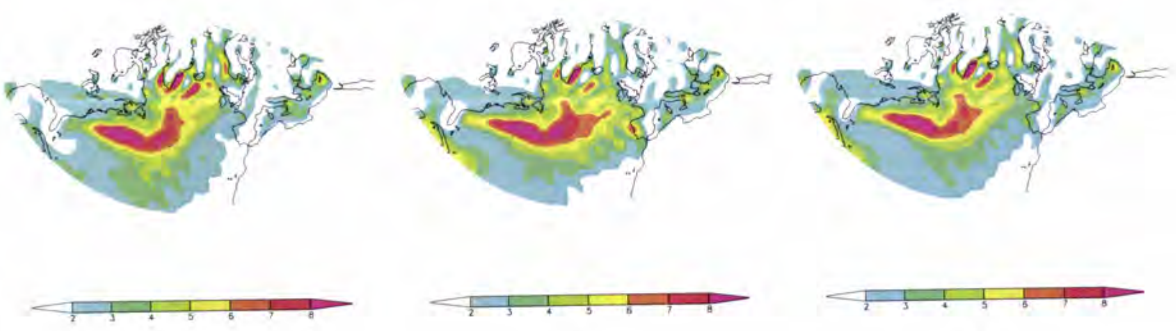

(a) (b) (c)

Figure 3.1: Winter composite of the precipitation rates (shading) in 10^{-5} mm.day^{-1} in the North Atlantic sector between 20°N-80°N and 100°W-40°E for (a) dry winters, (b) wet winters, and (c) winter climatology.

The precipitation regime over the Iberian Peninsula and, in particular, Portugal is characterized by a strong seasonal cycle. The occurrence of intense droughts in these regions during the winter season has a major impact, since summer precipitation can be regarded as irrelevant to the annual total. The study of wintertime precipitation variability is therefore of major relevance, especially because of its impact on society, on economic activities and also on land use and water resources [Qian et al., 2000; Santos et al., 2009b, 2007b; Trigo and Da Camara, 2000; Ulbrich et al., 1999b]. The analyses of the precipitable water fields thus plainly justified, since it represents the amount of liquid water that would result if all of the water vapour in the unit area column of the atmosphere was condensed [Dirmeyer and Brubaker, 2006]. Therefore, significant differences in precipitable water, as well as in the precipitation rate fields for the wet and dry winters are expected between wet and dry winters.

The observation of Figs. 3.1(a) and 3.1(b) patterns indicates a clear distinction between dry and wet winters respecting the Iberian Peninsula. While for dry winters a band of high precipitation values is significantly deviated towards Northeastern Europe, and consequently deviated from the Iberian Peninsula, for wet winters this band is much more zonal. Since this band of high precipitation values is commonly associated with the storm track and its baroclinic systems, this deviation away from the Iberian Peninsula is even more meaningful in terms of precipitation anomalies. This southwest-northeast tilted path in the maximum precipitation band is also observed for the winter climatology (Fig. 3.1(c)), although with a much weaker pattern.

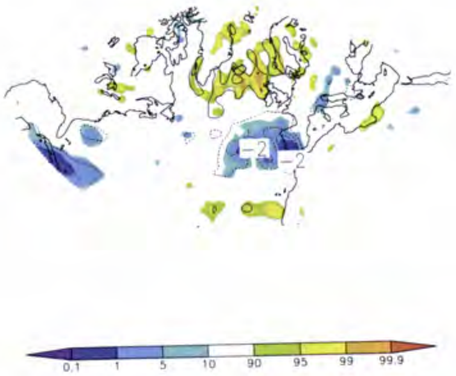

Figure 3.2: Difference of the precipitation rates between dry and wet winters (contours) in 10^{-5} mm.day^{-1} and the corresponding p-values of the Student's t-test (shading) in the North Atlantic sector between 20^{o}N-80^{o}N and 100^{o}W-40^{o}E.

Significant anomalies occur mainly in the North Atlantic, (Fig. 3.2) covering large areas of the Atlantic, westward and north-westward of the Iberian Peninsula. These anomalies are also relevant over some areas of Southern Europe, as well as Northern Europe, being however of opposite signal. Despite some obvious similarities, this pattern resembles the North Atlantic Oscillation (NAO), although northwardly shifted from the typical NAO pattern. The negative anomalies westward and over the Iberian peninsula means that the occurrence of the most severe winter precipitation deficits and surplus in Portugal are not due to local or regional effects, but rather to anomalies in the large-scale circulation [Santos et al., 2009b, 2007a; Trigo et al., 2002].

The analysis of precipitable water for the dry and wet winters, (Figs. 3.3(a) and 3.3(b)), reveals a continuous decrease from the equatorial regions towards the North Pole. This pattern mainly reflects the exponential dependence of the saturation pressure vapour with temperature. It also revealed that precipitable water is higher over the oceans than over the continents, as expected, since over the desert areas its values decrease mainly due to strong subsidence. This effect is also pronounced in the eastern portions of the large semi-permanent anticyclones of the subtropics [Peixoto and Oort, 1992]. Despite the clear differences between dry and wet winters, it is still noteworthy the resemblance between the wet and winter climatology patterns.

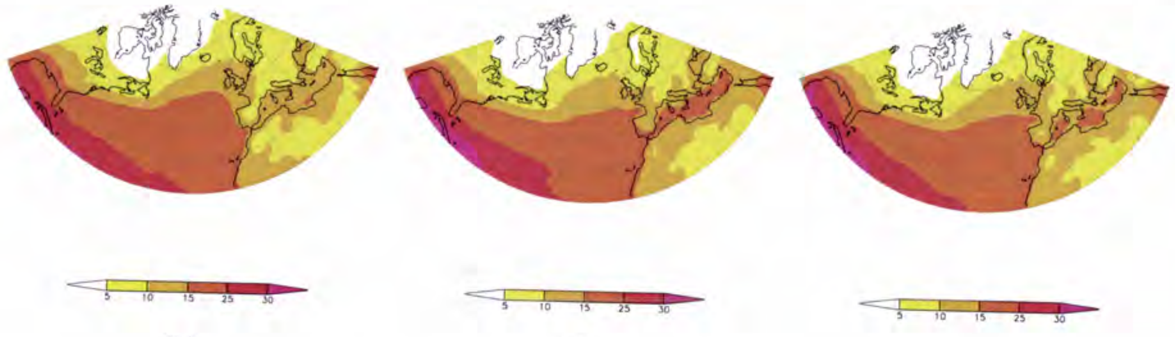

(a) (b) (c)

Figure 3.3: Winter composite of the precipitable water (shading) in mm in the North Atlantic sector between 20^{o}N-80^{o}N and 100^{o}W-40^{o}E for (a) dry winters, (b) wet winters, and (c) winter climatology.

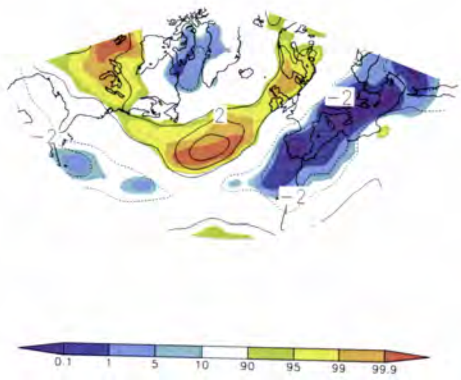

Figure 3.4: Difference of the precipitable water between dry and wet winters (contours) in mm and the corresponding p-values of the Student's t-test (shading) in the North Atlantic sector between 20^{o}N-80^{o}N and 100^{o}W-40^{o}E.

Both precipitable water (Fig. 3.3) and difference fields are consistent with the precipitation rate fields (Fig. 3.1), though significant differences (Fig. 3.4) can be observed. As already stated, the effect of air temperature on the latter variable is also important, since the atmosphere capacity to retain water vapour strongly depends on temperature. Overall, the relevant differences can be found along three bands of opposite signals (Fig. 3.4); two positive and one negative in between. This suggests that the westerly jet structure and trajectory is considerably different in dry and wet winters. The negative differences over the Mediterranean Basin and the extension of the bands over other regions outside the Euro-Atlantic sector are also relevant.

3.1.2 Sea level pressure

The North Atlantic Oscillation (NAO) is one of the most prominent and oldest known pattern of large-scale atmospheric variability [Stephenson et al., 2003]. Nonetheless the work of both Exner and Defant were known, Sir Gilbert Walker concept of the NAO became popular during the 1920s. Throughout the last century the NAO index calculation has been improved. NAO is thus a large-scale alternation of atmospheric mass between the North Atlantic regions of the subtropical high surface pressure (centered near Azores) and of the sub-polar low surface pressure (extending south and east of Greenland). It is well known that the phase and strength of the NAO determines the strength and orientation of the poleward pressure gradient over the North Atlantic, and hence the speed and direction of the mid-latitude westerlies across this ocean, also affecting the tracks of the low-pressure storm systems within the Euro-Atlantic sector [Lamb and Pepler, 1987; Osborn et al., 1999; Thompson and Green, 2004; Ulbrich and Christoph, 1999a]. In the last years, some authors have changed the stations used to calculate this index. Instead of Ponta Delgada, a Gibraltar-Iceland normalized index is determined [Jones et al., 1997].

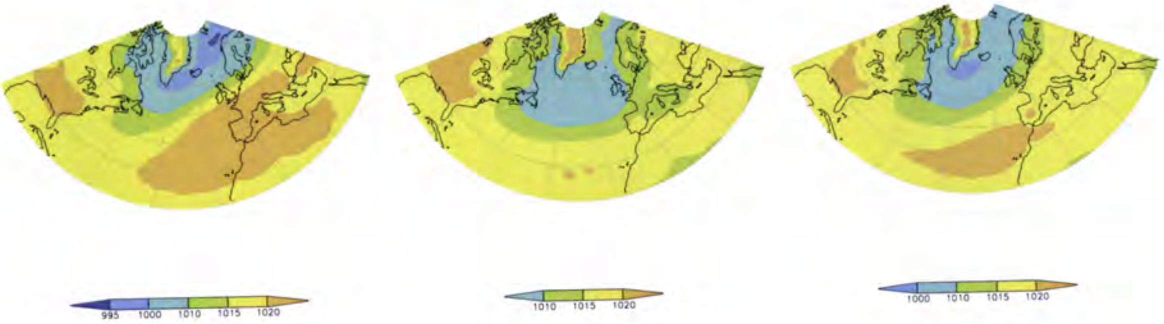

(a) (b) (c)

Figure 3.5: Winter composite of the mean sea level pressure (shading) in 10^2 Pa in the North Atlantic sector between 20^{o}N-80^{o}N and 100^{o}W-40^{o}E for (a) dry winters, (b) wet winters, and (c) winter climatology.

The NAO is thus one of the major forcing mechanisms that influence the winter precipitation in Portugal. Its negative phase is associated to wet conditions while a positive phase relates to drought conditions, due to the presence of an enhanced Azores High in the North Atlantic [Thompson and Green, 2004].

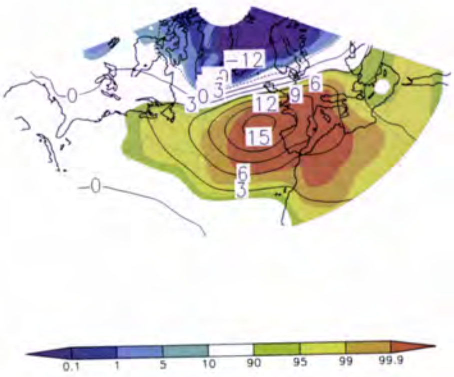

Figure 3.6: Difference of the mean sea level pressure between dry and wet winters (contours) in 10^2 Pa and the corresponding p-values of the Student's t-test (shading) in the North Atlantic sector between 20^{o}N-80^{o}N and 100^{o}W-40^{o}E.

Though the NAO index is not presented in this study, the analysis of the sea level pressure fields is relevant and is going to be discussed in this section, since the occurrence of pressure anomalies northwestward of Iberia is rather relevant for the selected case study. Hurrel [1995] has showed that changes in the North Atlantic pressure system, associated to high (low) NAO indexes, strongly affect the moisture transport across the North Atlantic. Also Thompson and Green [2004] revealed that 'precipitation in the Mediterranean is correlated with the pressure variations across the North Atlantic'. Indeed, negative or positive precipitation anomalies are respectively linked to anomalously high or low sea level pressure values, north-westward of Iberia (Figs. 3.5(a) and 3.5(b)). The joint effect yields a northeastward displaced NAO pattern as being the most relevant for precipitation in Portugal, (Fig. 3.6).

3.1.3 Mean Geopotential height

The geopotential height is an important field due its relation with temperature and pressure. Let us remind that the geopotential $\Phi(z)$ at height z is the work required to raise a unit mass to height z from mean sea level

$$\Phi = \int_0^z g\,dz \tag{3.3}$$

if the value of the geopotential is set to zero at mean sea level [Peixoto and Oort, 1992]. The variation of the geopotential with respect to altitude (pressure) depends only on temperature, in a hydrostatic atmosphere,

$$\Phi(z_2) - \Phi(z_1) = g_0(Z_2 - Z_1) = R\int_{p_2}^{p_1} T\,d\ln p \tag{3.4}$$

where $Z = \frac{\Phi(z)}{g_0}$ is the geopotential height, and $g_0 = 9.80665\,m.s^{-2}$ is the value of the global average of gravity at mean sea level.

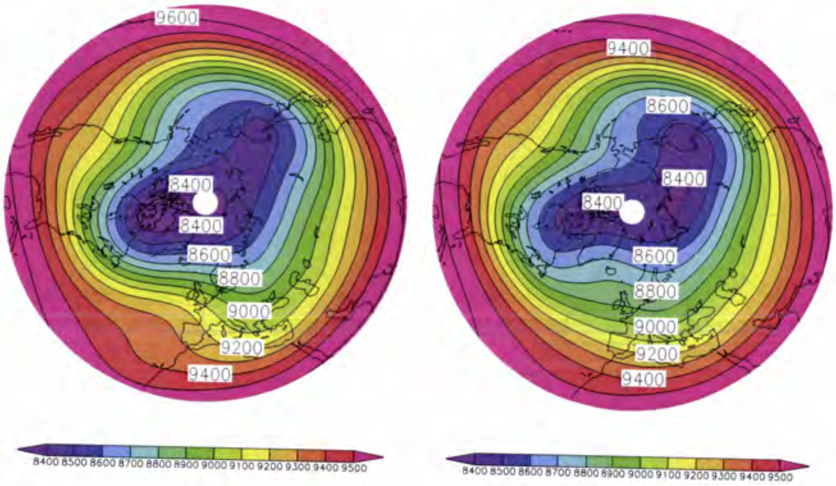
9600
8400
8400
8600
8800
9000
9200
9400
8400 8500 8600 8700 8800 8900 9000 9100 9200 9300 9400 9500
9400
8600
8400
8400
8600
8800
9000
9200
9400
8400 8500 8600 8700 8800 8900 9000 9100 9200 9300 9400 9500

(a) (b)

Figure 3.7: Winter composite of the mean geopotential field in gpm at 300 hPa over the Northern Hemisphere between 20°N-85°N for (a) dry winters, and (b) wet winters.

The difference between the dry and wet winters is quite obvious. For the dry winters (Fig. 3.7(a)) a well defined ridge over the Northern Atlantic at mid-latitudes is observed.

The ridge extends southwestward of Portugal, so it is dynamically different when comparing the same region for the wet winters. In this case, the pattern depicted is almost zonal (Fig. 3.7(b)). These contrasting characteristics are depicted in difference pattern (Fig. 3.8) were two small negative anomalies with a large positive anomaly in between is observed in the North Atlantic.

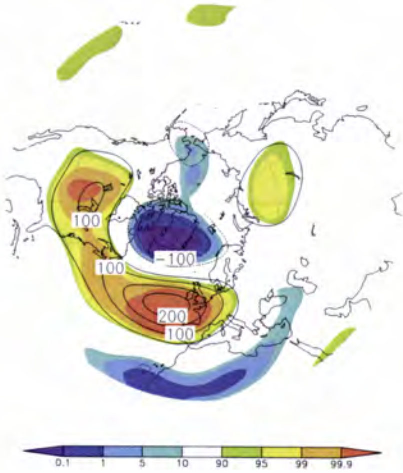

Figure 3.8: Difference of the mean geopotential field between dry and wet winters (contours) in gpm at 300 hPa and the corresponding p-values of the Student's t-test (shading) over the Northern Hemisphere between 20^{o}N-85^{o}N.

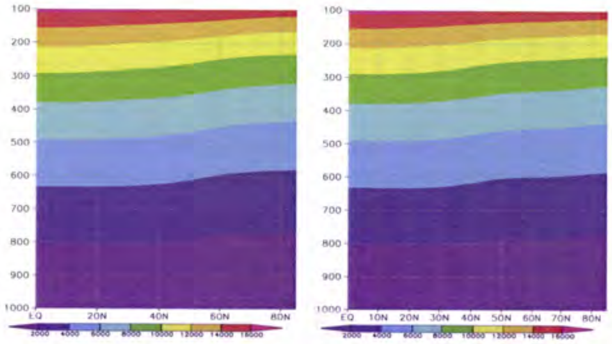

(a) (b)

Figure 3.9: Cross-section of the zonal-mean (60^{o}W-0^{o}E) winter composite of the mean geopotential field in gpm over the Northern Hemisphere sector between 0^{o}N-85^{o}N for (a) dry winters, and (b) wet winters.

Although the zonal-mean geopotential for the dry (Fig. 3.9(a)) and wet winters (Fig. 3.9(b)) pattern seem quite similar, a dipolar vertical structure is observed for the zonal-mean geopotential height at different tropospheric levels (Fig. 3.10). This is a clear result of the strengthening (weakening) of the North Atlantic ridge for the dry (wet) winters, respectively. Additionally, these isobaric surface patterns reflect important changes in the low and high-latitude regimes of the stationary planetary waves. Once more, the differences between dry and wet winters are quite obvious (Fig. 3.10). During wet winters, the North Atlantic ridge is significantly displaced towards much higher latitudes.

DADE DE ÉVORA

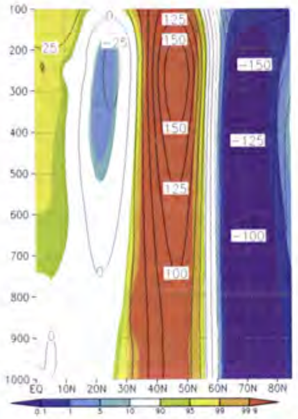

Figure 3.10: Cross-section of the zonal-mean (60^{o}W-0^{o}E) difference of the mean geopotential field between dry and wet winters (contours) in gpm and the corresponding p-values of the Student's t-test (shading) over the Northern Hemisphere between 0^{o}N-85^{o}N.

A maximum core (positive differences) can be found aloft (~ 300 hPa) between approximately 45^{o}N and 50^{o}N (Fig. 3.11(a)). For the negative (positive) precipitation anomalies the North Atlantic ridge is significantly strengthened (weakened), respectively. Moreover, the near vertical tilt of the maximum anomaly axis for the dry winters suggests that the ridge has a nearly equivalent barotropic structure (Figs. 3.9(a) and 3.9(b)). Similar results will be attained for the potential temperature field analysed in section 3.1.3 .

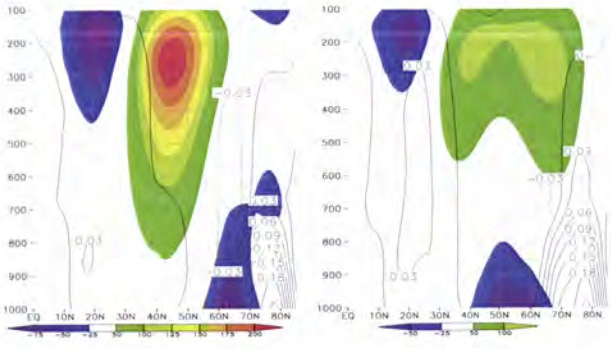

(a) (b)

Figure 3.11: Cross-section of the zonal-mean (60^{o}W-0^{o}E) difference of the mean geopotential field and its hemispheric mean (shading) in gpm and the corresponding winter mean omega-vertical velocity (contours) in Pa.s^{-1} over the Northern Hemisphere between 0^{o}N-85^{o}N for (a) dry winters, and (b) wet winters.

The omega-vertical velocities show that during the dry winters the sub-tropical subsidence is northwardly displaced and observed over a broader latitude belt than during the wet winters. Conversely, the sub-polar ascending motions are enhanced for the dry winters, which might be associated with a dynamical compensation mechanism. The difference pattern (Fig. 3.12) depicts a tri-pole with two negative cores and a positive one in between. These cores extended throughout the troposphere and the positive core is located in the mid-latitudes. This result is in clear accordance with the presence of an enhanced ridge over the North Atlantic during the dry winters.

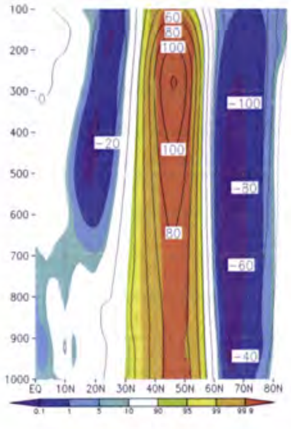

Figure 3.12: Cross-section of the zonal-mean (60^oW-0^oE) difference of the mean geopotential field and its hemispheric mean (contours) in gpm and the corresponding p-values of the Student's t-test (shading) over the Northern Hemisphere between 0^oN-85^oN.

The majority of the applications of Principal Component Analysis (PCA) to atmospheric data involve the analysis of the geopotential height field, temperature and precipitation. In particular, since its introduction in atmospheric sciences by Lorenz (1956) the technique called Empirical Orthogonal Function (section 2) analysis has been widely used to describe geophysical fields, besides meteorology and climatology. EOF analysis is a technique that is used to determine the principal modes that characterize the atmospheric variability and also to obtain its spatial structures. This subsection examines the characteristics of mean geopotential height field and its relationship with the dominant modes of large-scale atmospheric circulation for the dry, wet and dry-wet winters.

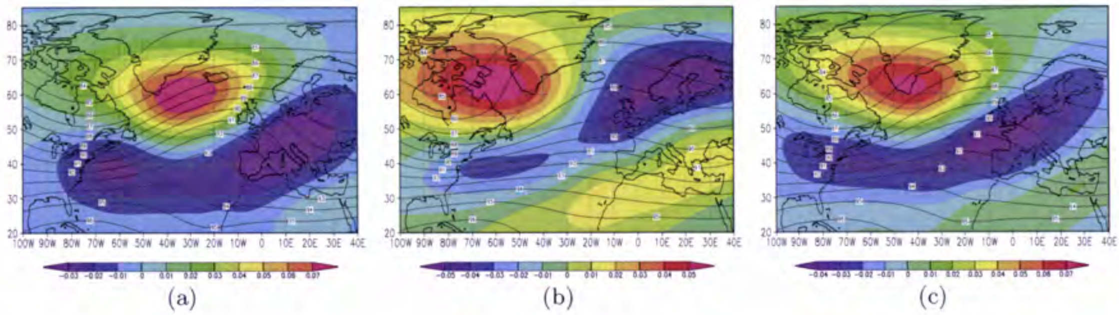

Figure 3.13: EOF1 of the mean geopotential field in the North Atlantic sector between 20^oN-85^oN and 100^oW-40^oE for (a) dry winters (90.3% explained variance), (b) wet winters (90.3% explained variance), and (c) dry-wet winters (90.0% explained variance), and the corresponding mean geopotential field in 10^2 gpm at 300 hPa .

An EOF analysis was applied to the dry and wet winters, separately, but also to the series obtained from both dry and wet winters, the dry-wet winters as previously stated in Section 2. Since the first EOF for all time series explains about 90% of variance, only EOF1 is presented. For the wet winters (Fig. 3.13(b)), a positive nuclei is observed near Greenland, displaced westward into the strait of Davis in a region commonly associated to intense cyclonic activity. This location is also a preferred location of the storm track path, as will be seen in the next subsection. The most striking difference between the EOF patterns for the dry and wet winters can be seen in middle latitudes. For the dry winters (Fig. 3.13(a)) the location of a strong negative nuclei in the North Atlantic, displaced northward to the British Isles can be associated with the location of a strong North Atlantic ridge. Moreover, this pattern also resembles the typical dipole pattern of the NAO. These results are plainly coherent with the presence of an enhanced stationary wave pattern over the North Atlantic during dry winters [Andrade et al., 2008a].

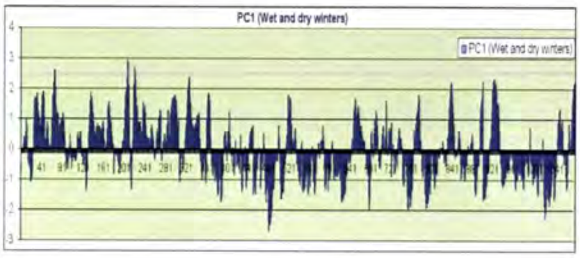

Figure 3.14: Chronogram of the normalized PC1 of the dry-wet winters mean geopotential field in 10^2 gpm in the North Atlantic sector between 20°N-85°N and 100°W-40°E.

The dry-wet winters EOF pattern (Fig. 3.13(c)) is quite similar to the pattern observed for the dry winters. This result can thus indicate that the number of days that have contributed to the dry conditions might be superior to those that have contributed to the wet conditions. Therefore, from the corresponding normalized PC1 (Fig. 3.14) the values above (positive composite) and below (negative composite) one standard deviation were selected, and the corresponding series was obtained. The geopotential field obtained for the positive composite (Fig. 3.15(a)) reveals a very pronounced omega shape ridge over the North Atlantic, whereas the negative composite (Fig. 3.15(b)) has a much smoother and eastward tilted ridge. These results are consistent with the relevance of a strong North Atlantic ridge as a large-scale mechanism associated with the occurrence of severe drought episodes in the Iberian Peninsula [Andrade et al., 2008a].

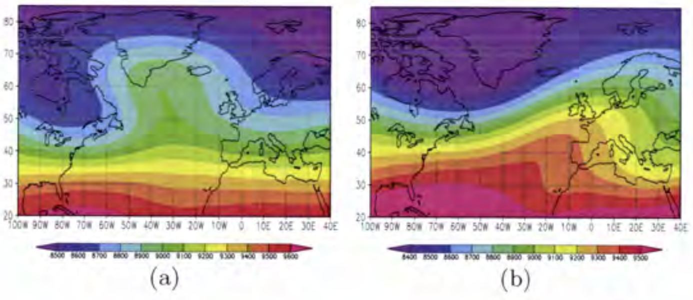

(a) (b)

Figure 3.15: Mean geopotential field obtained from PC1 in the North Atlantic sector between 20°N-85°N and 100°W-40°E for the (a) positive composite, and (b) negative composite.

3.1.4 Storm Track

As previously referred, the general atmospheric circulation includes mid-latitude tropospheric jet streams. Superimposed on the tropospheric jet streams are eastward propagating, baroclinic waves. These baroclinic waves feed upon the north-south temperature contrast in mid-latitudes. Moreover, they are included in the so-called weather systems in response to instabilities in the large-scale flow in which they are embedded [Wallace and Hobbs, 2006].

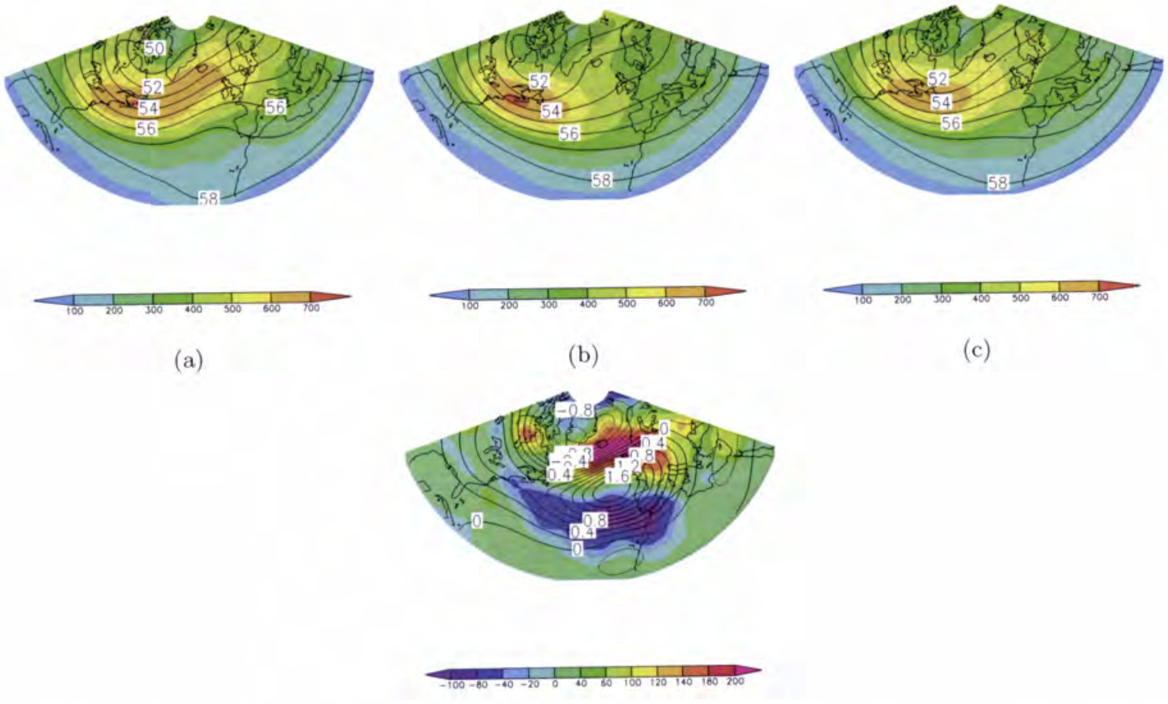

(a) (b) (c)

(d)

Figure 3.16: Winter composite of the storm track (shading) in gpm at 500 hPa, and the corresponding mean geopotential height field (contours) in 10^2 gpm in the North Atlantic sector between 20°N-85°N and 100°W-40°E for (a) dry winters, (b) wet winters, (c) winter climatology, and (d) the difference between dry and wet winters.

The extratropical cyclones are very relevant for the study of the mid-latitudes climate. As previously mentioned, they are generated preferentially along the polar front between two contrasting air masses, the subtropical and the polar, over mid-latitudes. In the North Atlantic region, the eastern North American continent is a preferred location area. This region presents strong meridional temperature gradients which, linked to several perturbations, triggers the development and intensification of cyclones. In recent diagnostic studies regarding the extratropical atmospheric circulation, special attention has been given to the dynamical properties of the wintertime storm tracks. These tracks are commonly located downstream and slightly poleward of the North Atlantic jet streams and represent the preferred trajectories of weather systems in middle latitudes, being cyclones often associated with severe precipitation extremes [Santos et al., 2009c]. Consequently the analysis of the storm track patterns can give further insight into the synoptic wave activity during the contrasting winters.

The geopotential height at 500 hPa also shows a well-defined ridge west of the Iberian Peninsula, oriented northward to the British Isles in the dry winters (Fig. 3.16(a)), while a nearly zonal (westerly) flow is observed in the wet and also in the winter climatologies (Figs. 3.16(b) and 3.16(c)). In fact, the presence of a strong warm-core ridge westward of Iberia, with a nearly equivalent barotropic structure, is clearly unfavourable to rain generation over Western Iberia [Santos et al., 2009b, 2007a]. The enhanced ridge blocks the westerly propagation of the baroclinic disturbances (weather systems) over the North Atlantic, leading to a northward deflection of the storm track over the Eastern North Atlantic (Fig. 3.16(b)). This explains the lack of precipitation in Portugal, since such systems tend to carry moist and unstable air masses that are usually favourable to the occurrence of precipitation. The anomalous flow is particularly clear when analysing the storm track anomalies against the wet winters (Fig. 3.16(d)). A dipolar structure, similar to the North Atlantic Oscillation, but northeastwardly displaced, is quite evident [c.f. also Ulbrich et al., 2008]. While an important negative anomaly in the storm track occurs over the North Atlantic and southwestern Iberia, strong positive anomalies occur over northern and central Europe. These results document again the link between anomalous large-scale circulation and winter rainfall deficits over Portugal.

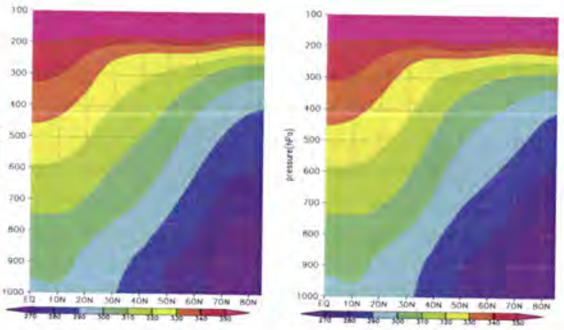

(a) (b)

Figure 3.17: Cross-sections of the mean-meridional (60°W-0°E) potential temperature in K in the Northern Hemisphere between 0°N-85°N for (a) dry winters, and (b) wet winters.

3.1.5 Potential temperature

Due to its relevance in the study of the dynamical processes in the atmosphere, this subsection will be devoted to the analysis of the potential temperature. It is worth mentioning that the potential temperature takes implicitly into account the effects of the compressibility of the air. That is the temperature that a parcel of air would attain in a reversible, adiabatic process if the parcel were displaced to a reference level p_{00} ($\simeq$ 1000 hPa),

$$\theta = T\left(\frac{p_{00}}{p}\right)^{k}, \tag{3.5}$$

where $k = \frac{R_d}{c_p} \cong 0.286$ (Arya, 2001; Peixoto and Oort, 1996).

Figures 3.17(a) and 3.17(b) show that the values of the potential temperature increase with height, and minimum values can be found near the surface in Polar Regions in both dry and wet winters. Nevertheless, in the middle latitudes, near 40^{o}N between 800 and 400 hPa, a slight difference can be observed in Fig. 3.18. The smoother slopes of the isentropes for the dry winters are also suggestive of lower levels of baroclinic activity. Moreover, the strengthening (weakening) of the North Atlantic ridge is dynamically accompanied by the presence of warm (cold) cores, which are clearly depicted in potential temperature difference patterns over the North Atlantic (Fig. 3.18). These results are plainly consistent with the results attained by Savijärvi [1978]. Consequently, a clear differentiation between the subtropical and polar jets, accompanied by a nearly equivalent barotropic warm-core, can be observed over the North Atlantic, resulting in the enhancement of the large-scale stationary wave pattern. In response to the strengthening of the ridge, important upward motions are expected poleward of its core. These features will be further investigated by analysing the winter composites for wind streamlines and intensity, as well as the winter zonal wind component.

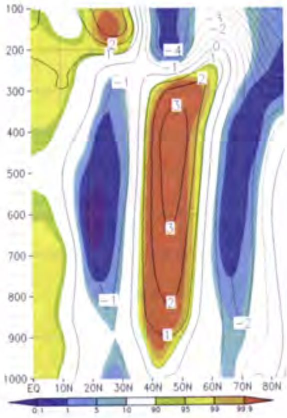

Figure 3.18: Cross-section of the mean-meridional (60^{o}W-0^{o}E) difference of the potential temperature between dry and wet winters (contours) in K and the corresponding p-values of the Student's t-test (shading) over the Northern Hemisphere between 0^{o}N-85^{o}N.

3.1.6 Horizontal transports of enthalpy

The understanding of the large-scale atmospheric circulation requires the study of fields that characterize the state of the atmosphere. These fields are highly variable both in time and space and it is common to use average conditions. The use of averages can be performed, in spaces, in certain time intervals, and in space-time domains. Let us thus remind that $\overline{(\ )}$ represents the time-mean and $(\ )'$ the deviation from the time-mean. As such, the instantaneous value of a quantity A is given by

$$A = \overline{A} + A'.$$

Noting that $[\ ]$ represents the zonal-mean and $(\ )^*$ the departure from the zonal-mean; and considering the generic variable A

$$A = [A] + A^*.$$

From the combination of both time and space expansions, an important relation is then obtained,

$$A = \left[\,\overline{A}\,\right] + \overline{A}^* + [A]' + A'^*,$$

where $[\,\overline{A}\,]$ represents the zonally symmetric part of the steady time-mean of A, $\overline{A}^*$ the asymmetric part of the time-mean of A, $[A]'$ represents the instantaneous fluctuations of the symmetric term, and finally A'^* the instantaneous fluctuations of the zonally asymmetric term.

Considering now the quantities A and B, similar considerations can be made leading to the following relationship

$$[\,\overline{AB}\,] = [\,\overline{A}\,]\,[\,\overline{B}\,] + \left[\overline{A}^*\overline{B}^*\right] + [\,\overline{A'B'}\,],$$

where the time-mean and zonal-mean can then be decomposed into three different and physically meaningful components: the mean meridional circulation, the stationary eddies and the transient eddies, respectively. The latter equality enables a useful decomposition of the general circulation. In fact, it allows the identification of the mechanisms responsible for the different modes of transport and their relative importance, location and magnitude. This decomposition undertaken in this section in order to analyse the transports of enthalpy and other upcoming fields. Therefore, the total horizontal transports of enthalpy are given by

$$\overline{uT}\,\mathbf{i} + \overline{vT}\,\mathbf{j}, \tag{3.6}$$

and the transient horizontal transports of enthalpy by

$$\overline{u'T'}\,\mathbf{i} + \overline{v'T'}\,\mathbf{j}. \tag{3.7}$$

The patterns of total horizontal transports of enthalpy for the dry and wet winters (Figs. 3.19(a) and 3.19(b)), are two orders of magnitude smaller than the transient transports (Figs. 3.21(a) and 3.21(b)), revealing relevant differences. These differences are more evident westward the Iberian Peninsula where a clear minimum core is observed for the dry winters. The difference of the two total horizontal transports of enthalpy display once more a tri-pole of opposite signals over the North Atlantic (Fig. 3.20).

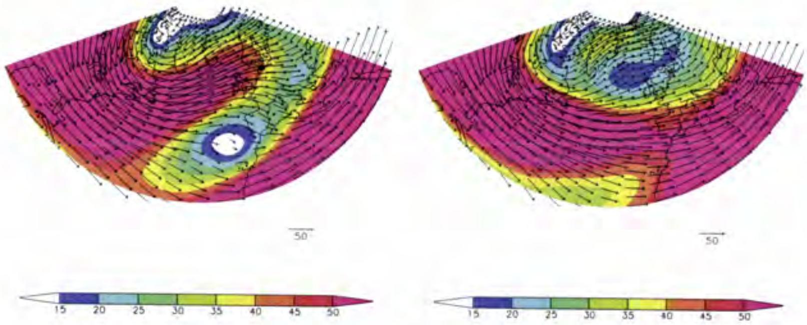

(a) (b)

Figure 3.19: Winter composite of the total horizontal transports of enthalpy in 10^2 K.m.s^{-1} at 300 hPa in the North Atlantic sector between 20^oN-80^oN and 100^oW-40^oE for (a) dry winters, and (b) wet winters. Shading represents the intensity of the fluxes, and arrows represent the horizontal fluxes.

Similar considerations can be made for the transient enthalpy transports since the differences between dry and wet winters are quite obvious. For the dry winters, the transport of enthalpy is displaced northeastward (Fig. 3.21(a)), while a nearly zonal flow is observed for the wet winters (Fig. 3.21(b)). The difference patterns (Fig. 3.22) also indicate a significant decrease in the intensity of the transports over the eastern North Atlantic for the dry winters, when compared to wet winters. The regions of the maxima intensity of the transports are concentrated in the preferred locations of the storm track [Lau and Nath, 1991]. These results are in clear accordance with those obtained by Holopainen et al. [1982]. Again they are also plainly consistent with the presence of a strong North Atlantic ridge, blocking the westerly propagation of the weather systems towards the Iberian Peninsula during dry winters. Furthermore, the intensity of the transports produced by the enthalpy fluxes when comparing with those produced by the momentum fluxes, to be presented in the next subsection (Fig. 3.26), is also noteworthy. This result underlies the relative importance of some EFF components, since the diabatic heating and transient fluxes are directly related to the first, second, third and sixth components of the EFF (2.43), (2.44), (2.45), (2.48). Hence, the above described patterns are expected to emerge again in the EFF patterns.

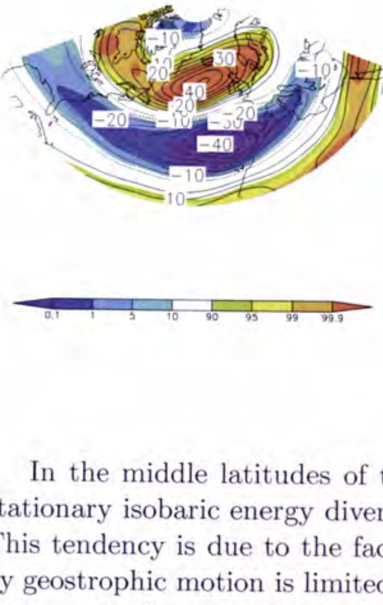

Figure 3.20: Difference of the total horizontal transports of enthalpy between dry and wet winters (contours) in 10^2 K.m.s^{-1} at 300 hPa and the corresponding p-values of the Student's t-test (shading) in the North Atlantic sector between 20°N-80°N and 100°W-40°E.

In the middle latitudes of the Northern Hemisphere, the patterns of the transient and stationary isobaric energy divergence in the baroclinic waves tend in general to be opposite. This tendency is due to the fact that the isobaric divergence of the total energy transports by geostrophic motion is limited by the advection of enthalpy. Therefore, an increase of temperature in the lower troposphere through convergence of the enthalpy transports implies an increase, in the upper levels, of geopotential energy by transient enthalpy convergence. Moreover, the low-level convergence of transient transports in higher latitudes and the low-level divergence in lower latitudes are heat sources and sinks, respectively, forcing upward mass flux at higher latitudes and downward in subtropical latitudes [Chen et al., 2001; Johnson, 1989]. In this manner, the observation of the dry winters convergence of the transient transports of enthalpy (Fig. 3.23(a)) reveals a broad band of convergence throughout the North Atlantic into the British Isles that highly contrasts with a convergence band that is interrupted over the North Atlantic southward of Greenland for the wet winters (Fig. 3.23(b)). These results are in clear accordance with the presence of a strong North Atlantic ridge during dry winters, since the centres of energy convergence are located primarily over oceanic anticyclonic circulations [Davis et al., 1997].

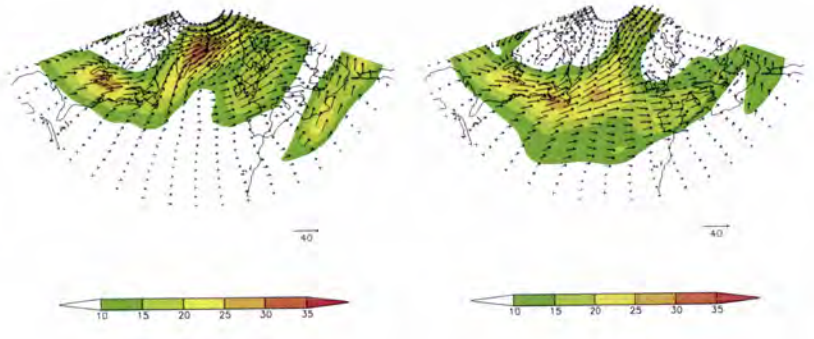

(a) (b)

Figure 3.21: Winter composite of the transient horizontal transports of enthalpy in K.m.s^{-1} at 300 hPa in the North Atlantic sector between 20^{o}N-80^{o}N and 100^{o}W-40^{o}E for (a) dry winters, and (b) wet winters. Shading represents the intensity of the fluxes, and arrows represent the horizontal fluxes.

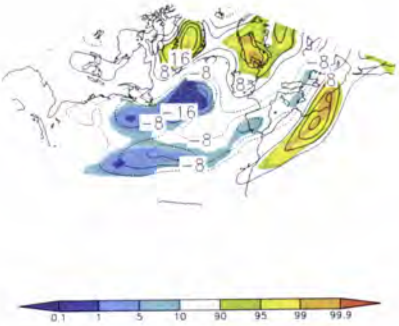

Figure 3.22: Difference of the transient horizontal transports of enthalpy between dry and wet winters (contours) in K.m.s^{-1} at 300 hPa and the corresponding p-values of the Student's t-test (shading) in the North Atlantic sector between 20^{o}N-80^{o}N and 100^{o}W-40^{o}E.

3.1.7 Horizontal transports of momentum

The interactions between large-scale eddies and the zonal-mean fields are of high relevance to better understand the dynamics of the atmospheric circulation, since these eddies are important for the maintenance of the zonal-mean flow. Not only the eddy enthalpy fluxes are important in this process, but also the eddy momentum fluxes are associated with its maintenance. As in the previous section, both total and transient transports of zonal momentum are presented and are respectively given by the flux vectors

$$\overline{u^2}\,\mathbf{i} + \overline{uv}\,\mathbf{j}, \qquad (3.8)$$

and

$$\overline{u'^2}\mathbf{i} + \overline{u'v'}\mathbf{j}. \qquad (3.9)$$

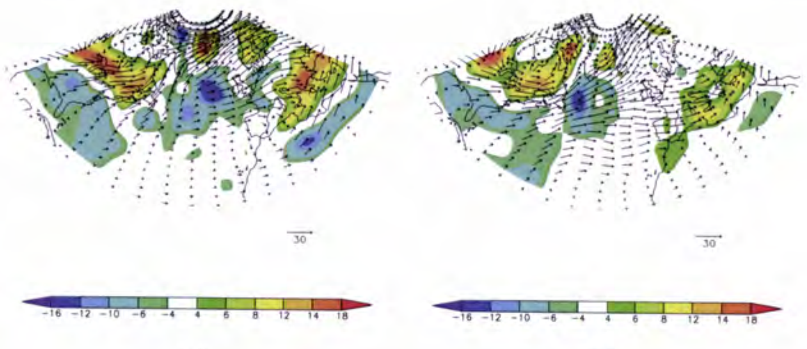

(a) (b)

Figure 3.23: Winter composite of the horizontal convergence of the transports of enthalpy in K.s^{-1} at 300 hPa in the North Atlantic sector between 20^{o}N-80^{o}N and 100^{o}W-40^{o}E for (a) dry winters, and (b) wet winters. Shading represents the intensity of the fluxes, and arrows represent the horizontal fluxes.

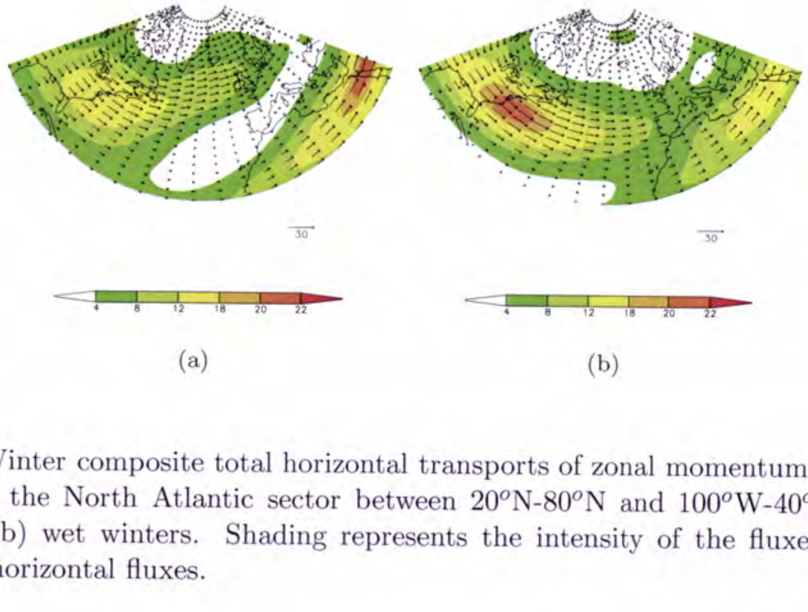

(a) (b)

Figure 3.24: Winter composite total horizontal transports of zonal momentum in 10^2 m^2.s^{-2} at 300 hPa in the North Atlantic sector between 20^{o}N-80^{o}N and 100^{o}W-40^{o}E for (a) dry winters, and (b) wet winters. Shading represents the intensity of the fluxes, and arrows represent the horizontal fluxes.

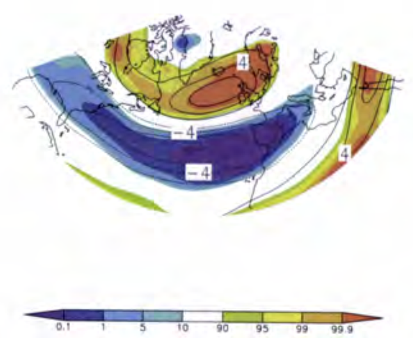

Figure 3.25: Difference of the total horizontal transports of momentum between dry and wet winters (contours) in 10^2 m^2.s^{-2} at 300 hPa and the corresponding p-values of the Student's t-test (shading) in the North Atlantic sector between 20^{o}N-80^{o}N and 100^{o}W-40^{o}E.

A significant decrease in the intensity of the total transports over the eastern North Atlantic can be observed for the dry winters (Fig. 3.24(a)) when compared to the wet winters (Fig. 3.24(b)). The wet winter patterns depict an almost zonal flow. Once more, these results are plainly consistent with the presence of a strong North Atlantic ridge.

When comparing the total horizontal transports of zonal momentum with the transient transports, the latter transports are smaller and thus give a small contribution to these total transports. The transient fluxes over the Northern Atlantic tend to be limited to higher latitudes for the dry winters (Fig. 3.26(a)), while for the wet winters (Fig. 3.26(b)) they are also important on lower latitudes. This result is clear in the difference pattern (Fig. 3.27) as a consequence of the path of the transient systems, which in turn tend to follow the westerly jet [Holopainen et al., 1982].

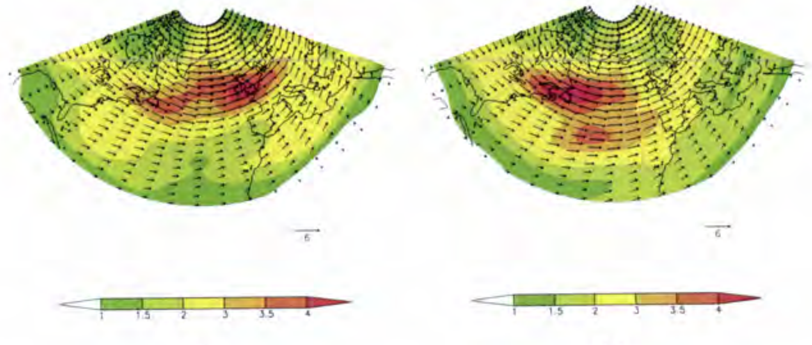

(a) (b)

Figure 3.26: Winter composite transient horizontal transports of zonal momentum in 10^2 $m^2.s^{-2}$ at 300 hPa in the North Atlantic sector between 20^{o}N-80^{o}N and 100^{o}W-40^{o}E for (a) dry winters, and (b) wet winters. Shading represents the intensity of the fluxes, and arrows represent the horizontal fluxes.

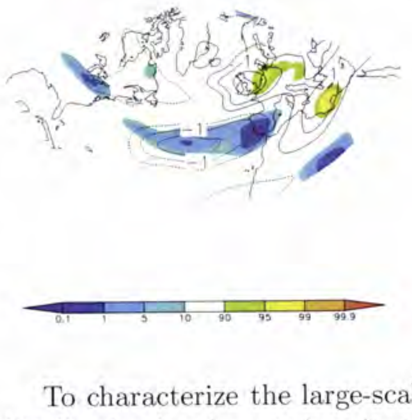

Figure 3.27: Difference of the transient horizontal transports of momentum between dry and wet winters (contours) in 10^2 $m^2.s^{-2}$ at 300 hPa and the corresponding p-values of the Student's t-test (shading) in the North Atlantic sector between 20^{o}N-80^{o}N and 100^{o}W-40^{o}E.

To characterize the large-scale atmospheric circulation the analysis of the kinetic energy distribution is relevant since its transient eddy component mainly reflects the dominant storm tracks in mid-latitudes. Therefore, although the total mean kinetic energy, per unit mass, is the sum of the transient eddy, stationary eddy, and zonal-mean components, only the transient eddy kinetic energy component was computed using

$$K_{TE} = \frac{1}{2}\left[\overline{u'^2} + \overline{v'^2}\right]. \tag{3.10}$$

This procedure follows the results after Newell et al. [1974] which indicated that about half of the kinetic energy in the atmosphere is embedded in the large-scale transient eddies.

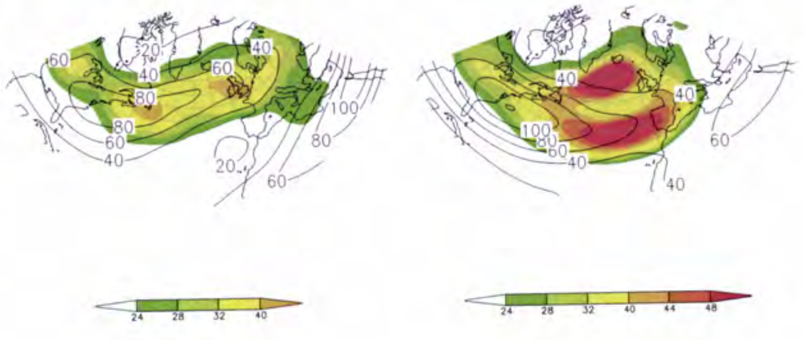

(a) (b)

Figure 3.28: Winter composite of the mean kinetic energy (contours) and transient mean kinetic energy (shading) in 10^1 $m^2.s^{-2}$ at 300 hPa in the North Atlantic sector between 20°N-80°N and 100°W-40°E for (a) dry winters, and (b) wet winters.

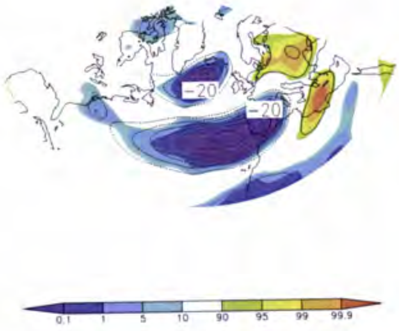

Figure 3.29: Difference of the transient mean kinetic energy between dry and wet winters (contours) in 10^1 $m^2.s^{-2}$ at 300 hPa and the corresponding p-values of the Student's t-test (shading) in the North Atlantic sector between 20°N-80°N and 100°W-40°E.

As previously referred, the transient mean kinetic energy correlates well with the locations of the storm tracks. The observation of the dry winter pattern reveals a significant decrease and a northward displacement over the North Atlantic, whereas the wet winters pattern depict the presence of two cores of maximum transient kinetic energy. It is worth noticing that these two belts of maximum kinetic energy were also observed for the wet winters in the transient transports of momentum.

3.1.8 Horizontal transports of humidity

It is well known that the amount of water vapour for a given volume of air can be expressed in different ways; in this section the specific humidity is used to analyse both total and transient-eddy horizontal transports, as well as the humidity advection. The total transports are given by the flux vector

$$\overline{uq}\,\mathbf{i} + \overline{vq}\,\mathbf{j}, \tag{3.11}$$

and the transient-eddy horizontal transports of humidity by

$$\overline{u'q'}\,\mathbf{i} + \overline{v'q'}\,\mathbf{j}. \tag{3.12}$$

the humidity advection being given by

$$-\overline{\mathbf{v} \bullet \nabla q}. \tag{3.13}$$

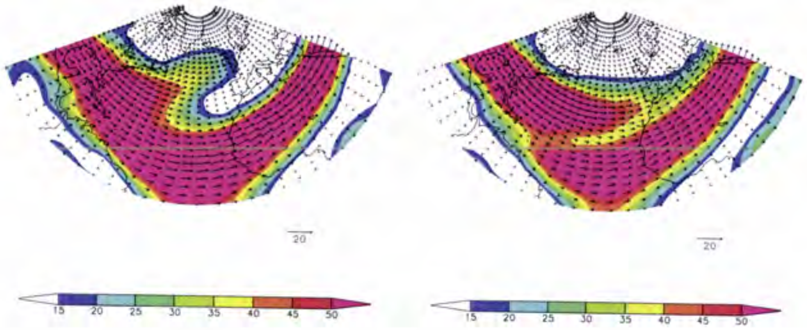

(a) (b)

Figure 3.30: Winter composite of the total horizontal transports of specific humidity in 10^{-1} g.kg^{-1}.m.s^{-1} at 300 hPa in the North Atlantic sector between 0°N-80°N and 100°W-40°E for (a) dry winters, and (b) wet winters. Shading represents the intensity of the fluxes, and arrows represent the horizontal fluxes.

The total horizontal transports of specific humidity reflect the mean wind patterns. For the wet winters, the almost zonal flow, transports moist air masses from the North Atlantic towards Portugal (Fig. 3.30(b)). These conditions are clearly favourable to the development of the different precipitation mechanisms.

For the dry winters, a northeastward deviation of the flow is observed (Fig. 3.30(a)). Consequently the main transports of humidity are deviated from the Iberian Peninsula and from Portugal. This behaviour is also observed for the humidity advection (Fig. 3.34(a)); these latter conditions are unfavourable for the establishment of rain-generating conditions over Portugal.

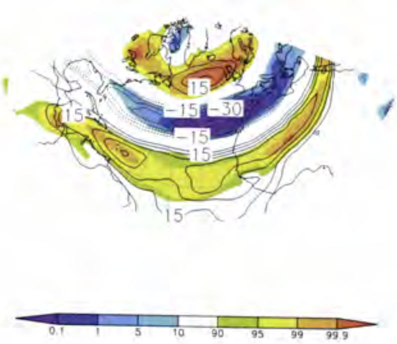

Figure 3.31: Difference of the total horizontal transports of specific humidity between dry and wet winters (contours) in 10^{-1} g.kg^{-1}.m.s^{-1} at 300 hPa and the corresponding p-values of the Student's t-test (shading) in the North Atlantic sector between 0°N-80°N and 100°W-40°E.

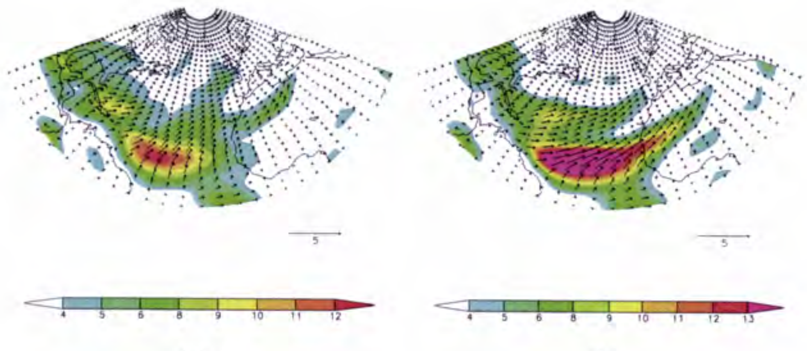

(a) (b)

Figure 3.32: Winter composite of the transient-eddy horizontal transports of specific humidity in 10^{-1} g.kg^{-1}.m.s^{-1} at 300 hPa in the North Atlantic sector between 0^{o}N-80^{o}N and 100^{o}W-40^{o}E for (a) dry winters, and (b) wet winters. Shading represents the intensity of the fluxes, and arrows represent the horizontal fluxes.

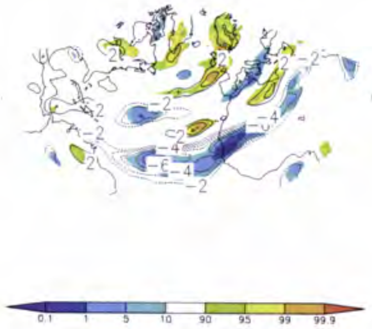

Figure 3.33: Difference of the transient-eddy horizontal transports of specific humidity between dry and wet winters (contours) in 10^{-1} g.kg^{-1}.m.s^{-1} at 300 hPa and the corresponding p-values of the Student's t-test (shading) in the North Atlantic sector between 0^{o}N-80^{o}N and 100^{o}W-40^{o}E.

The total horizontal transports difference pattern (Fig. 3.31) shows once again the tripole core of opposite signals, two positive cores with a negative core in between in the Iberian Peninsula latitude band. These facts enhance the importance of the humidity transports of the wet winters when comparing with the dry winters. This result was also obtained for the total transports of enthalpy and humidity.

The transient-eddy transports of humidity show an intense transport between 30^{o}N-40^{o}N, and 60^{o}W-40^{o}W, more relevant for the wet winters (Fig. 3.32(b)). This result is clearly corroborated by the negative core in the differences pattern (Fig. 3.33). A significant amount of this humidity is transported towards the North Africa, in both winters, and towards the Iberian Peninsula for the wet winters and towards the British Isles for the dry winters (Fig. 3.32(a)). Consequently, the humidity transports are deviated from Portugal, reflecting the blocking of the transient systems by the intensified North Atlantic ridge.

The precipitation in the western region of the Iberian Peninsula is associated to large-scale sea level pressure anomalies and to advection of humidity into this area. Negative sea level pressure anomaly over the North Atlantic (Fig. 3.5(b) and 3.6) induces an intensification of the westerly winds (Fig. 3.26(b) and 3.27), which are favourable conditions to trigger rain generation [Zorita et al., 1992]. The reduction of the westerly advection of humidity then causes a decrease of rainfall over Portugal. For the dry winters, the specific humidity advection

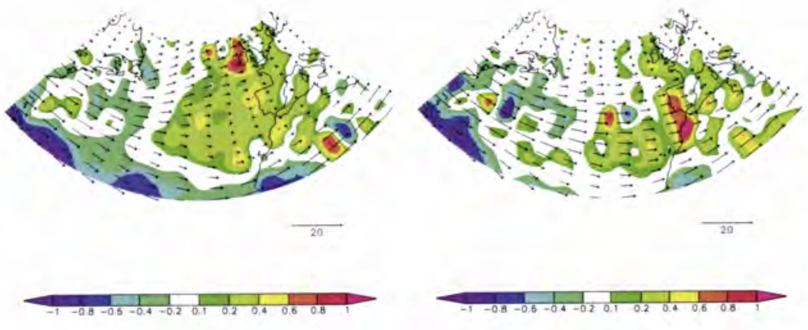

(a) (b)

Figure 3.34: Winter composite of the specific humidity advection in 10^{-1} g.kg^{-1}.day^{-1} at 300 hPa in the North Atlantic sector between 20^{o}N-60^{o}N and 80^{o}W-20^{o}E for (a) dry winters, and (b) wet winters. Shading represents the intensity of the fluxes, and arrows represent the horizontal fluxes.

pattern depicts an east-west dipolar structure over the North Atlantic, with negative values westwards of 40^{o}W and positive values eastwards (Fig. 3.34(a)). It is also worth mentioning the intensification of the advection of specific humidity in the western part of the Iberian Peninsula during wet winters (Fig. 3.34(b)). This result is plainly coherent with the presence of a strong North Atlantic ridge during extremely dry winters. Furthermore, due to the pronounced influence of NAO on precipitation over Iberia, it is expected that the increase in westerly advection is associated with low NAO index values [Ulbrich et al., 1999b].

3.1.9 Wind fields and the jet stream

The atmospheric flows plays a major role in transferring momentum, heat and moisture in the atmosphere. The winds are caused by different heating of the atmosphere. Therefore winds vary with locations, and with the seasons.

One of the most important particularities of the atmospheric flow is the existence of jet streams, strong narrow currents of vast-moving air in the upper atmosphere. Their paths have a meandering shapes oriented eastward. Each large-scale meander, or wave, within the jet is known as a Rossby wave. Jets are caused by strong horizontal gradients which take place across surfaces of discontinuities (Fig. 3.35), e.g., the transition between troposphere (where temperature decreases with height) and the stratosphere (where temperature increases with height) or frontal zones between cold (polar region) and warm air masses.

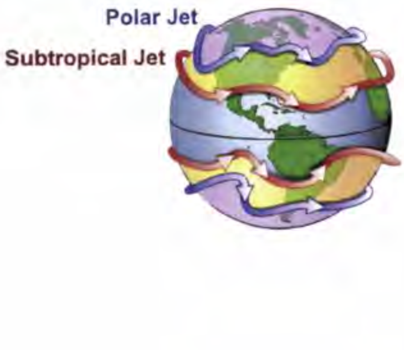

Figure 3.35: General configuration of the polar and subtropical jet streams (from NASA).

The jet streams were 'discovered' during the World War II, during the US air raids over Japan in 1944. The designation is attributed to Rossby, who previously studied the jets in water, although Seilkopf had introduced the German term Strahlströme in 1939 for upper strong winds, and the English Clement Ley in 1870s inferred the presence of very strong upper winds [Barry and Carleton, 2001]. There are two main jet streams (Fig. 3.35), one located northward of subtropical latitudes (approximately 30^{o}N depending the season), the subtropical jet, and another near the sub-polar latitudes, the eddy-driven jet stream.

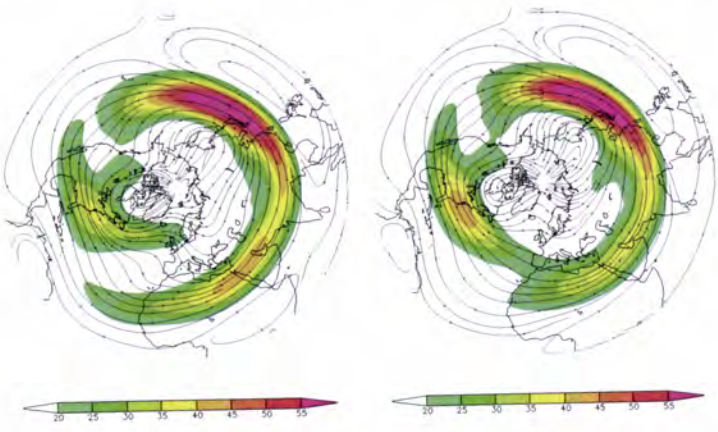

(a) (b)

Figure 3.36: Winter composite of the streamlines and wind intensity in m.s^{-1} at 300 hPa over the Northern Hemisphere between 0^{o}N-85^{o}N for (a) dry winters, and (b) wet winters. Shading represents the wind intensity, and arrows represent the streamlines.

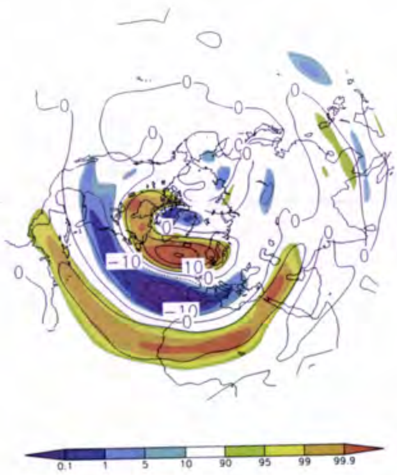

Figure 3.37: Difference of the streamlines and wind intensity between dry and wet winters (contours) in m.s^{-1} at 300 hPa and the corresponding p-values of the Student's t-test (shading) over the Northern Hemisphere between 0^{o}N-85^{o}N.

Since dry and wet winters in Portugal are a result of significant changes in the Northern hemisphere stationary wave pattern of the large-scale flow, this subsection is devoted to the study of the wind field and streamlines of the winter composites. As expected, the differences between dry and wet winters are clear, Figs. 3.36(a) and 3.36(b). It can be observed a strong zonal wind maxima near 30^{o}N throughout the Asian continent and North Pacific, as well as in the North American continent and northward of the Arabian Peninsula. Although these areas of maximum wind speed (jet streaks) are present in both composites, the major difference is located over the North Atlantic, where a difluence in the streamlines during the dry winters can be observed. Furthermore, for these winters, the mid-latitude westerly jet suffers an important difluence just eastward of North America and the sub-polar jet presents a significant tilt in its core. Besides, the sub-polar and subtropical jets are clearly separated for the dry winters, whereas this distinction is less pronounced for the wet winters; this clearly indicates that storm tracks in the dry and wet winters behave quite differently. Synoptic-scale disturbances tend to develop preferentially in the regions of maximum time-mean zonal winds associated with the western Pacific and western Atlantic jets and to propagate downstream along storm tracks that approximately follow the jet axes [Holton, 2004; Luo et al., 2007].

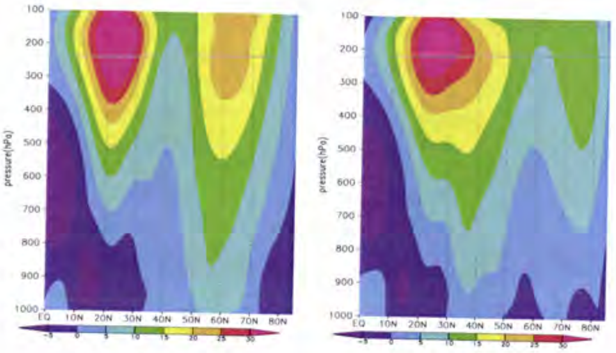

(a) (b)

Figure 3.38: Cross-sections of the winter composites of the zonal-mean wind component in m.s^{-1} at 300 hPa in the North Atlantic sector between 0^{o}N-85^{o}N and 60^{o}W-0^{o}E for (a) dry winters, and (b) wet winters.

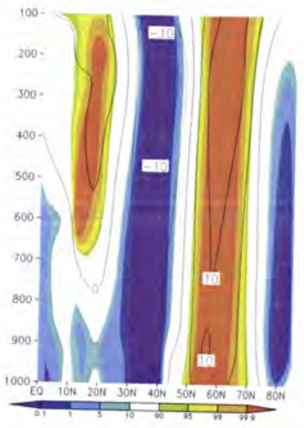

Figure 3.39: Difference of the winter composites of the zonal-mean wind component between dry and wet winters (contours) in m.s^{-1} at 300 hPa and the corresponding p-values of the Student's t-test (shading) in the North Atlantic sector between 0^{o}N-85^{o}N and 60^{o}W-0^{o}E.

As already stated, the most striking differences in the dry and wet winters are located in the North Atlantic (Fig. 3.37), where the significant statistical differences are located in these regions. Once more a tri-pole with opposite signals is observed. This result also corroborates the already referred strong relationship between winter precipitation in Portugal and large-scale atmospheric circulation.

The results attained for the zonal-mean cross-sections of the zonal wind component (Fig. 3.38) are also in clear agreement with the previous results. The core of maximum zonal wind speed (jet stream axis) is located just below the tropopause, about 30^oN, for the wet winters (Fig. 3.38(b)). Although this core is observed for the dry winters, another weaker core is still present near 60^oN. This suggest the presence of another branch of the jet stream. The strengthening of the subtropical jet for the dry winters is also clear through the observation of the difference pattern (Fig. 3.39). These results suggest not only that there are two jets over the North Atlantic during the dry winters, but also that the large-scale wave pattern is nearly barotropic equivalent. This equivalent barotropic structure can be inferred due to the almost absent vertical tilt in the maximum amplitude of the ridge throughout the troposphere [Santos et al., 2009b]. The splitting of the jet stream into two branches, corresponds to an intensification of the meridional component of the mid-tropospheric circulation. This intensification is usually accompanied by blocking, located in the vicinity of the British Isles [Barriopedro et al., 2006; Treidl et al., 1981]. Overall, the anomalous flow is not only linked to an enhancement (weakening) of the North Atlantic ridge but also to an enhancement (weakening) of the stationary eddies over the North Atlantic.

3.2 Dynamical analysis of the precursors of the EFF components

Changes in the winter time large-scale atmospheric circulations have a pronounced effect on regional distributions of surface temperature and precipitation. Anomalies in precipitation, are linked not only to the behaviour of the NAO, but are also accompanied by a northward shift of the storm tracks in association with synoptic eddy activity. As previously highlighted, the identification of the dynamical differences between the two contrasting conditions is essential to understand the large-scale mechanisms that commonly trigger the occurrence of drought episodes in Portugal. This anomalous flow is not only associated with the time-mean flow, but also with the transient motions. It is therefore important to analyse the local effect of these transient eddies on the stationary waves. This can be achieved through the evaluation of the contributions of the eddy transports of both heat and momentum. Along these lines, the patterns of the internal components of the EFF are presented and discussed. This methodology explores the role of local release of latent heat by the transient eddies and local transient transports of enthalpy and momentum in forcing large-scale asymmetries. Since the EFF can be separated into several physically significant components, as shown in chapter two, a separate descriptive analyses of the winter-mean values of these components and its internal structure is undertaken, before the analysis of the EFF itself.

3.2.1 Horizontal and vertical divergences of enthalpy

Since EFF1, component associated to friction and diabatic heating, encompasses horizontal and vertical fluxes of enthalpy, both mean and eddy fields will be analysed before presenting the EFF1.

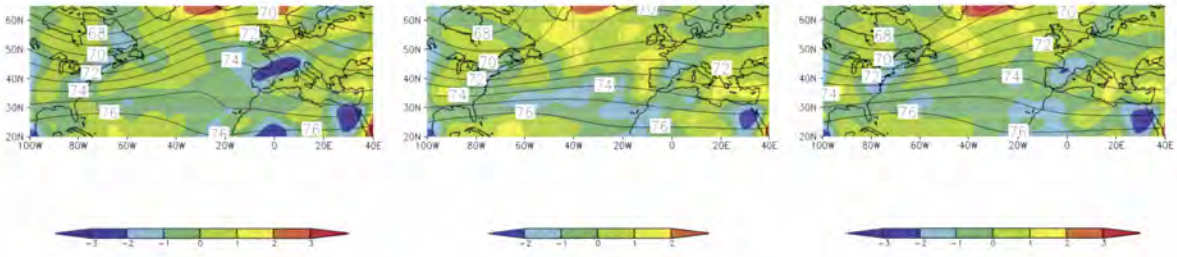

(a) (b) (c)

Figure 3.40: Winter composite of the vertically-averaged (500 − 300 hPa) mean horizontal divergence of enthalpy (shading) in 10^{-4} m.K.s^{-2} and the corresponding mean geopotential field (contours) in 10^{2} gpm in the North Atlantic sector between 20°N-65°N and 100°W-40°E for (a) dry winters, (b) wet winters, and (c) winter climatology.

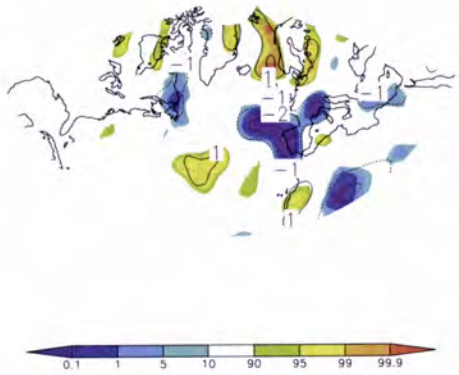

Figure 3.41: Difference of the vertically-averaged (500 – 300 hPa) mean horizontal divergence of enthalpy between dry and wet winters (contours) in 10^{-4} m.K.s^{-2} and the corresponding p-values of the Student's t-test (shading) in the North Atlantic sector between 20^{o}N-80^{o}N and 100^{o}W-40^{o}E.

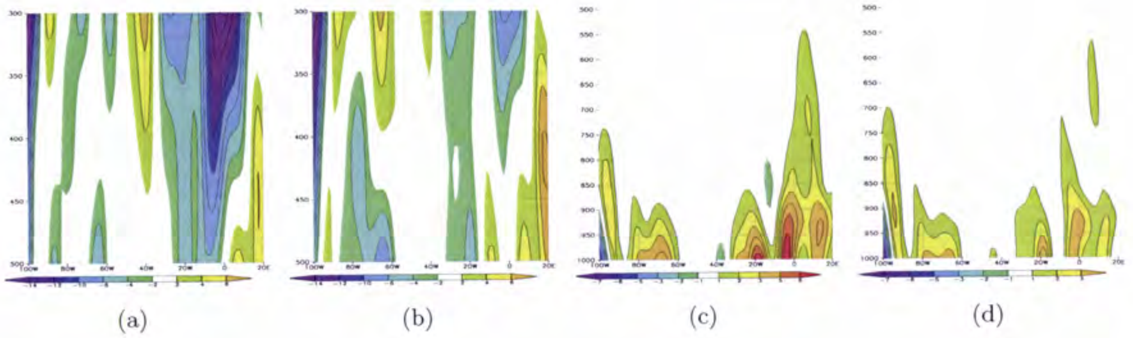
(a) (b) (c) (d)

Figure 3.42: Zonal cross-sections of the meridional-mean (20^{o}N-60^{o}N) of the mean horizontal divergence of enthalpy at 500 – 300 hPa in 10^{-5} m.K.s^{-2} in the North Atlantic between 100^{o}W-20^{o}E for (a) dry winters, and (b) wet winters, and at 1000 – 500 hPa in 10^{-4} m.K.s^{-2} for (c) dry winters, and (d) wet winters.

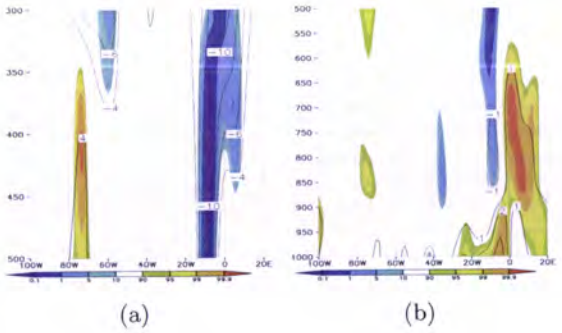
(a) (b)

Figure 3.43: Zonal cross-section of the difference of the meridional-mean (20^{o}N-60^{o}N) of the mean horizontal divergence of enthalpy between dry and wet winters (contours) at (a) 500 – 300 hPa in 10^{-5} m.K.s^{-2}, and (b) 1000 – 500 hPa in 10^{-4} m.K.s^{-2} and the corresponding p-values of the Student's t-test (shading) in the North Atlantic sector between 100^{o}W-20^{o}E.

The mean horizontal divergence fields of the enthalpy transport, $\frac{\partial \bar{u}\bar{T}}{\partial x} + \frac{\partial \bar{v}\bar{T}}{\partial y}$, displayed in Fig. 3.40, show for the dry winters an intensification of the enthalpy flux, upstream of the ridge, when compared with the wet winters and with the winter climatology. Moreover, the mean horizontal divergence of enthalpy transport is displaced northeastward (Fig 3.40(a)) when comparing with the almost zonal distribution during the wet winters (Fig. 3.40(b)). The difference pattern (Fig. 3.41) depicts a significant increase of the divergence of the enthalpy transport in middle latitudes over eastern and central Europe for the dry winters, contrasting with the decrease observed in higher latitudes [Andrade et al., 2008b, d]. The meridional-mean zonal cross-sections of the divergence of the enthalpy transport for the lower troposphere (Figs. 3.42(c) and 3.42(d)) are one order of magnitude higher than aloft (Figs. 3.42(a) and 3.42(b)). The higher values at the lower troposphere are expected, since the influence of the continents and oceans diminishes with height. The strongest divergence of the enthalpy transport values are found between 20^oW and 0^oE and are most intense during the dry winters.

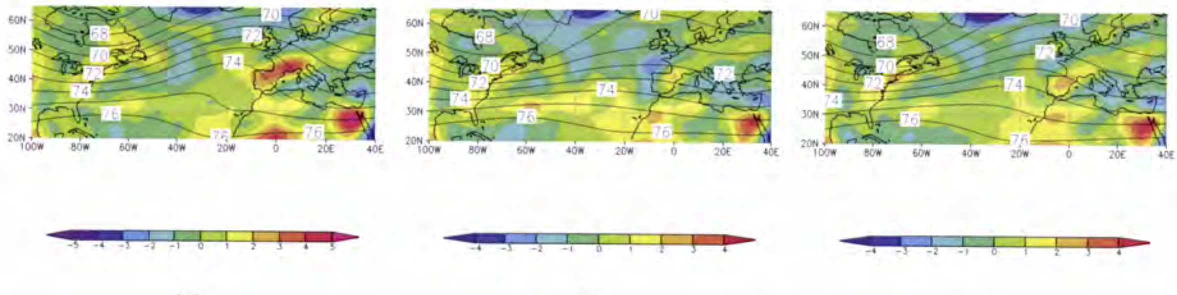

(a) (b) (c)

Figure 3.44: Winter composite of the vertically-averaged (500 − 300 hPa) mean vertical transports of enthalpy (shading) in 10^{-4} m.K.s^{-2} and the corresponding mean geopotential field (contours) in 10^2 gpm in the North Atlantic sector between 20^oN-65^oN and 100^oW-40^oE for (a) dry winters, (b) wet winters, and (c) winter climatology.

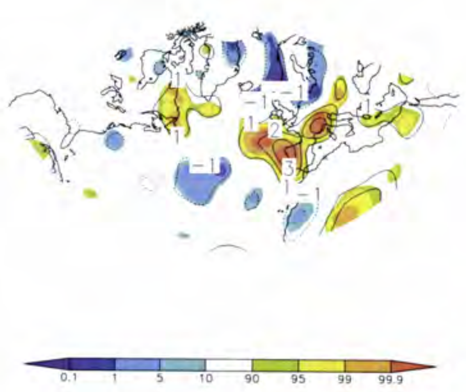

Figure 3.45: Difference of the vertically-averaged (500 − 300 hPa) mean vertical transports of enthalpy between dry and wet winters (contours) in 10^{-4} m.K.s^{-2} and the corresponding p-values of the Student's t-test (shading) in the North Atlantic sector between 20^oN-80^oN and 100^oW-40^oE.

When comparing Figs. 3.42(a), 3.42(b) with Figs. 3.42(c), 3.42(d), a rapid decrease of the mean-meridional divergence of enthalpy transports can be observed throughout the troposphere with reverse conditions present at higher levels.

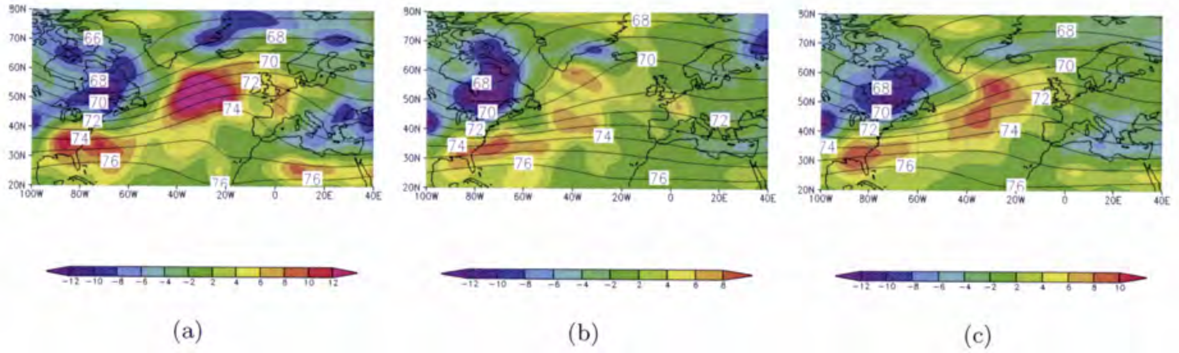

(a) (b) (c)

Figure 3.46: Winter composite of the vertically-averaged (500 – 300 hPa) mean eddy-horizontal divergence of enthalpy (shading) in 10^{-6} m.K.s^{-2} and the corresponding mean geopotential field (contours) in 10^{2} gpm in the North Atlantic sector between 20^{o}N-80^{o}N and 100^{o}W-40^{o}E for (a) dry winters, (b) wet winters, and (c) winter climatology.

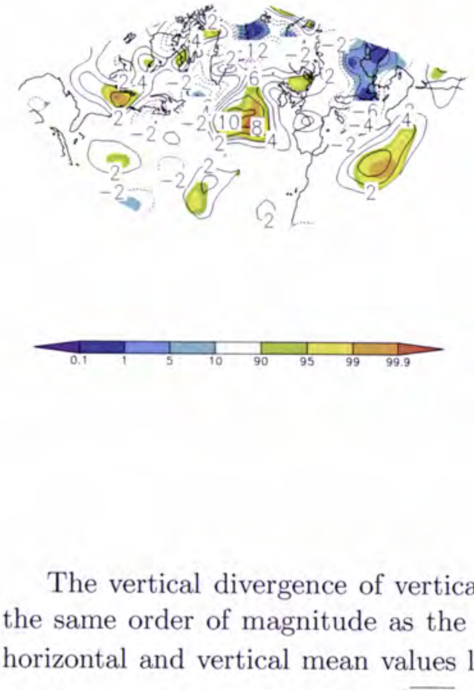

Figure 3.47: Difference of the vertically-averaged (500 – 300 hPa) mean eddy-horizontal divergence of enthalpy between dry and wet winters (contours) in 10^{-6} m.K.s^{-2} and the corresponding p-values of the Student's t-test (shading) in the North Atlantic sector between 20^{o}N-80^{o}N and 100^{o}W-40^{o}E.

The vertical divergence of vertical enthalpy transport, $\frac{\partial \overline{\omega T}}{\partial p}$, displayed in Fig. 3.44, has the same order of magnitude as the mean horizontal divergence of enthalpy. However, the horizontal and vertical mean values largely exceed the horizontal, $\frac{\partial \overline{u'T'}}{\partial x} + \frac{\partial \overline{v'T'}}{\partial y}$ and vertical divergence of eddy transports, $\frac{\partial \overline{\omega' T'}}{\partial p}$, (Figs. 3.46 and 3.48) as expected, since the eddy transports represent the transient eddies. The latter fields although being two orders of magnitude weaker, are nevertheless very important for the large-scale circulation of the atmosphere. It is interesting to note that the main findings described earlier for the mean fields are also present in both horizontal and vertical eddy fields (Figs. 3.46 and 3.48). The dry winter patterns are also more intense upstream of the ridge than for the wet and winter climatologies. This result is thus plainly coherent with the maintenance of a strong North Atlantic ridge during extremely dry winters.

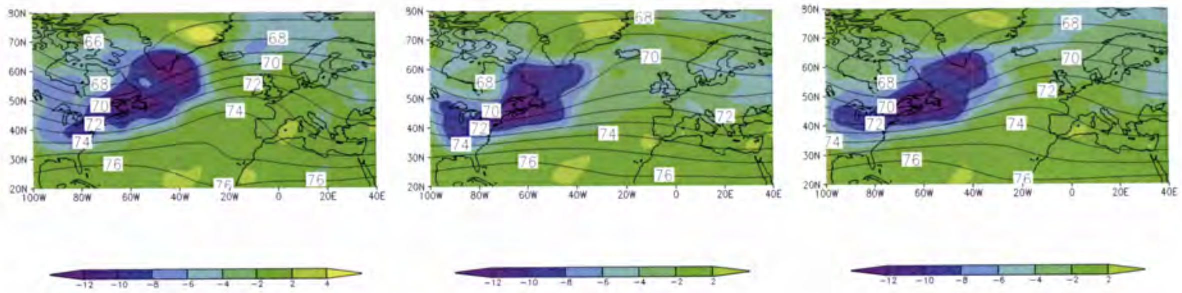
80N
70N
60N
50N
40N
30N
20N
100W
80W
60W
40W
20W
0
20E
40E
66
68
70
72
74
76
−12
−10
−8
−6
−4
−2
2
4

(a) (b) (c)

Figure 3.48: Winter composite of the vertically-averaged (500 − 300 hPa) mean eddy-vertical transports of enthalpy (shading) in 10^{-6} m.K.s^{-2} and the corresponding mean geopotential field (contours) in 10^{2} gpm in the North Atlantic sector between 20^{o}N-80^{o}N and 100^{o}W-40^{o}E for (a) dry winters, (b) wet winters, and (c) winter climatology.

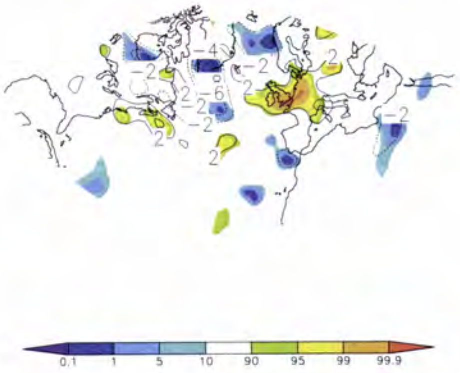
−4
−2
−6
2
0.1
1
5
10
90
95
99
99.9

Figure 3.49: Difference of the vertically-averaged (500 − 300 hPa) mean eddy-vertical transports of enthalpy between dry and wet winters (contours) in 10^{-6} m.K.s^{-2} and the corresponding p-values of the Student's t-test (shading) in the North Atlantic sector between 20^{o}N-80^{o}N and 100^{o}W-40^{o}E.

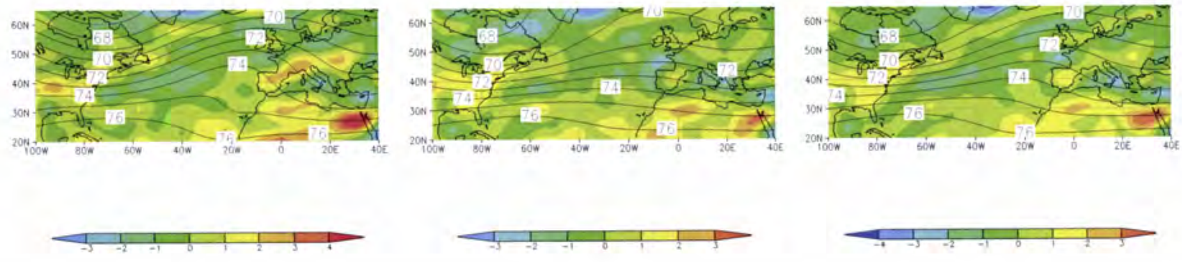
60N
50N
40N
30N
20N
100W
80W
60W
40W
20W
0
20E
40E
68
70
72
74
76
−4
−3
−2
−1
0
1
2
3
4

(a) (b) (c)

Figure 3.50: Winter composite of the vertically-averaged (500 − 300 hPa) mean divergence of enthalpy (shading) in 10^{-5} m.K.s^{-2} and the corresponding mean geopotential field (contours) in 10^{2} gpm in the North Atlantic sector between 20^{o}N-65^{o}N and 100^{o}W-40^{o}E for (a) dry winters, (b) wet winters, and (c) winter climatology.

The field resulting from the sum of the both mean and eddy horizontal and vertical divergence of the enthalpy transport fields (Fig. 3.50) shows a nearly zonal distribution of the convergence values for the wet winters (Fig. 3.50(b)). This pattern is clearly contrasting with the dry winter pattern, where a convergence area is observed upstream of the ridge and a divergence area downstream of the intense ridge. The referred convergence area is once more displaced northeastward. These results are clearly unfavourable to the occurrence of rain-generation weather systems over Portugal. The difference between the two winter composites (Figs. 3.50(c) and 3.51) clearly reflects this contrasting behaviour.

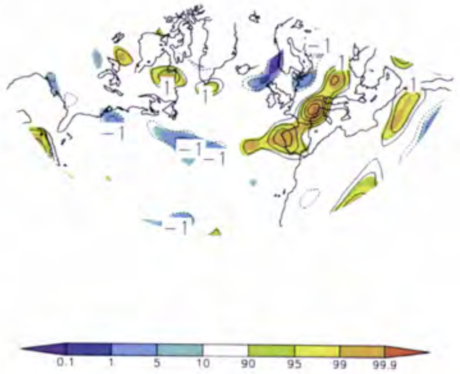

Figure 3.51: Difference of the vertically-averaged (500 – 300 hPa) mean divergence of enthalpy between dry and wet winters (contours) in 10^{-5} m.K.s^{-2} and the corresponding p-values of the Student's t-test (shading) in the North Atlantic sector between 20^{o}N-80^{o}N and 100^{o}W-40^{o}E.

3.2.2 Horizontal and vertical divergences of humidity

Following the same methodology as in the previous section, the horizontal and vertical divergence of humidity transport embedded in EFF2, component associated with the latent heat release, is analysed for the mean and transient contributions. The mean horizontal and vertical divergences of the humidity transport fields were computed following, $\frac{\partial \overline{uq}}{\partial x} + \frac{\partial \overline{vq}}{\partial y}$, and $\frac{\partial \overline{\omega q}}{\partial p}$.

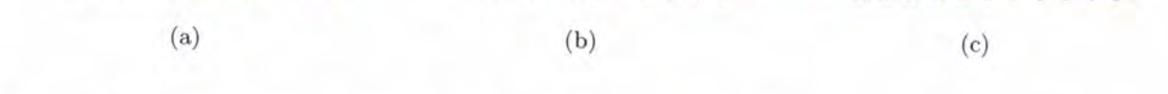

(a) (b) (c)

Figure 3.52: Winter composite of the vertically-averaged (500 – 300 hPa) mean horizontal divergence of humidity (shading) in 10^{-10} m.s^{-2} and the corresponding mean geopotential field (contours) in 10^2 gpm in the North Atlantic sector between 20^{o}N-80^{o}N and 100^{o}W-40^{o}E for (a) dry winters, (b) wet winters, and (c) winter climatology.

The divergence fields of the humidity transports are highly relevant for this study, since they allow the identification of the regions that constitute sources (sinks) of humidity. The divergence regions (positive values) are associated with source regions, whereas convergence regions (negative values) are associated with atmospheric sink regions.

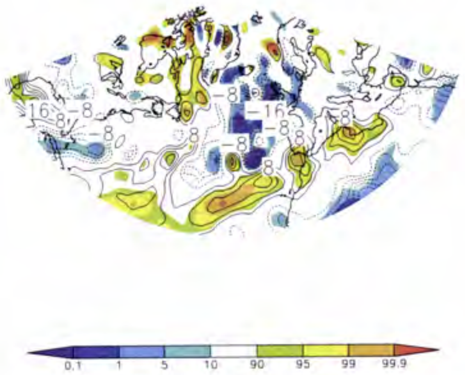

Figure 3.53: Difference of the vertically-averaged ($500 - 300$ hPa) mean horizontal divergence of humidity between dry and wet winters (contours) in 10^{-10} m.s^{-2} and the corresponding p-values of the Student's t-test (shading) in the North Atlantic sector between 20^oN-80^oN and 100^oW-40^oE.

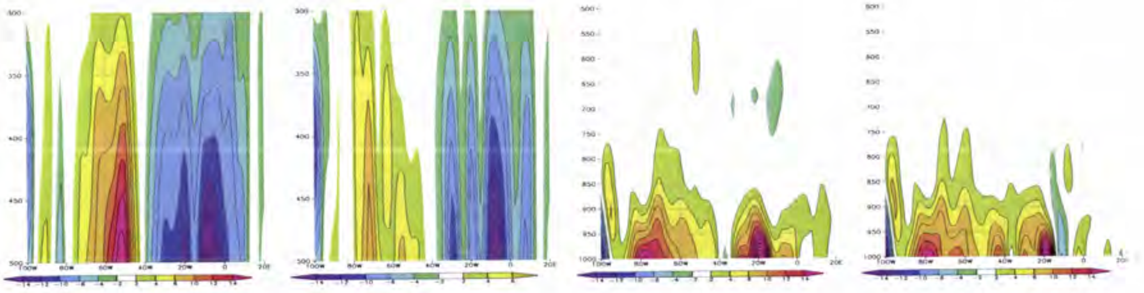

(a) (b) (c) (d)

Figure 3.54: Zonal cross-sections of the meridional-mean (20^oN-60^oN) of the mean horizontal divergence of humidity at $500 - 300$ hPa in 10^{-10} m.s^{-2} in the North Atlantic between 100^oW-20^oE for (a) dry winters, and (b) wet winters, and at $1000 - 500$ hPa in 10^{-9} m.s^{-2} for (c) dry winters, and (d) wet winters.

The mean horizontal divergence of the humidity transports (Fig. 3.52) shows a pattern that resembles the mean horizontal divergence of the enthalpy transport (Fig. 3.40). This results from the fact that the ability of the atmosphere to retain humidity depends strongly on temperature. Therefore, in the divergence regions evaporation exceeds the precipitation, and hence it is expected that the areas of maximum divergence occur not only along the storm track path, but also in maximum diabatic heating regions. The dry winter pattern (Fig. 3.52(a)) depicts an east-west dipolar structure with positive values westward of 40^oW and negative values eastward. This clear separation between divergence and convergence, respectively upstream and downstream of the ridge (Fig. 3.52(a)) is still devised for winter climatology (Fig. 3.52(c)), but contrast with the wet winter pattern (Fig. 3.52(b)). This pattern was also present in the specific humidity advection pattern (Fig. 3.34). The location of positive divergence indicates an important source region and coincide with a well-known cyclogenesis area [Basset and Ali, 2006]. Significant differences are found over western and central Europe (Fig. 3.53), where positive nuclei suggests the prevalence of convergence over divergence, leading to a surplus of precipitation on the wet winters.

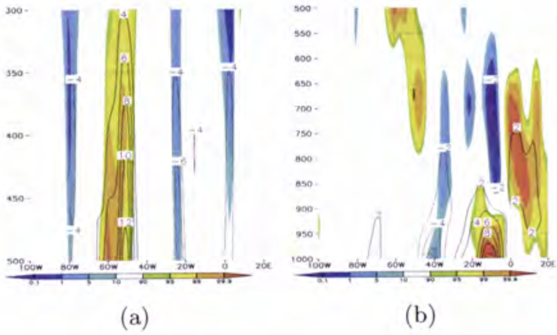
(a) (b)

Figure 3.55: Zonal cross-section of the difference of the meridional-mean (20^{o}N-60^{o}N) horizontal divergence of humidity between dry and wet winters (contours) at (a) $500-300$ hPa in 10^{-10} m.s^{-2}, and at (b) $1000-500$ hPa in 10^{-9} m.s^{-2} and the corresponding p-values of the Student's t-test (shading) in the North Atlantic sector between 100^{o}W-20^{o}E.

The zonal cross-section of the mean-meridional horizontal divergence of humidity is one order of magnitude higher in the lower troposphere when compared with the values observed in the higher troposphere. These results are expected, since specific humidity decreases rapidly with height. Usually, the maximum values in the lower troposphere occur since evaporation exceeds precipitation in the planetary boundary layer (Figs. 3.54(c) and 3.54(d)). At the higher troposphere, maximum values are found over the North Atlantic, being more intense for the dry winters (Fig. 3.54(a)).

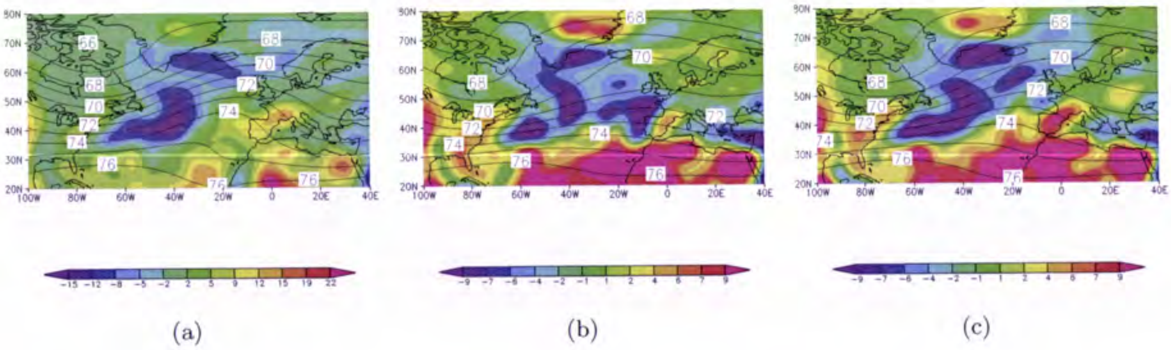
(a) (b) (c)

Figure 3.56: Winter composite of the vertically-averaged $(500-300$ hPa) mean vertical transports of humidity (shading) in 10^{-10} m.s^{-2} and the corresponding mean geopotential field (contours) in 10^2 gpm in the North Atlantic sector between 20^{o}N-80^{o}N and 100^{o}W-40^{o}E for (a) dry winters, (b) wet winters, and (c) winter climatology.

Contrasting with the case of enthalpy fields presented in the latter section, both horizontal and vertical divergences of the transports of humidity are relevant. For dry winters (Fig. 3.56(a)), negative values are observed upstream of the enhanced ridge, which results in an northward flux of humidity. This maximum northward flux is associated with low-pressure systems that, due to the northward displacement of this core are driven away from the Iberian Peninsula. This behaviour highly contrasts with the wet winters (Fig. 3.56(b)) and is clearly observed in the difference pattern (Fig. 3.57), in which the downward flux occurs where subsidence prevails.

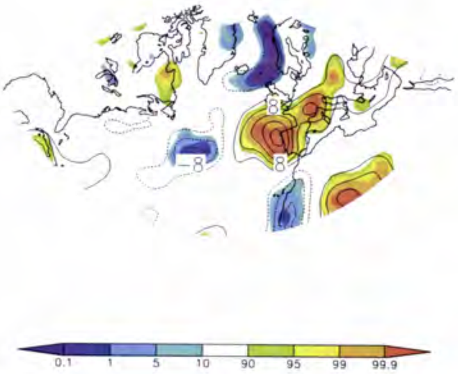

Figure 3.57: Difference of the vertically-averaged $(500-300$ hPa) mean vertical transports of humidity between dry and wet winters (contours) in 10^{-10} m.s^{-2} and the corresponding p-values of the Student's t-test (shading) in the North Atlantic sector between 20^{o}N-80^{o}N and 100^{o}W-40^{o}E.

As stated above, the transient-eddy humidity fluxes are as important as the mean transports. The divergence of the mean eddy transports of humidity $\frac{\partial \overline{u'q'}}{\partial x} + \frac{\partial \overline{v'q'}}{\partial y}$ revealed, for the dry winters in the North Atlantic, a strong negative and positive centres located respectively of the trough and ridge of the geopotential field (Fig. 3.58(a)) that highly contrast with the undefined pattern observed for both wet (Fig. 3.58(b)) and winter climatologies (Fig. 3.58(c)). The difference pattern is statistically meaningful over the Iberian Peninsula (Fig. 3.59).

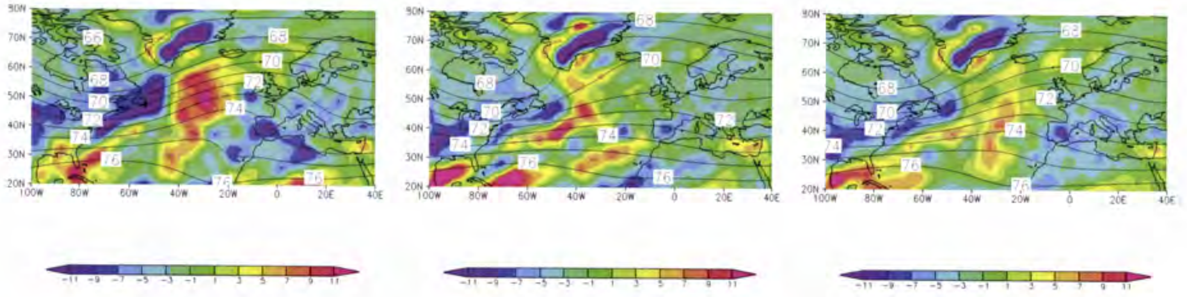

(a) (b) (c)

Figure 3.58: Winter composite of the vertically-averaged (500 $-$ 300 hPa) mean eddy-horizontal divergence of humidity (shading) in 10^{-10} m.s^{-2} and the corresponding mean geopotential field (contours) in 10^2 gpm in the North Atlantic sector between 20^{o}N-80^{o}N and 100^{o}W-40^{o}E for (a) dry winters, (b) wet winters, and (c) winter climatology.

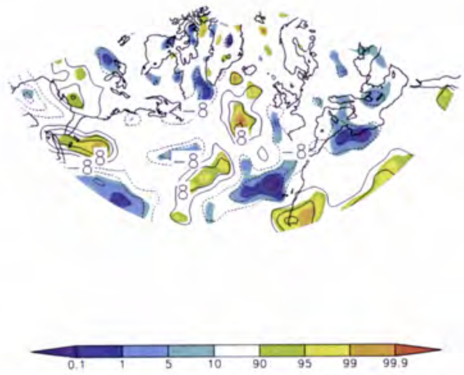

Figure 3.59: Difference of the vertically-averaged ($500-300$ hPa) mean eddy-horizontal divergence of humidity between dry and wet winters (contours) in 10^{-10} m.s^{-2} and the corresponding p-values of the Student's t-test (shading) in the North Atlantic sector between 20^{o}N-80^{o}N and 100^{o}W-40^{o}E.

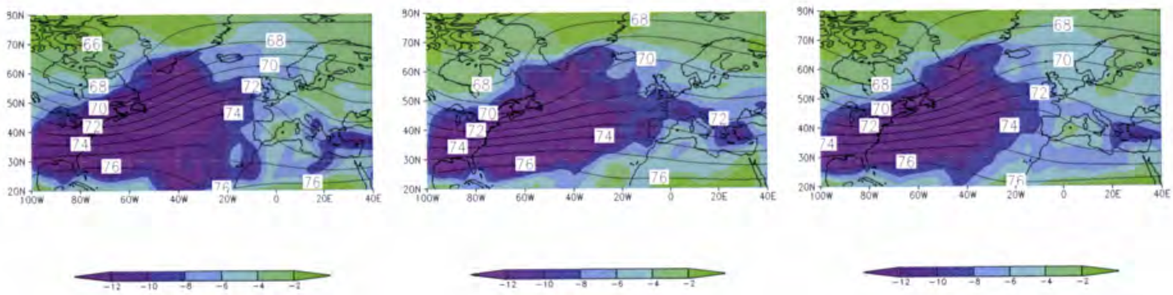

(a) (b) (c)

Figure 3.60: Winter composite of the vertically-averaged ($500-300$ hPa) mean eddy-vertical transports of humidity (shading) in 10^{-10} m.s^{-2}, and the corresponding mean geopotential field (contours) in 10^2 gpm in the North Atlantic sector between 20^{o}N-80^{o}N and 100^{o}W-40^{o}E for (a) dry winters, (b) wet winters, and (c) winter climatology.

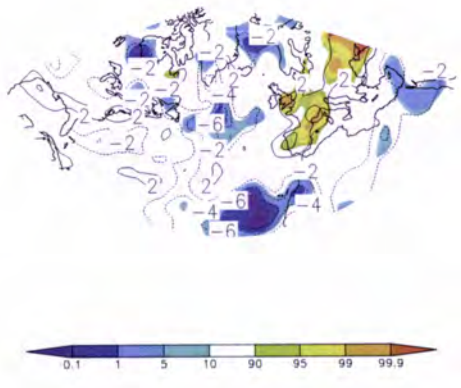

Figure 3.61: Difference of the vertically-averaged ($500-300$ hPa) mean eddy-vertical transports of humidity between dry and wet winters (contours) in 10^{-10} m.s^{-2} and the corresponding p-values of the Student's t-test (shading) in the North Atlantic sector between 20^{o}N-80^{o}N and 100^{o}W-40^{o}E.

The divergence of the eddy-vertical transports of humidity $\frac{\partial \overline{\omega' q'}}{\partial p}$ shows an intense negative region over the North Atlantic ridge (Fig. 3.60), indicating an upward humidity flux expanding towards the Iberian Peninsula for the wet winters (Fig. 3.60(b)). In this region the difference is statistically relevant (Fig. 3.61). However, being as important as the mean transports, the transient eddy transports seem to oppose the latter.

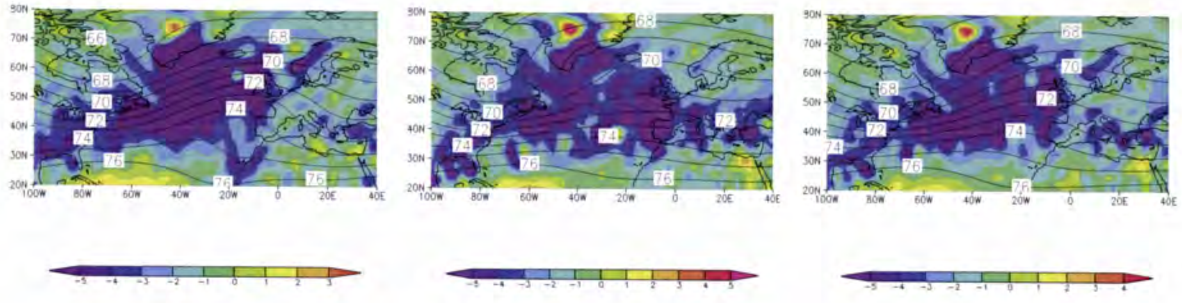

(a) (b) (c)

Figure 3.62: Winter composite of the vertically-averaged (500 − 300 hPa) mean divergence of humidity (shading) in 10^{-10} m.s^{-2}, and the corresponding mean geopotential field (contours) in 10^{2} gpm in the North Atlantic sector between 20^{o}N-80^{o}N and 100^{o}W-40^{o}E for (a) dry winters, (b) wet winters, and (c) winter climatology.

On the whole, the sum of all of the previous contributions result in a humidity field pattern (Fig. 3.62) that depicts the influence of the eddy-vertical transports of humidity. In fact, the middle and high latitude convergences are mainly associated with the transient baroclinic lows along the polar front. This result is consistent with the wet winters (Fig. 3.62(b)) and the differences patterns (Fig. 3.63).

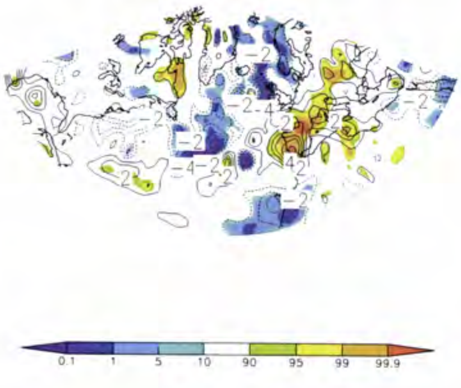

Figure 3.63: Difference of the vertically-averaged (500 − 300 hPa) mean divergence of humidity between dry and wet winters (contours) in 10^{-10} m.s^{-2} and the corresponding p-values of the Student's t-test (shading) in the North Atlantic sector between 20^{o}N-80^{o}N and 100^{o}W-40^{o}E.

3.2.3 Rates of heat addition

It is well known that differential heating plays an important role in cyclogenesis, especially the cyclogenesis associated with the generation of cold waves in a cold front, associated with cold synoptic anticyclones in the rear of the front. Indeed, the pioneer theory of Sutcliffe [1947] stated that both heating between the surface and the level of nondivergence, as well as, vorticity advection aloft are major contributers to surface cyclogenesis. Since the preferred locations of the cyclone development are concentrated near the maximum diabatic heating regions [Lin, 1989], it is expected that the diabatic heating fields of both winter composites will provide a valuable physical insight into the problem. In particular, both the rate of heat addition per unit mass due to condensation, $\overline{\dot{q}_L}$ (2.50), embedded in EFF2, and the total rate of heat addition, $\overline{\dot{q}} = \overline{\dot{q}_F + \dot{q}_R + \dot{q}_L}$ (2.51), present in EFF1, are analysed here. Both components of EFF1 (2.43) and EFF2 (2.44), are indirectly computed, as previously mentioned, from the energy conservation equation (2.14) and from the water vapour continuity equation, respectively.

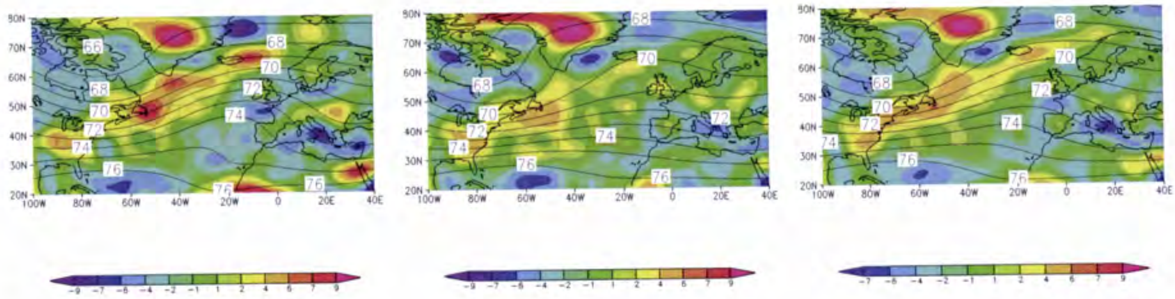

(a) (b) (c)

Figure 3.64: Winter composite of the vertically-averaged (500 − 300 hPa) total rate of heat addition (shading) in 10^{-2} J.s^{-1}, and the corresponding mean geopotential field (contours) in 10^{2} gpm in the North Atlantic sector between 20^{o}N-80^{o}N and 100^{o}W-40^{o}E for (a) dry winters, (b) wet winters, and (c) winter climatology.

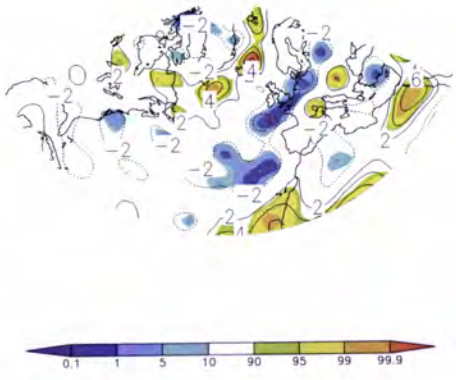

Figure 3.65: Difference of the vertically-averaged (500 − 300 hPa) total rate of heat addition between dry and wet winters (contours) in 10^{-2} J.s^{-1} and the corresponding p-values of the Student's t-test (shading) in the North Atlantic sector between 20^{o}N-80^{o}N and 100^{o}W-40^{o}E.

The dry winter pattern of the total rate of heat addition, (Fig. 3.64(a)) underlies the enhanced positive forcing in the region upstream of the ridge. These results are also in clear accordance with the results presented for the convergence of the transient transports of enthalpy, since this pattern reflects the large region of enthalpy convergence previously shown. The heat sink is associated with a downward diabatic mass transport. These results are in clear agreement with the results attained by Lin [1989]. This pattern is also very similar to the pattern associated with the rate of heat addition due to latent heat release (Fig. 3.66(a)). It is expected that these regions will also correspond to the position of the core of the storm track. This correspondence is physically coherent with high precipitation rates (subsection 3.1., Fig. 3.1) and cloudiness that are commonly found along the storm track, where significant amounts of latent heat are released by water vapour condensation (deposition). Indeed the wet winter maxima of the rate heat addition due to condensation, are located over the Iberian Peninsula (Fig. 3.66(b)).

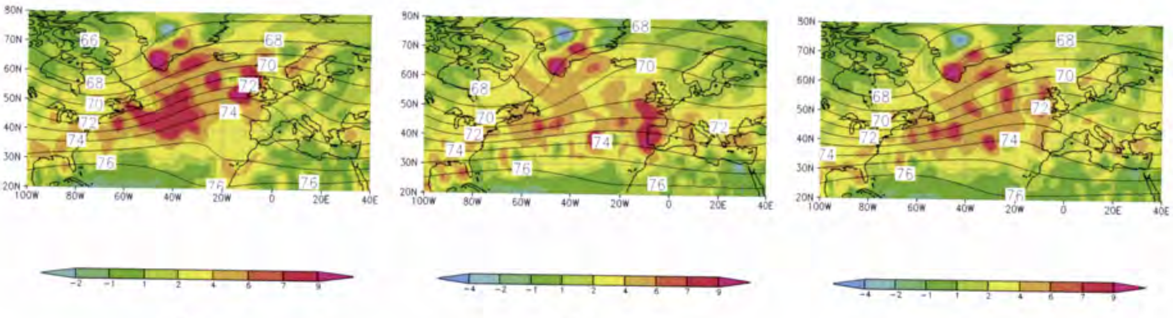

(a) (b) (c)

Figure 3.66: Winter composite of the vertically-averaged (500 − 300 hPa) rate of heat addition, per unit mass, due to condensation (shading) in 10^{-3} J.s^{-1}, and the corresponding mean geopotential field (contours) in 10^2 gpm in the North Atlantic sector between 20^{o}N-80^{o}N and 100^{o}W-40^{o}E for (a) dry winters, (b) wet winters, and (c) winter climatology.

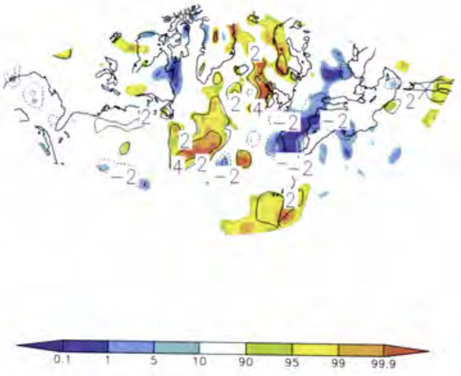

Figure 3.67: Difference of the vertically-averaged (500 − 300 hPa) rate of heat addition, per unit mass, due to condensation between dry and wet winters (contours) in 10^{-3} J.s^{-1} and the corresponding p-values of the Student's t-test (shading) in the North Atlantic sector between 20^{o}N-80^{o}N and 100^{o}W-40^{o}E.

3.2.4 Vorticity fields

Forescasting and interpretation of midlatitude cyclonic and anticyclonic activity constitutes an important field of meteorological research. The ability and accuracy to forecast implies a better diagnostic framework in which the study of cyclogenesis is relevant. One approach is to diagnose developments in terms of conserved quantities (or locally conserved), such as absolute vorticity, and provided the necessary conditions are fulfilled (e.g., non-divergent barotropic flow); the invertibility principle will then allow the recovery of the exact flow field. Moreover, the assumption of a dynamically balanced flow encloses the dynamics of the extratropical cyclones into a potential vorticity framework, since potential vorticity is a conserved quantity [Davis and Emanuel, 1991].

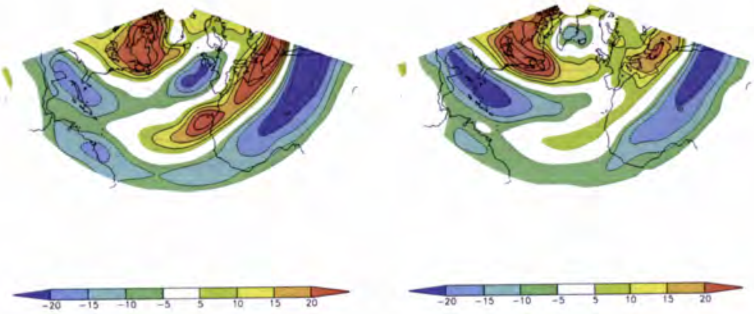

(a)

(b)

Figure 3.68: Winter composite of the vertical component of the relative vorticity (shading) in 10^{-6} s^{-1} at 300 hPa in the North Atlantic sector between 0^{o}N-80^{o}N and 100^{o}W-40^{o}E for (a) dry winters, (b) wet winters, and (c) winter climatology.

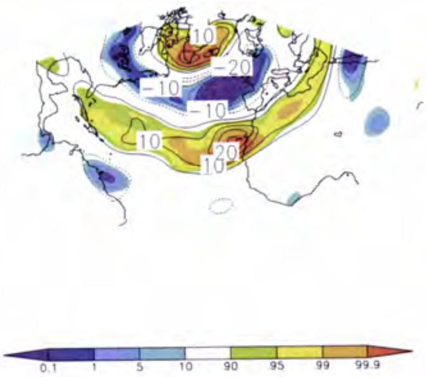

Figure 3.69: Difference of the vertical component of the relative vorticity between dry and wet winters (contours) in 10^{-6} s^{-1} at 300 hPa and the corresponding p-values of the Student's t-test (shading) in the North Atlantic sector between 0^{o}N-80^{o}N and 100^{o}W-40^{o}E.

When a rotating atmospheric column remains at the same latitude, only changes in the height of the column can affect the absolute vorticity. In the Northern Hemisphere, shrinking of the column (subsidence) is associated with the divergent flow at low levels. This divergent flow is then transformed by the Coriolis force into an anticyclonic circulation which is associated with negative relative vorticity. On the other hand, vertical stretching of the column causes inward motion at low levels. In this case, the Coriolis force transforms this motion into an cyclonic circulation, associated to positive relative vorticity [Holton, 2004].

There is a clear distinction between the dry and the wet winters, depicted in Figs. 3.68(a) and 3.68(b). In dry winters, a region of negative relative vorticity can be found northwestward of the Iberian Peninsula, while to the south an area of opposite signal can be observed. The wet winters show a more zonal distribution. Two bands of negative relative vorticity are present in the tropical and subtropical regions, followed by a more northward positive band.

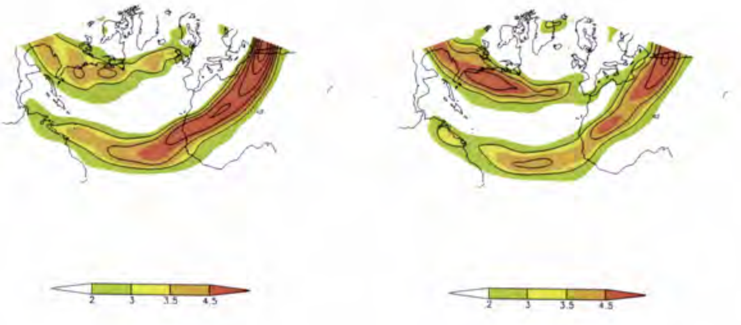

(a) (b)

Figure 3.70: Winter composite of the mean meridional gradient of the absolute vorticity (shading) in 10^{-11} $m^{-1}.s^{-1}$ at 300 hPa in the North Atlantic sector between 0^oN-80^oN and 100^oW-40^oE for (a) dry winters, and (b) wet winters.

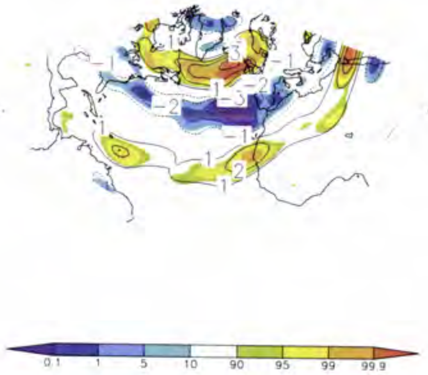

Figure 3.71: Difference of the mean meridional gradient of the absolute vorticity between dry and wet winters (contours) in 10^{-11} $m^{-1}.s^{-1}$ at 300 hPa and the corresponding p-values of the Student's t-test (shading) in the North Atlantic sector between 0^oN-80^oN and 100^oW-40^oE.

The presence of anticyclones or cyclones northwestward of Portugal is clearly linked to the occurrence of dry or wet winters, respectively. Moreover, the vorticity over Portugal is not a good indicator of the precipitation extremes. In fact, precipitation extremes in Portugal tend to occur in association with remote synoptic systems, rather then being associated with local systems.

The analysis of the meridional gradient of absolute vorticity at 300 hPa, reveals the existence in the North Atlantic sector of a wide area of positive values in the mid-latitudes, wider in range (extended towards the Iberian Peninsula) for the wet winters (Fig. 3.70(b)). This can indicate a shift of the jet towards the British Isles during the dry winters, in contrast with a more zonal trajectory for wet winters. The differences in both winters show once more a tri-pole pattern; two negative areas with a positive one in between (Fig. 3.71).

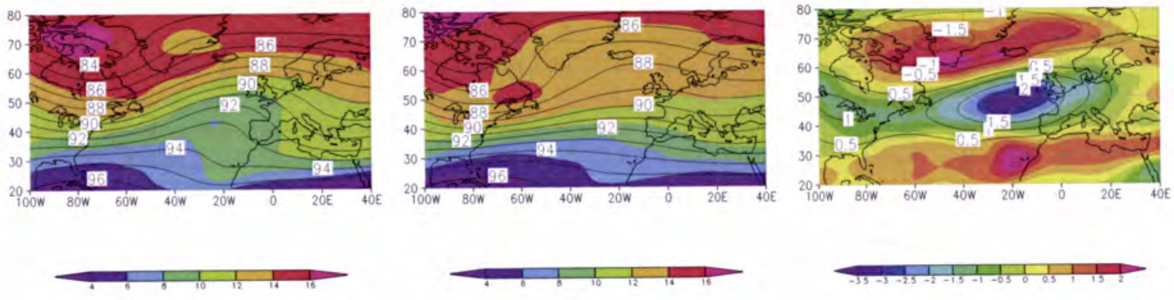
80
70
60
50
40
30
20
100W
80W
60W
40W
20W
0
20E
40E
84
86
88
90
92
94
96
4
6
8
10
12
14
16
-1.5
-1
-0.5
0.5
1
1.5
2
-3.5 -3 -2.5 -2 -1.5 -1 -0.5 0 0.5 1 1.5 2

(a) (b) (c)

Figure 3.72: Winter composite of the absolute vorticity (shading) in 10^{-5} s^{-1} at 300 hPa and the corresponding mean geopotential field (contours) in 10^2 gpm in the North Atlantic sector between 0^oN-80^oN and 100^oW-40^oE for (a) dry winters, (b) wet winters, and (c) difference between dry and wet winters.

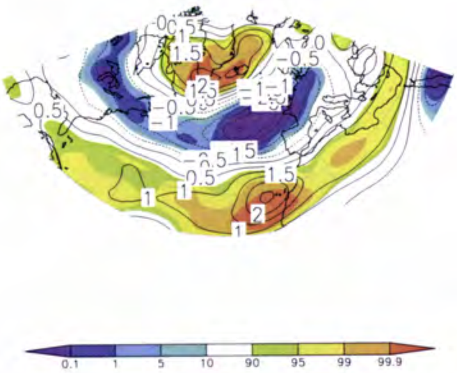
0.5
1
1.5
2
-0.5
-1
0.1
1
5
10
90
95
99
99.9

Figure 3.73: Difference of the absolute vorticity between dry and wet winters (contours) in 10^{-5} s^{-1} at 300 hPa and the corresponding p-values of the Student's t-test (shading) in the North Atlantic sector between 0^oN-80^oN and 100^oW-40^oE.

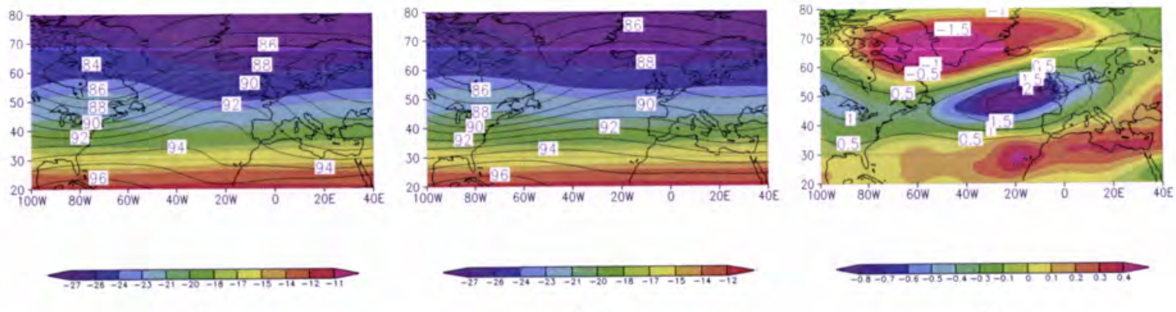
80
70
60
50
40
30
20
100W
80W
60W
40W
20W
0
20E
40E
84
86
88
90
92
94
96
-27 -26 -24 -23 -21 -20 -18 -17 -15 -14 -12 -11
-1.5
-1
-0.5
0.5
1
1.5
-0.8 -0.7 -0.6 -0.5 -0.4 -0.3 -0.1 0 0.1 0.2 0.3 0.4

(a) (b) (c)

Figure 3.74: Winter composite of the potential vorticity (shading) in 10^{-4} s^{-1} at 300 hPa and the corresponding mean geopotential field (contours) in 10^2 gpm in the North Atlantic sector between 20^oN-80^oN and 100^oW-40^oE for (a) dry winters, (b) wet winters, and (c) difference between dry and wet winters.

The potential vorticity field (equation (10)) at 300 hPa for the dry winters and the corresponding deviations from the winter climatology are depicted in Fig. 3.74. For both winters it is quite obvious the presence of a trough in the potential vorticity pattern in the region of the geopotential ridge and vice-versa, both in clear phase opposition as expected. The strong meridional gradient of this field is noteworthy (Fig. 3.74(a)), as well as the strong mean negative anomaly over the North Atlantic within the range 45^oN-55^oN (Fig. 3.74(b)), which is a clear manifestation of the anomalously enhanced ridge observed in dry winters.

The advection of potential vorticity shows much higher values and much smoother patters at 300 hPa, than at 700 hPa (not shown). Overall, these patterns are in clear accordance with the location of the ridges and troughs in the mean flow. Positive values are observed downstream of a trough and negative downstream of a ridge.

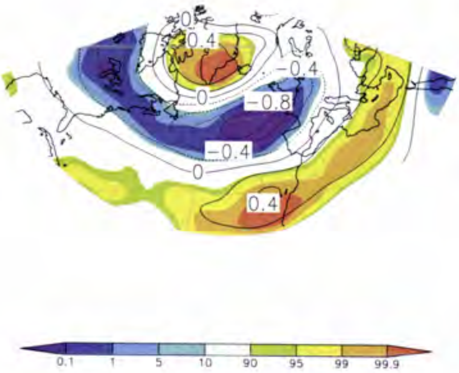

Figure 3.75: Difference of the potential vorticity between dry and wet winters (contours) in 10^{-4} s^{-1} at 300 hPa and the corresponding p-values of the Student's t-test (shading) in the North Atlantic sector between 20^oN-80^oN and 100^oW-40^oE.

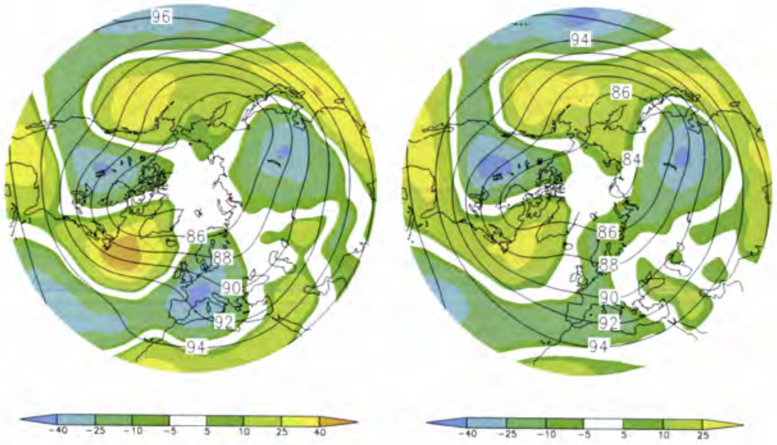

(a) (b)

Figure 3.76: Winter composite of the potential vorticity advection (shading) in 10^{-10} s^{-1} at 300 hPa and the corresponding mean geopotential field (contours) in 10^2 gpm in the North Atlantic sector between 20^oN-80^oN for (a) dry winters, and (b) wet winters.

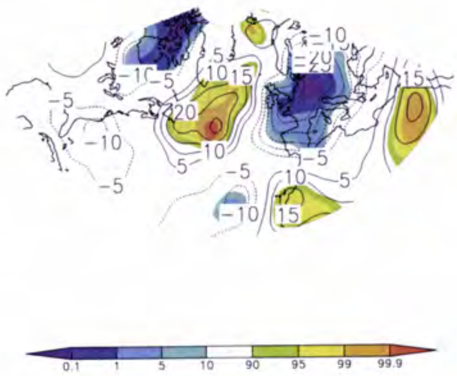

Figure 3.77: Difference of the potential vorticity advection between dry and wet winters (contours) in 10^{-10} s^{-1} at 300 hPa and the corresponding p-values of the Student's t-test (shading) in the North Atlantic sector between 20^oN-80^oN and 100^oW-40^oE.

For the dry winters (Fig. 3.76(a)) the two main maximum potential vorticity advection centers (one positive over the western North Atlantic and another negative over the eastern North Atlantic and Europe) are particular weakened. It is also apparent in both winters a three wave number pattern, as well as additional changes in the related wave-train. The winter differences of the potential vorticity advection are also distinct (Fig. 3.77). In the North Atlantic two major statistical significant cores of opposite signals can be observed. One positive core southward of Greenland, and another negative northeast of the Iberian Peninsula. Moreover, following a latitude circle in the sub-polar regions, it is evident the sequence between cores of opposite signals.

3.3 Empirical Forcing Function: A Case Study

The temporal mean state of the atmosphere can be regarded as a response to a forced regime, that is conditioned by several factors, such as topography, solar and terrestrial radiation, latent heat release, momentum transports, among others. These features lead to the distribution of the transient perturbations that act as sources and sinks of enthalpy and momentum. Moreover, the dual effect produced on the stationary flow by these transient motions, tend to accelerate the mean zonal flow in areas of convergence of the transient eddy flux of zonal momentum, whereas the transient eddy fluxes of enthalpy attenuate the local temperature gradient [Holopainen et al., 1982]. Together they influence the general circulation of the atmosphere and in an indirect way the forced regime of atmospheric circulation. They also represent the effects of the asymmetric horizontal transports of momentum and latent heat, by large-scale transient eddies.

It can be shown that for quasi-geostrophic motions (using the quasi-geostrophic approximation) the potential vorticity is materially conserved [Holton, 2004], which means that the local tendency of potential vorticity is exactly balanced by its advection, e.g., positive (negative) advections result in positive (negative) tendencies of the same value. In this manner, within the framework presented in chapter two, the superposition of the geopotential field with the potential vorticity field allows a complete diagnosis of the tendency of the potential vorticity. However, this theory is often an oversimplification of the actual atmospheric flow, as can be seen from equation (2.41), where the tendency is actually the combined result of the advection of potential vorticity and the total forcing (EFF). This forcing function is itself a combination of different physical processes. Since the fifth EFF component (friction) cannot be calculated with the available data, the EFF is here only the sum of the remaining six components [Andrade et al., 2010].

3.3.1 The first and second components of the EFF

The patterns of the first EFF component, associated to friction and diabatic heating, can be interpreted as temperatures tendencies associated with eddy transports. The cross sections of the first EFF component, over the selected Euro-Atlantic sector (80^oW-20^oE) depict significant forcing values both at low ($1000-500$ hPa) and high tropospheric levels ($500-300$ hPa). However near the surface the forcing values tend to have one order of magnitude higher than at 300 hPa. The high values of the low tropospheric forcing can be associated to the presence of very strong divergences (convergences) due to diabatic processes, which in turn tend to reinforce (attenuate) local asymmetric potential vorticity.

The vertically-averaged pattern of the first EFF component, depicts at high tropospheric levels ($500-300$ hPa) positive values over the western part of the North Atlantic (Fig. 3.79) contrasting with negative values on its eastern portion. This east-west dipolar structure is more intense during the dry winters (Fig. 3.79(a)) when compared with the wet ones (Fig. 3.79(b)) and even with the winter climatology (Fig. 3.79(c)). This characteristic can also be observed on the difference pattern (Fig. 3.79(d)), which is statistically significant northwestward the Iberian Peninsula around 20^oW (Fig. 3.81(a)).

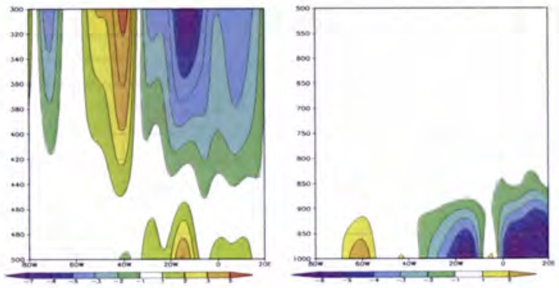

(a) (b)

Figure 3.78: Zonal cross-sections of the difference of the meridional-mean (35^{o}N-50^{o}N) of the first EFF component pattern between dry and wet winters for the North Atlantic between 80^{o}W-20^{o}E at (a) 500 – 300 hPa in 10^{-10} s^{-2}, and at (b) 1000 – 500 hPa in 10^{-9} s^{-2}.

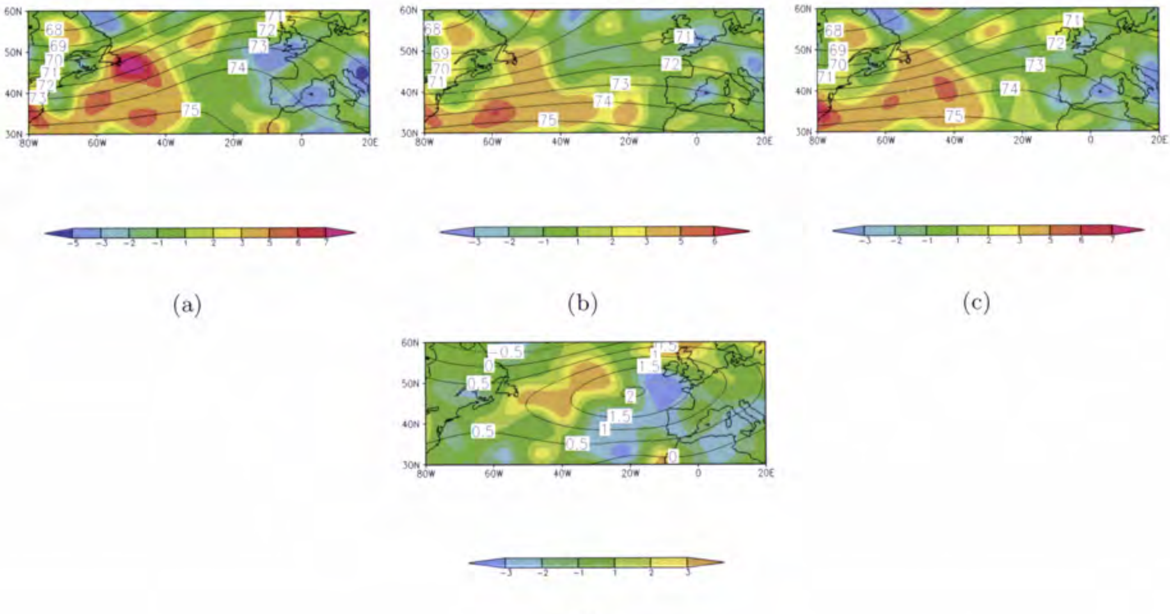

(a) (b) (c)

(d)

Figure 3.79: Vertically-averaged (500 – 300 hPa) first EFF component (shading)in 10^{-10} s^{-2} and the corresponding mean geopotential field (contours) in 10^2 gpm in the North Atlantic between 30^{o}N-60^{o}N and 80^{o}W-20^{o}E for (a) dry winters (b) wet winters (c) winter climatology, and (d) difference between dry and wet winters.

Although one order of magnitude higher, the vertically-averaged pattern of the first EFF at lower tropospheric levels (1000 – 500 hPa) shows a more smoother pattern (Fig. 3.80). In general the forcing values are more intense north of 50^{o}N as well as over western Europe, where a significant region of negative values can be observed. An area of maxima can be seen over the Alpes during dry winters (Fig. 3.80(a)) a well known area of ciclogenesis. The differences between dry and wet winters are also statistically meaningful over Europe (Fig. 3.81(b)).

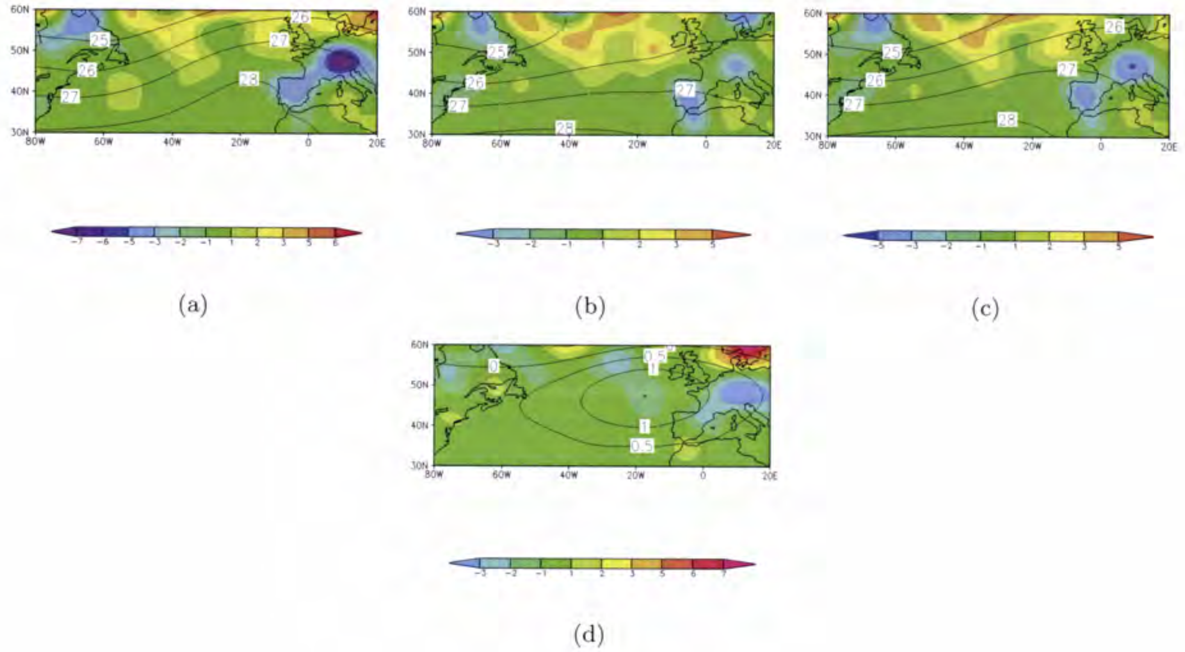

(a) (b) (c)

(d)

Figure 3.80: Vertically-averaged ($1000 - 500$ hPa) first EFF component (shading) in 10^{-9} s^{-2} and the corresponding mean geopotential field (contours) in 10^2 gpm in the North Atlantic between 30^{o}N-60^{o}N and 80^{o}W-20^{o}E for (a) dry winters (b) wet winters (c) winter climatology, and (d) difference between dry and wet winters.

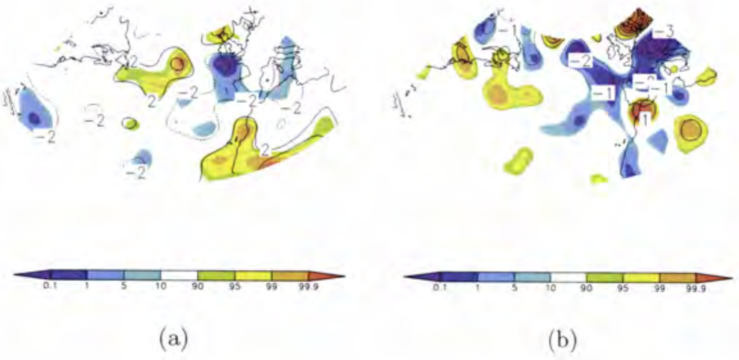

(a) (b)

Figure 3.81: Difference of the vertically-averaged first EFF component between dry and wet winters (contours) at (a) $500 - 300$ hPa in 10^{-10} s^{-2}, and at (b) $1000 - 500$ hPa in 10^{-9} s^{-2} and the corresponding p-values of the Student's t-test (shading) in the North Atlantic between 30^{o}N-60^{o}N and 80^{o}W-20^{o}E.

The cross-sections of the second EFF component, associated to latent heat release, display significant forcing values near the surface, which tend to be one order of magnitude higher than at high tropospheric levels ($500 - 300$ hPa). Those high values at the surface are coherent with the release of latent heat (Fig. 3.82(b)), and are also coherent in the higher troposphere with the phase transitions of the water substance namely its condensation (Fig. 3.82(a)).

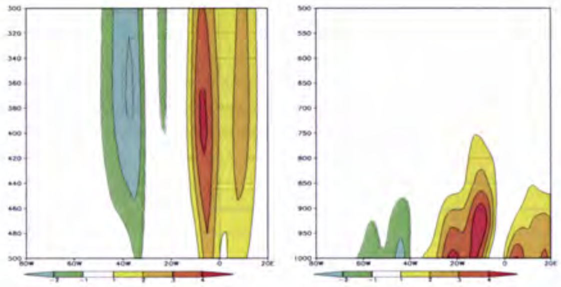

(a) (b)

Figure 3.82: Zonal cross-sections of the difference of the meridional-mean (35^{o}N-50^{o}N) of the second EFF component pattern between dry and wet winters in the North Atlantic between 80^{o}W-20^{o}E at (a) $500 - 300$ hPa in 10^{-11} s^{-2}, and at (b) $1000 - 500$ hPa layer in 10^{-10} s^{-2}.

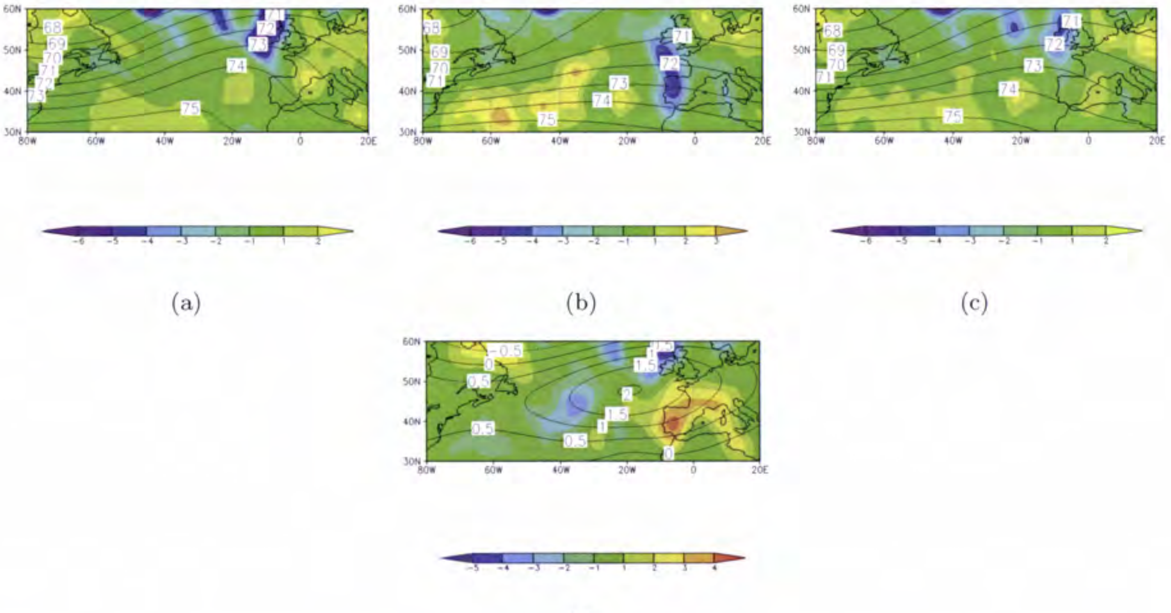

(a) (b) (c)

(d)

Figure 3.83: Vertically-averaged ($500 - 300$ hPa) second EFF component (shading) in 10^{-11} s^{-2} and the corresponding mean geopotential field (contours) in 10^2 gpm in the North Atlantic between 30^{o}N-60^{o}N and 80^{o}W-20^{o}E for (a) dry winters (b) wet winters (c) winter climatology, and (d) difference between dry and wet winters.

For the higher tropospheric levels the pattern of both dry winters (Fig. 3.83(a)) and winter climatology (Fig. 3.83(c)) are highly smoothed between 30^{o}N-50^{o}N contrasting with the wet winters where a west-east dipolar structure can be observed. Although weak positive forcing values are observed in the North Atlantic a negative centre can be observed over the Iberian Peninsula (Fig. 3.83(b)). In this region the difference between dry and wet winters are statistically meaningful (Fig. 3.83(d), 3.84). These results suggest the relevance of latent heating in the mean potential vorticity budget, since the centres of maxima are observed in the storm track maxima region (Fig. 3.16(b)) and are also supported by the results attained by Black [1998].

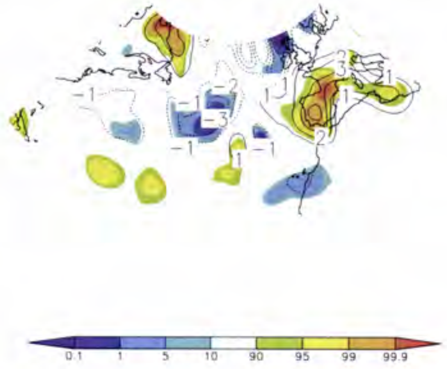

Figure 3.84: Difference of the vertically-averaged (500 – 300 hPa) second EFF component between dry and wet winters (contours) in 10^{-11} s^{-2}, and the corresponding p-values of the Student's t-test (shading) in the North Atlantic between 30°N-60°N and 80°W-20°E.

In general, in the higher troposphere the forcing values of the first EFF are one order of magnitude higher than the values of the second EFF over the North Atlantic. The locations of the maxima forcing values are relevant. The previous results are corroborated by the results after Hoskins and Valdes [1990], we can state that for the Northern Hemisphere the mean diabatic heating values and their locations are the most important factor controlling storm track locations. Moreover the large-scale latent heat release acts to enhance individual weather systems.

3.3.2 The third and fourth components of the EFF

The study of the atmospheric flow made by Saltzman [1962], aimed at assessing the contributions of the eddy transports of both heat and momentum eddy transports to the time-mean budget of the potential vorticity. In the present study, this methodology is undertaken and each contribution is evaluated separately.

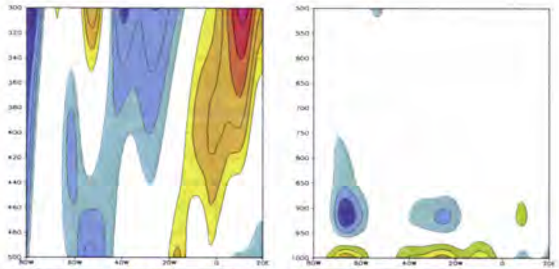

(a) (b)

Figure 3.85: Zonal cross-sections of the difference of the meridional-mean (35°N-50°N) of the third EFF component pattern between dry and wet winters in the North Atlantic between 80°W-20°E at (a) 500 – 300 hPa in 10^{-11} s^{-2}, and at (b) 1000 – 500 hPa in 10^{-11} s^{-2}.

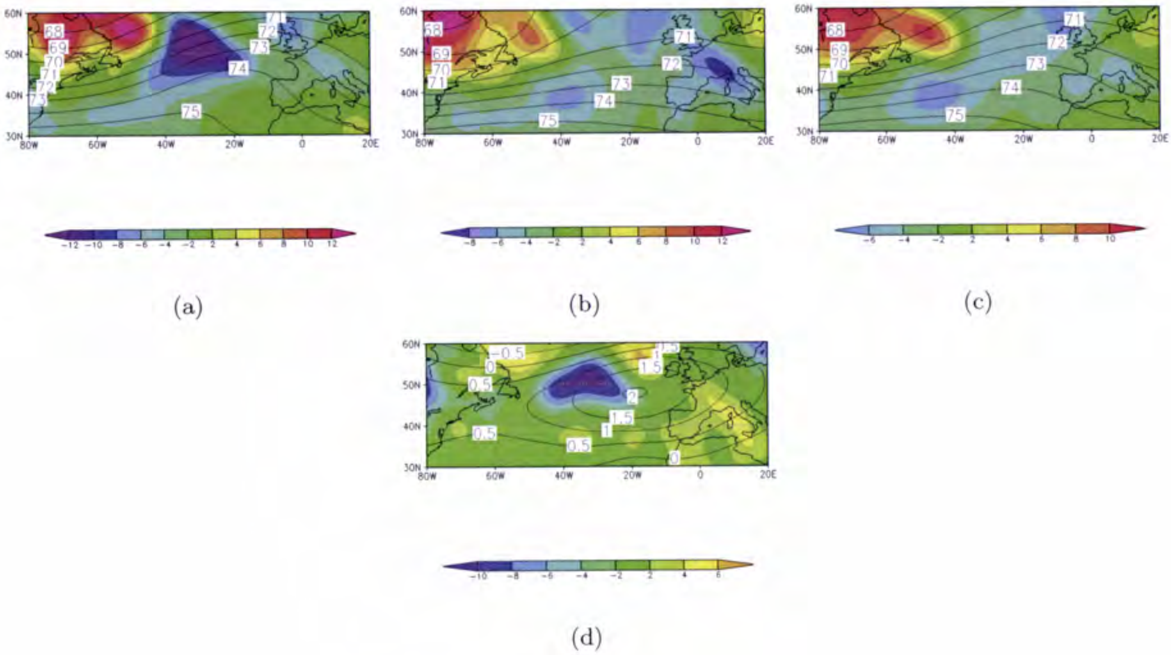

(a) (b) (c)

(d)

Figure 3.86: Vertically-averaged (500 − 300 hPa) third EFF component (shading) in 10^{-11} s^{-2} and the corresponding mean geopotential field (contours) in 10^2 gpm in the North Atlantic between 30°N-60°N and 80°W-20°E for (a) dry winters (b) wet winters (c) winter climatology, and (d) difference between dry and wet winters.

The zonal cross-sections of the third EFF component, associated to the differential divergence of the horizontal transient-eddy transports of enthalpy, depict at both lower and higher tropospheric levels, values of the same order of magnitude. However, a detailed observation of Fig. 3.85 reveals that the forcing values in the higher troposphere (500 − 300 hPa) are more intense. This suggests the importance of the forcings due to the transient transports of enthalpy to the establishment of dynamical anomalies in the atmospheric flow.

The vertically averaged third EFF component displays physically meaningful patterns at both low and high tropospheric levels for the dry winters (Fig. 3.86(a), 3.87(a)). In fact, the source of anticyclonic potential vorticity over the North Atlantic is noteworthy. The stronger values in the positive and negative centres of maxima, highly contrasts with those observed for the wet winters and also the winter climatology. As noted before, this fact can be observed not only in the lower troposphere (1000 − 500 hPa), but also at higher tropospheric levels (500 − 300 hPa). It is clearly coherent with the development of the anomalously strong ridges that prevail during severe precipitation deficits over the Western Iberia.

The analysis of the fourth EFF component, associated with the differential divergence of the vertical transient-eddy transports of enthalpy, reveals that aloft (500 − 300 hPa) the forcing values are one order of magnitude lower than the previous EFF components values. It can also be noted that its vertically averaged pattern is highly smoothed and thus not reveal meaningful forcing centres. In this way, in a first approximation, the fourth EFF component can be neglected in the estimation of the EFF.

Although the values of the third and fourth EFF components are of the same order of

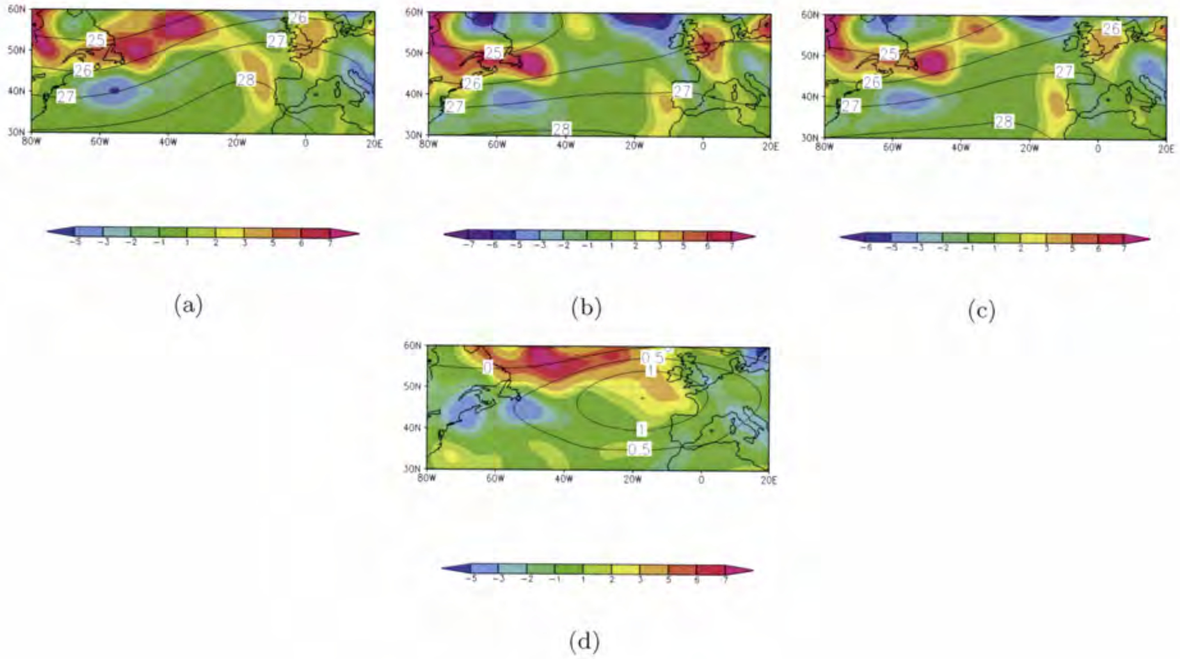

(a) (b) (c)

(d)

Figure 3.87: Vertically-averaged (1000 − 500 hPa) third EFF component (shading) in 10^{-11} s^{-2} and the corresponding mean geopotential field (contours) in 10^2 gpm in the North Atlantic between 30^{o}N-60^{o}N and 80^{o}W-20^{o}E for (a) dry winters (b) wet winters (c) winter climatology, and (d) difference between dry and wet winters.

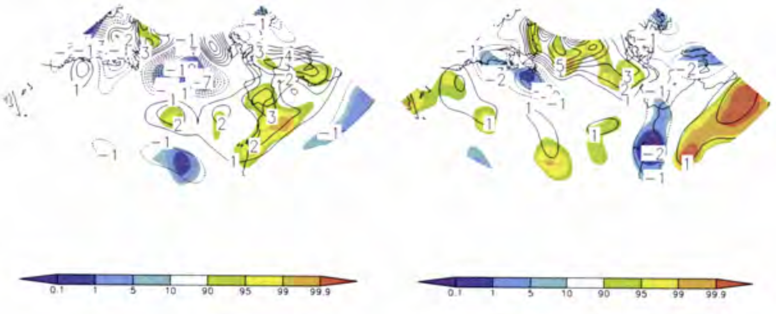

(a) (b)

Figure 3.88: Difference of the vertically-averaged third EFF component between dry and wet winters (contours) at (a) $500 - 300$ hPa in 10^{-11} s^{-2}, and at (b) $1000 - 500$ hPa in 10^{-11} s^{-2} and the corresponding p-values of the Student's t-test (shading) in the North Atlantic between 30^{o}N-60^{o}N and 80^{o}W-20^{o}E.

magnitude in the higher troposphere, the magnitude of the forcing centres is smaller for the vertical transient-eddy transports of enthalpy. In fact, the forcing is consistent with the trough-ridge locations characterized in previous subsections.

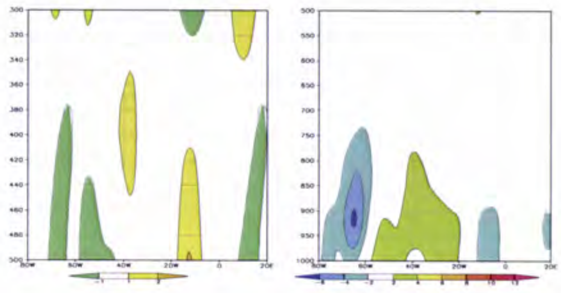

(a) (b)

Figure 3.89: Zonal cross-sections of the difference of the meridional-mean (35^{o}N-50^{o}N) of the fourth EFF component pattern between dry and wet winters in the North Atlantic between 80^{o}W-20^{o}E at (a) $500 - 300$ hPa in 10^{-12} s^{-2}, and at (b) $1000 - 500$ hPa in 10^{-11} s^{-2}.

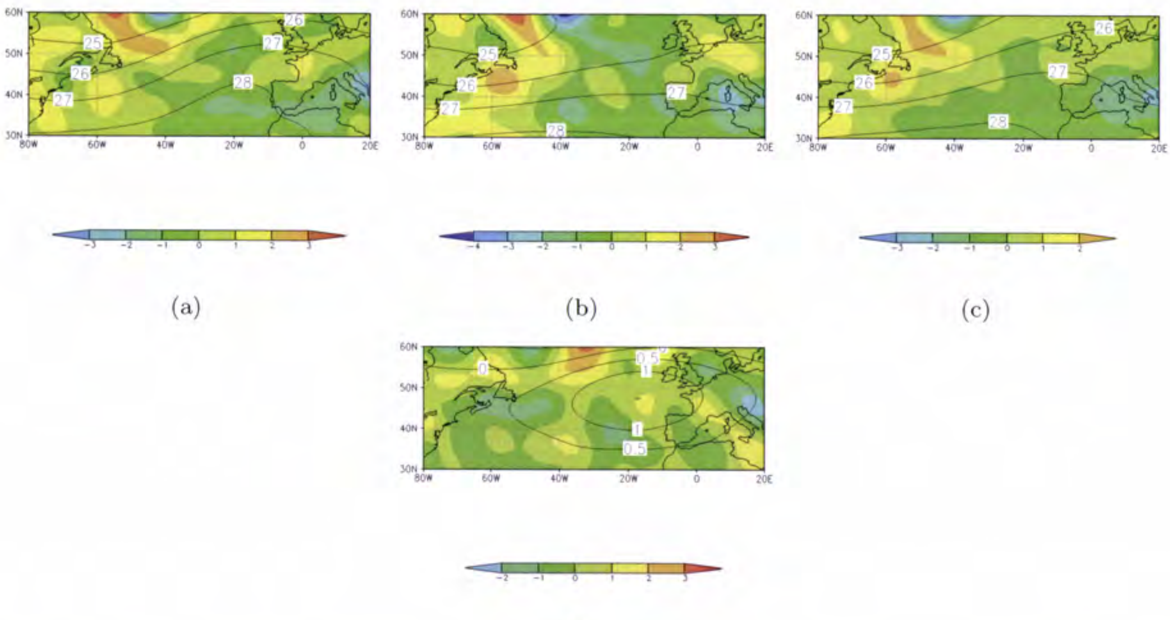

(a) (b) (c)

(d)

Figure 3.90: Vertically-averaged ($500 - 300$ hPa) fourth EFF component (shading) in 10^{-11} s^{-2} and the corresponding mean geopotential field (contours) in 10^2 gpm in the North Atlantic between 30^{o}N-60^{o}N and 80^{o}W-20^{o}E for (a) dry winters (b) wet winters (c) winter climatology, and (d) difference between dry and wet winters.

3.3.3 The sixth and seventh components of the EFF

The zonal cross-sections of the sixth EFF component (Fig. 3.91), associated with the eddy horizontal transports of momentum, for the lower and higher troposphere have the same order of magnitude. However, an additional apparent source of eddy activity is located in the upper troposphere (Fig. 3.91(a)). These maxima centres are located in the preferred positions of the jet stream. The comparison between the third and sixth components reveals that the magnitude of the third component is generally larger than the sixth, mainly at higher levels. Furthermore, between 20^{o}W and 20^{o}E, a certain degree of cancellation can be observed throughout the higher troposphere.

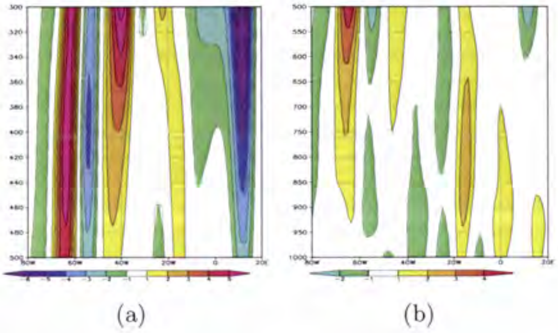
(a) (b)

Figure 3.91: Zonal cross-sections of the difference of the meridional-mean (35^{o}N-50^{o}N) of the sixth EFF component pattern between dry and wet winters in the North Atlantic between 80^{o}W-20^{o}E at (a) $500-300$ hPa in 10^{-11} s^{-2}, and at (b) $1000-500$ hPa in 10^{-11} s^{-2}.

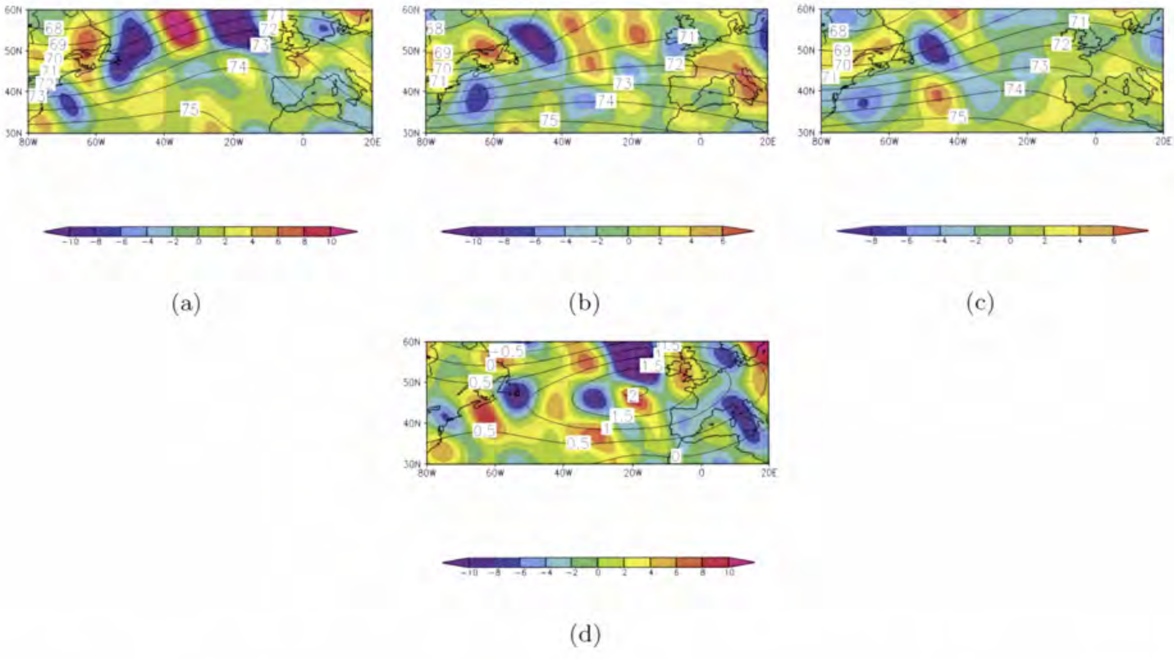
(a) (b) (c)

(d)

Figure 3.92: Vertically-averaged ($500-300$ hPa) sixth EFF component (shading) in 10^{-11} s^{-2} and the corresponding mean geopotential field (contours) in 10^2 gpm in the North Atlantic between 30^{o}N-60^{o}N and 80^{o}W-20^{o}E for (a) dry winters (b) wet winters (c) winter climatology, and (d) difference between dry and wet winters.

In the sixth EFF component for the dry winters, there is a very pronounced sequence of strong forcing cores along the northern border of the ridge (Fig. 3.92(a)). In fact, these

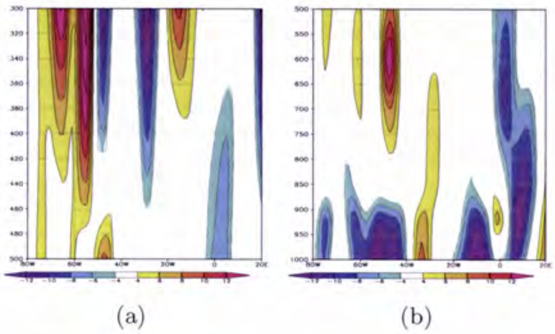

(a) (b)

Figure 3.93: Zonal cross-sections of the difference in the meridional-mean (35^oN-50^oN) of the seventh EFF component pattern between dry and wet winters in the North Atlantic between 80^oW-20^oE at (a) $500 - 300$ hPa in 10^{-12} s^{-2}, and at (b) $1000 - 500$ hPa in 10^{-12} s^{-2}.

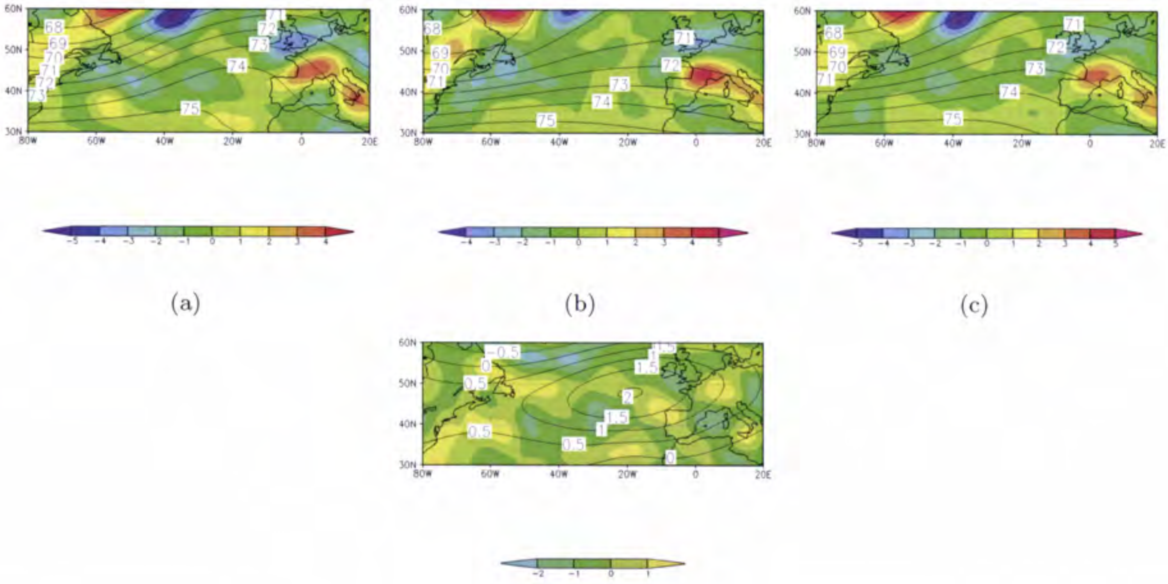

(a) (b) (c)

(d)

Figure 3.94: Vertically-averaged ($500 - 300$ hPa) seventh EFF component (shading) in 10^{-12} s^{-2} and the corresponding mean geopotential field (contours) in 10^2 gpm in the North Atlantic between 30^oN-60^oN and 80^oW-20^oE for (a) dry winters (b) wet winters (c) winter climatology, and (d) difference between dry and wet winters.

forcing cores play an important role in aligning the eddy-driven polar jet and the storm track along their maxima by generating a sequence of positive and negative asymmetric potential vorticity anomalies. The transient transports of both enthalpy and momentum at higher tropospheric levels are thus shown to be essential for the development of the large-scale asymmetric anomalies of potential vorticity over the North Atlantic. The outcomes of this case study clearly highlight the relevance of the EFF in diagnosing large-scale anomalies and understanding their underlying physical mechanisms.

The analysis of the zonal cross-sections of the seventh EFF component (Fig. 3.93), associated with the differential divergence of the vertical transient-eddy transports of momentum, reveals that these transports are of the same order of magnitude throughout the troposphere. However, when compared with the values of the other components, are one order of magnitude lower than the second, third and sixth EFF components, and two orders of magnitude lower than the first EFF component. The vertically-averaged pattern (Fig. 3.94) is rather smooth, and no major differences can be observed between dry and wet winters (Fig. 3.94(d)). As a result, in a first approximation the seventh EFF component can be neglected in the estimation of the EFF.

3.3.4 The Empirical Forcing Function

Due to the relevance of the latent heat release and the transient eddy transports of enthalpy and momentum in atmospheric dynamics, the composed fields of the second, third and sixth EFF components is formed and analysed.

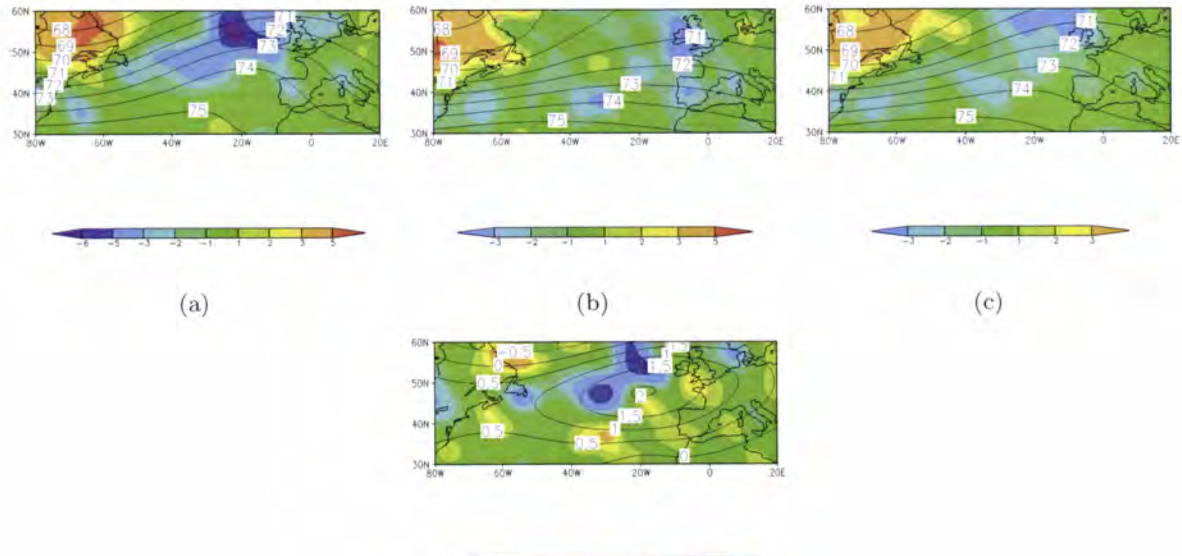

(a) (b) (c)

(d)

Figure 3.95: Vertically-averaged $(500-300\ \mathrm{hPa})$ sum of second, third and sixth EFF component (shading) in $10^{-11}\ \mathrm{s}^{-2}$ and the corresponding mean geopotential field (contours) in 10^2 gpm in the North Atlantic between 30°N-60°N and 80°W-20°E for (a) dry winters (b) wet winters (c) winter climatology, and (d) difference between dry and wet winters.

In the higher troposphere (Fig. 3.95), a centre of positive values, associated with cyclonic potential vorticity, is depicted in the trough, whereas a centre of negative values, associated with anticyclonic potential vorticity, is found on the ridge. These forcing centres are more intense during the dry winters (Fig. 3.95(a)). This result is plainly coherent with the presence and maintenance of a strong North Atlantic ridge. Thus at higher tropospheric levels, the second, third and fourth EFF components document the importance of the latent heat release, and of the transient enthalpy and momentum transports in the maintenance of the asymmetric flow.

In the lower troposphere for the dry winters (Fig. 3.96(a)) a negative centre is found upstream of the ridge, whereas a strong positive nuclei can be observed downstream. These results indicate the importance of the forcing on lower tropospheric levels in order to maintain the strong ridge aloft. For the wet winters (Fig. 3.96(b)) and for the winter climatologies (Fig. 3.96(c)) the forcing values are much smoother, as can be confirmed by the difference pattern (Fig. 3.96(d)) mainly over the Iberian Peninsula.

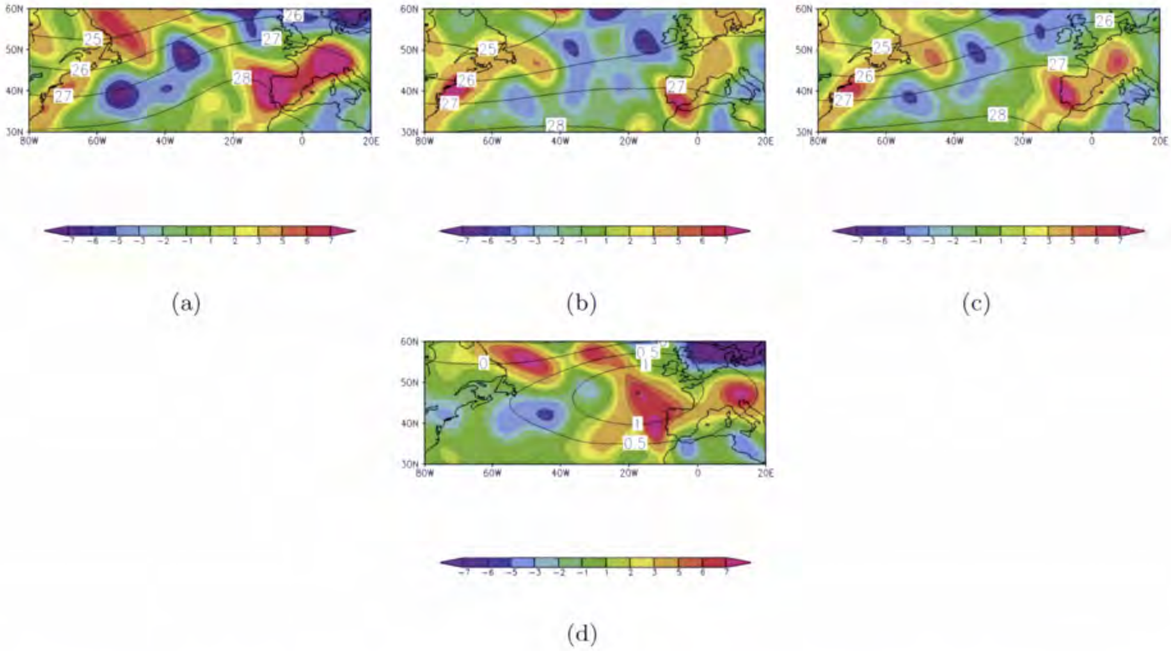

(a)

(b)

(c)

(d)

Figure 3.96: Vertically-averaged (1000 – 500 hPa) sum of second, third and sixth EFF component (shading) in 10^{-11} s^{-2} and the corresponding mean geopotential field (contours) in 10^2 gpm in the North Atlantic between 30^oN-60^oN and 80^oW-20^oE for (a) dry winters (b) wet winters (c) winter climatology, and (d) difference between dry and wet winters.

The zonal cross-sections of the mean-meridional EFF over the selected Euro-Atlantic sector (80^oW-20^oE) show significant forcing values both at low (1000 – 500 hPa) and high tropospheric levels (500 – 300 hPa), though the near-surface forcing tends to have values one order of magnitude higher than at 300 hPa (Fig. 3.97). The high values of the low tropospheric forcing are coherent with the presence of very strong divergences (convergences) at these levels due to diabatic processes that act as important factors in maintaining stationary-eddy potential vorticity. However, the cross-sections of the individual EFF components reveal that the first component (Fig. 3.78), which is associated with all diabatic heating processes but latent heat release, is the leading component not only at low tropospheric levels, but also in

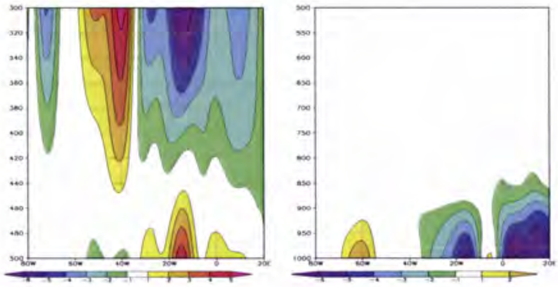

(a) (b)

Figure 3.97: Zonal cross-sections of the difference of the meridional-mean (35^oN-50^oN) of the EFF pattern between dry and wet winters in the North Atlantic between 80^oW-20^oE at (a) $500 - 300$ hPa in 10^{-10} s^{-2}, and at (b) $1000 - 500$ hPa in 10^{-9} s^{-2}.

the upper troposphere, with values at least one order of magnitude larger than the other EFF components [Andrade et al., 2009a, b]. Hence, the EFF pattern mainly reflects the rate of total heat addition and therefore, as a first approximation, it can be estimated using only the first EFF component defined by (2.43).

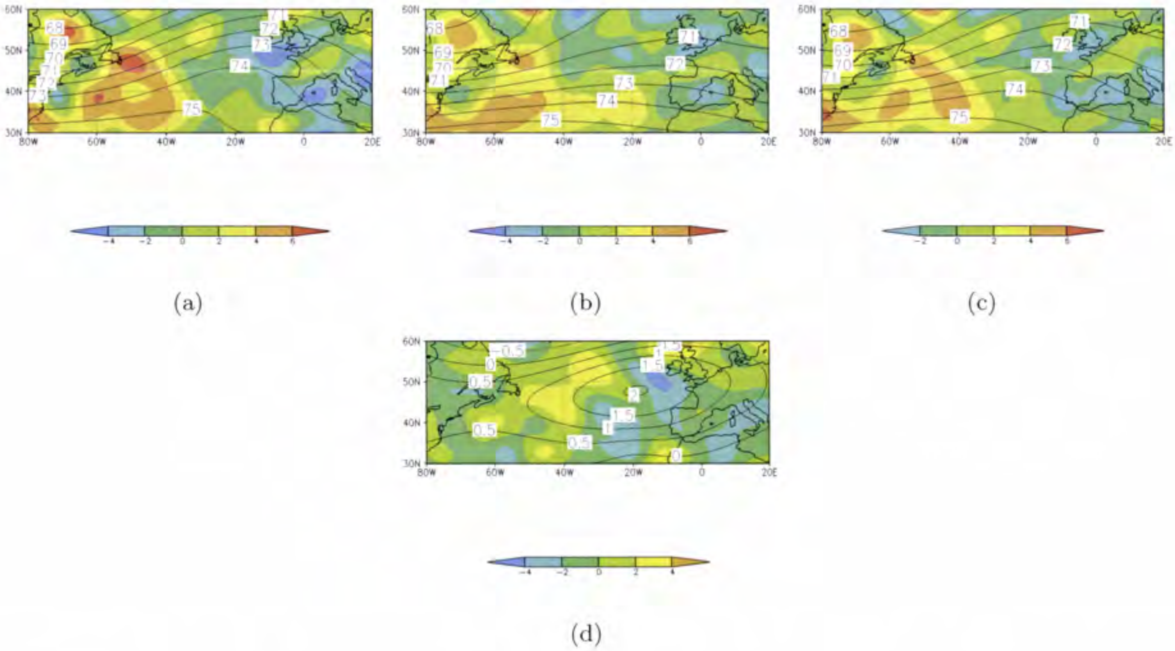

(a) (b) (c)

(d)

Figure 3.98: Vertically-averaged ($500 - 300$ hPa) EFF (shading) in 10^{-10} s^{-2} and the corresponding mean geopotential field (contours) in 10^2 gpm in the North Atlantic between 30^oN-60^oN and 80^oW-20^oE for (a) dry winters (b) wet winters (c) winter climatology, and (d) difference between dry and wet winters.

The vertically-averaged ($500 - 300$ hPa) EFF pattern for the dry winters reveals an east-

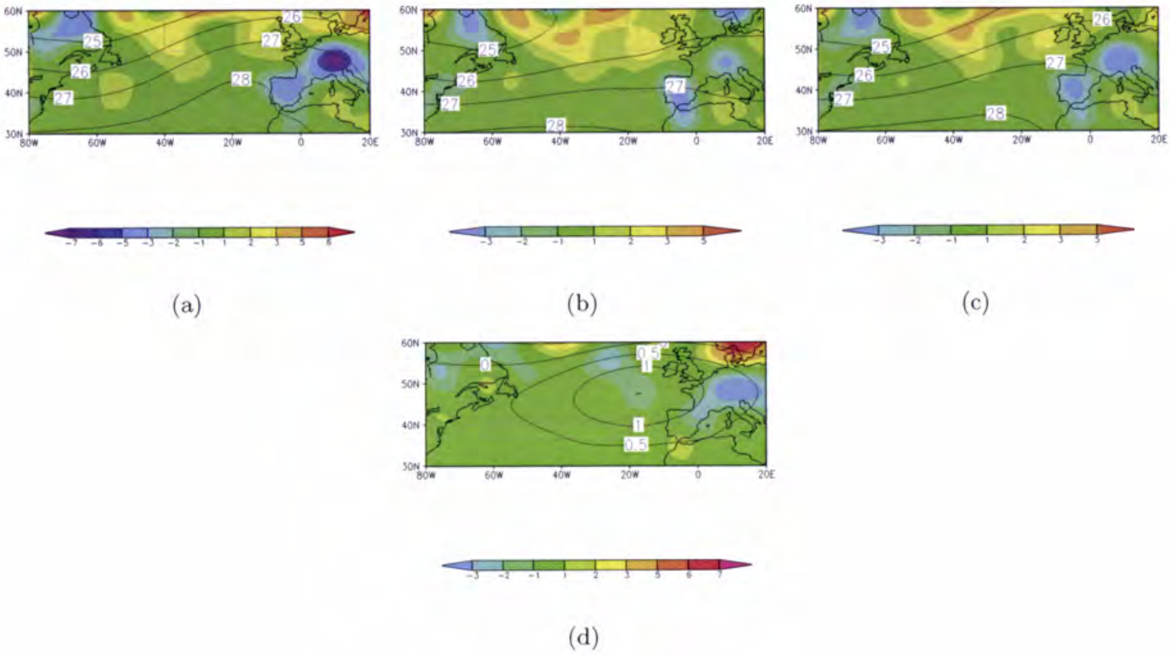

(a) (b) (c)

(d)

Figure 3.99: Vertically-averaged (1000 − 500 hPa) EFF (shading) in 10^{-9} s^{-2} and the corresponding mean geopotential field (contours) in 10^2 gpm in the North Atlantic between 30°N-60°N and 80°W-20°E for (a) dry winters (b) wet winters (c) winter climatology, and (d) difference between dry and wet winters.

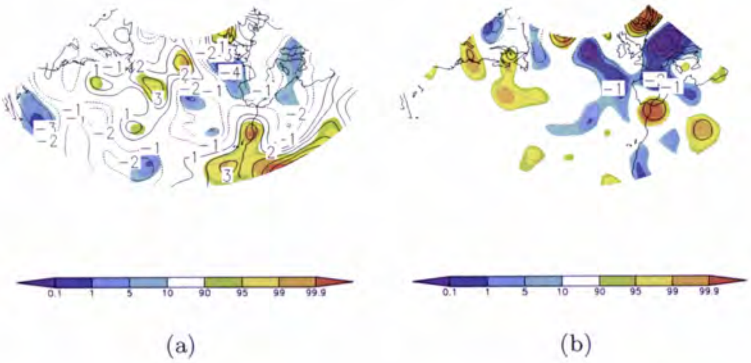

(a) (b)

Figure 3.100: Difference of the vertically-averaged EFF between dry and wet winters (contours) at (a) 500 − 300 hPa in 10^{-10} s^{-2}, and at (b) 1000 − 500 hPa in 10^{-9} s^{-2}, and the corresponding p-values of the Student's t-test (shading) in the North Atlantic between 30°N-60°N and 80°W-20°E.

west dipolar structure over the North Atlantic (Fig. 3.98(a)), with essentially positive values westward of 40°W and negative values eastward. This pattern thus supports with the presence of a strong North Atlantic ridge during the selected winters, since the stationary-eddy cyclonic potential vorticity (positive EFF values) tends to be associated with geopotential troughs, while the stationary-eddy anticyclonic potential vorticity (negative EFF values) tends to be associated with geopotential ridges.

In the lower troposphere the vertically-averaged EFF pattern is very smooth, particularly south of 40^{o}N. However, for the dry winters (Fig. 3.99(a)), at high latitudes, positive values can be observed upstream of the ridge and negative downstream. Moreover, it is worthwhile mentioning that these forcing values, are statistically meaningful (Fig. 3.100(b)). For the wet winters (Fig. 3.99(b)) and winter climatologies (Fig. 3.99(c)) the patterns do not show any major forcing extremes.

Despite the leading role of the first component in maintaining the stationary-eddy potential vorticity, the second component, associated to latent heat release, is also important at low tropospheric levels, where humidity is concentrated . Conversely, at higher tropospheric levels, the third and sixth components acquire a (relatively) higher relevance, documenting the relevance of the transient enthalpy and momentum transports in the maintenance of the stationary-eddy flow. These results are in agreement with previous results using the Eliassen-Palm fluxes [c.f., Fig. 9, Santos et al., 2009b].

Chapter 4

Discussion and Conclusions

The occurrence of severe precipitation deficits over the western portion of the Iberian Peninsula is due to the lack of rainfall during the winter season. Winter precipitation is mainly related to disturbed patterns in the North Atlantic large-scale atmospheric flow. A well defined ridge over the Northern Atlantic is observed in the geopotential mean height field for dry winters, both at 500 and 300 hPa, whereas for the wet ones the prevailing pattern is almost zonal. This result is also supported by the difference field in the potential vorticity. The near vertical tilt in the maximum anomaly axis of the zonal-mean geopotential height for dry winters suggests that the ridge has a nearly equivalent barotropic structure. The presence of a strong warm-core ridge westward of Iberia, is clearly unfavourable to rain generation over western Iberia. This enhanced ridge blocks the propagation of the weather systems, leading to a northward deflection of the storm track over the Eastern North Atlantic. The pattern of the storm track anomalies displays a dipolar structure, similar to the NAO, however displaced northeastward. The EOF analysis of the mean geopotential height field also suggests the relevance of the NAO during the dry winters. Conversely, cyclonic activity seems to be more relevant for the wet winters near the Iberian Peninsula.

The aforementioned ridge with equivalent barotropic warm-core leads not only to an enhancement of the large-scale stationary wave pattern, but also to a clear differentiation between the subtropical and polar jets. Indeed, the mid-latitude westerly jet suffers an important difluence just eastward of North America and the sub-polar jet presents a significant tilt in its core [Santos et al., 2009b]. The transports of both enthalpy and specific humidity are displaced, for the dry winters, to the northeast. This displacement is also observed for the precipitation rate and precipitable water patterns. A nearly zonal flow is observed for the wet winters. The regions of the maximum intensity of the enthalpy transports are concentrated in the preferred locations of the storm track and the observed deviation of the humidity transports suggests the blocking of the transient systems by the intensified ridge. In fact, the splitting of the subtropical jet stream into two branches corresponds to an intensification of the meridional component of the mid-tropospheric circulation. Moreover, this intensification is usually accompanied by a blocking located in the vicinity of the British Isles [Barriopedro et al., 2006]. The transports of zonal momentum are plainly coherent with the presence of an enhanced North Atlantic ridge for the dry winters, whereas for the wet winter the flow pattern is almost zonal. It is also worth emphasizing the intensification of the advection of specific humidity in the western part of the Iberian Peninsula during wet winters. Overall, the disturbed flow is not only related to an enhancement (weakening) of the NAO but also to an enhancement (weakening) of the stationary eddies over the North Atlantic.

The formulation of the time-mean potential vorticity equation on isobaric surfaces (after Saltzman, 1962) is revisited in the present study. This less conventional formulation presents some attractive features. In fact, this formal development comprises a forcing term of the equation (EFF) that can be decomposed into seven additive components associated with different physical mechanisms. The role of different internal forcing mechanisms (both thermal and mechanical processes) in maintaining stationary eddies in the large-scale atmospheric motion can then be assessed.

The EFF was applied as a tool to diagnose large-scale stationary eddies associated with the occurrence of strong ridges over the Eastern North Atlantic, which are often precursors of severe droughts over Western Iberia [Andrade et al., 2010]. Results show that the EFF pattern (total forcing term) is dynamically coherent with the configuration of the geopotential height field. For such events, the EFF pattern depicts a clear dipolar structure over the North Atlantic that contributes to the maintenance of cyclonic (anticyclonic) potential vorticity upstream (downstream) of the anomalously strong ridges. The analysis of the individual components also shows that among the six calculated components (the fifth EFF component is associated to frictional effects and was not computed), the most important component throughout the troposphere is the first, which is associated with diabatic heating (latent heat excluded). Nevertheless, latent heat release (second component) can also be important at low tropospheric levels, while transient horizontal enthalpy (third component) and momentum (sixth component) fluxes are important at high tropospheric levels. When compared with the latter components, vertical fluxes are negligible throughout the troposphere (fourth and seventh components). As such, the EFF pattern can be, at a first approximation, accurately estimated by computing only the first component. At a second approximation, the estimation of the EFF pattern at low (high) troposphere can be further improved by considering the second (third and sixth) components. No significant improvements can be made when considering the remaining components. Hence, they may be discarded in future studies.

Despite the previous results, in the interpretation of the EFF patterns some considerations must be born in mind. Although several internal (both mechanical and thermal) processes are taken into account in the EFF definition, the external forcing mechanisms of the atmospheric circulation, such as topographic effects, diabatic fluxes at the lower atmospheric boundary are not incorporated in this definition. In fact, these processes can only be included as boundary conditions. Furthermore, taking into account that the EFF formulation derives from the equation of the time-mean potential vorticity over a relatively long time scale (e.g., a season), the EFF analysis only allows a diagnostic approach to the dynamical conditions, not enabling studies of generation/decay (development) of the anomalies. In fact, in this kind of analysis it can only be stated that an EFF component can contribute or not for the maintenance of a specific stationary eddy. Many previous studies have shown that transient eddies interact with the mean flow through positive and negative feedback mechanisms and cannot be considered as independent forcing entities of the atmospheric flow [e.g. Rivière, 2009].

Even taking into consideration the previous limitations of the EFF analysis, results give some evidence for considering the EFF patterns as a valuable tool in diagnosing stationary-eddy anomalies in the large-scale atmospheric motion, illustrated here for the occurrence of strong ridges over the Eastern North Atlantic. Moreover, by definition, the EFF enables the assessment of the different contributions made by internal (both mechanical and thermal) atmospheric processes in the maintenance of time-mean (e.g., seasonal mean) axially asymmetric anomalies in the atmospheric flow. This last property is a major motivation to consider the EFF patterns when analysing other large-scale atmospheric anomalies (e.g., teleconnections).

References

Andrade, C., Santos, J., and Corte-Real, J.(2007): The Empirical forcing functions for the Large-Scale mean disturbances in the atmosphere by heat and momentum transports, XXXI Reunión Bienal de la Real Sociedad de Física, Universidade de Granada, Livro de Resumos, 1, pp 200, ISBN: 978-84-690-7298-1.

Andrade, C., Santos, J.A., and Corte-Real, J.(2008a): Applications of PCA in atmospheric sciences, 17th International Workshop on Matrices and Statistics, Tomar, pp 89, ISBN:978-972-9473-37-1.

Andrade, C., Santos, J., and Corte-Real, J.(2008b): Climate-mean winters patterns associated with enthalpy, latent heat and momentum mean convergence fields due large-scale transient eddies, General Assembly 2008, Geoph. Res. Abst., Vol. 10, EGU2008-A-03343.

Andrade, C., Santos, J.A., and Corte-Real, J.(2008c): A Climatologia de referência da divergência diferencial dos transportes horizontais perturbados de entalpia e de momento linear, 6ª Assembleia Luso-Espanhola de Geodesia e Geofísica, Tomar, Livro de Resumos, 111–112.

Andrade, C., Santos, J., and Corte-Real, J.(2008d): A divergência diferencial dos transportes horizontais perturbados de entalpia e de momento linear, 6ª Assembleia Luso-Espanhola de Geodesia e Geofísica, Tomar, Livro de Resumos, 31-32.

Andrade, C., Santos, J.A., Pinto, J.G., Corte-Real, J., and Leite, S.(2009a): The diagnosis of large-scale atmospheric anomalies by the Empirical Forcing Function: A case study, International Conference on Ecohydrology and Climate Change, EcoHCC09-63, ISBN:978-972-9473-45-6.

Andrade, C., Santos, J., Pinto, J.G., and Corte-Real, J.(2009b): Dynamical mechanisms of the North Atlantic circulation in Portugal, EGU General Assembly 2009, Geoph. Res. Abst., Vol. 11, EGU2009-3687.

Andrade, C., Santos, J., Pinto, J.G., Corte-Real, J., and Leite, S.(2010): The Empirical Forcing Function as a tool for the diagnosis of the large-scale atmospheric anomalies, Ann. Geophys., 28(1), 75–87.

Arya, S. Pal(2001): Introduction to micrometeorology, International Geophysics Series, 79, 2nd ed. San Diego, Academic Press.

Basset, H. A., and Ali, A. M.(2006): Diagnostic of Cyclogenesis using Potential Vorticity, Atmosfera, 19, 4, 213–234.

Barnston, A.G., and Livezey, R.E.(1987): Classification seasonality and persistence of low-frequency atmospheric circulation patterns, Mon. Weather Rev., 115, 1083–1126.

Barriopedro, D., García-Herrera, R., Lupo, A., and Hernández, E.(2006): A Climatology of Northern Hemisphere Blocking, J. Climate, 19, 1042–1063.

Barry, R.G., and Carleton, A.M.(2001): Synoptic and dynamic climatology, Routledge, New York.

Black, R.(1998): The Maintenance of Extratropical Intraseasonal Transient Eddy Activity in the GEOS-1 Assimilated Dataset, J. Atmos. Sci., 55, 3159–3175.

Blackmon, M.L.(1976): A climatological spectral study of the 500 mb geopotential height of the Northern Hemisphere, J. Atmos. Sci., 33, 1607–1623.

Blackmon, M.L., Lee, Y.H., and Wallace, J.M.(1984a): Horizontal structure of 500 mb geopotential height fluctuations with long, intermediate and short time scales, J. Atmos. Sci., 41, 961–979.

Blackmon, M.L., Lee, Y.H., Wallace, J.M., and Hsu, H-H(1984b): Time Variation of 500 mb Geopotential Height Fluctuations with short, Medium and Long Time Scales, J. Atmos. Sci., 41, 981–991.

Blackmon, M. L., Wallace, J. M., Lau, N-C., and Mullen, S. L.(1977): An observational study of the Northern hemisphere wintertime circulation, J. Atmos. Sci., 34, 1040–1053.

Bluestein, H.B.(1993): Synoptic-Dynamic Meteorology in Middle Latitudes, Oxford University Press, Vol. II.

Chang, E.K.M., and Fu, Y.(2002): Interdecadal variations in Northern Hemisphere winter storm track intensity, J. Climate, 22, 670–688.

Chang, E.K.M.(2009): Diabatic and Orographic Forcing of Northern Winter Stationary Waves and Storm Tracks, J. Climate, 15, 642–658.

Charney, J.G.(1947): The dynamics of long waves in a baroclinе westerly current, J. Meteorol., 4, 135–163.

Chen, P., Hoerling, M., and Dole, R.(2001): The Origin of the Subtropical Anticyclones, J. Atmos. Sci., 58, 1827–1835.

Christoph, M., Ulbrich, U., and Haak, U.(1995): Faster Determination of the Intraseasonal Variability of Storm tracks Using Murakami's Recursive Filter, Mon. Weather Rev., 123, 578–581.

Corte-Real, J., Wang, X., and Zhang, X.(1995): Modes of variability in the Northern Hemisphere's mid tropospheric large-scale circulation, Theor. Appl. Climatol., 50, 133–146.

Davis, C.A., and Emanuel, K.A.(1991): Potential Vorticity Diagnostics of Cyclogenesis, Mon. Weather Rev., 119, 1929–1953.

Davis, R.E., Hayden, B.P., Gay, D.A., Phillips, W.L., and Jones, G.V.(1997): The North Atlantic Subtropical Anticyclone, J. Climate, 10, 728–744.

Dirmeyer, P.A., and Brubaker, K.L.(2006): Evidence for trends in the Northern hemisphere water cycle, Geop. Res. Lett., 33, L14712, doi:10.1029/2006GL026359.

Eady, E.T.(1949): Long waves and cyclone waves, Tellus, 1, 33–52.

Edmon, H.J., Hoskins, B.J., and McIntyre, M.E.(1980): Eliassen-Palm cross sections for the troposphere, J. Atmos. Sci., 37, 2600–2616.

Ertel, H.(1962): Monatsber. Dt. Akad. Wiss. Berlin, 4, 368–372.

Fernandez, J., Saenz, J., and Zorita, E.(2003): Analysis of wintertime atmospheric moisture transport and its variability over southern Europe in the NCEP reanalysis, Climate Research, 23, 195–215.

García-Herrera, R., Paredes, D., Trigo, R., Trigo, I., Hernández, E., Barriopedro, D., and Mendes, M.(2007): The Outstanding 2004/05 Drought in the Iberian Peninsula: Associated Atmospheric Circulation, J. Hydrometeorol., 8, 483–498.

Goodess, C.M., and Jones, P.D.(2002): Links between circulation and changes in the characteristics of the Iberian rainfall, Int. J. Climatol., 22, 1593–1615.

Hanson, C. E., Palutikof, J. P., Livermore, M. T. J., Barring, L., Bindi, M., Corte-Real, J., Duaro, R., Giannakopoulos, C., Good, P., Holt, T., Kundzewicz, Z., Leckebush, G., Moriondo, M., Radziejewski, M., Santos, J., Schlyter, P., Schwarb, M., Stjernquist, I., and Ulbrich, U.(2007): Modelling the Impact of Climate Extremes: An overview of the Project, Prudence Special Issue, Climatic Change, 81, 1, 163–177.

Hartmann, D.H.(1977): On potential vorticity and transport in the stratosphere, J. Atmos. Sci., 34, 968–977.

Holopainen, E., Ronto, L., and Lau, N.(1982): The Effect of Large-Scale Transient Eddies on the Time-mean flow in the Atmosphere, J. Atmos. Sci., 39, 1972–1984.

Holton, James R.(2004): An Introduction to Dynamic Meteorology, Elsevier.

Hoskins, B.J., McIntyre, M.E., and Robertson, A.W.(1985): On the Use of Significance of Isentropic Potential Vorticity Maps, Q. J. Roy. Meteor. Soc., 111, 470, 877–946.

Hoskins, B.J., and Valdes, P.J.(1990): On the existence of storm tracks, J. Atmos. Sci., 47, 1854–1864.

Hurrell, J.W.(1995): Decadal Trends in the North Atlantic Oscillation: Regional Temperatures and Precipitation, Science, 269, 676–679.

Jollife, I.T.(1995): Rotation of ill-defined principal components, Appl. Stat., 38, 139–147.

Jones, P.D., Jonsson, T., and Wheeler, D.(1997): Extension to the North Atlantic Oscillation using early instrumental pressure observations from Gibraltar and South-West Iceland, Int. J. Climatol., 17, 1433–1450.

Johnson, D.R.(1989): The forcing and maintenance of Global Monsoonal Circulations: An isentropic analysis, Advances in Geophysics, 31, Academic Press.

Kistler, R. and co-authors (2001): The NCEP/NCAR 50-Year Reanalysis: Monthly-Means CD-ROM and Documentation, Bull. Amer. Meteor. Soc., 82, 247–267.

Lamb, P.J., and Pepler, R.A.(1987): North Atlantic Oscillation and an application, Bull. Amer. Meteorol. Soc., 68, 1218–1225.

Lau, N., and Nath, M.(1991): Variability of the Baroclinic Transient Eddy Forcing Associated with Monthly Changes in the Midlatitude Storm Tracks, J. Atmos. Sci., 48, 2589–2613.

Lau, N.C., and Wallace, J.M.(1979): On the distribution of horizontal transports by transient eddies in the Northern Hemisphere wintertime circulation, J. Atmos. Sci., 36, 1844–1861.

Lin, Y.(1989): A Theory of Cyclogenesis forced by diabatic heating. Part I: A Quasi-geostrophic Approach, J. Atmos. Sci., 46, 19, 3015–3036.

Lolis, C.J., Metaxas, D.A. and Bartzokas, A.(2008): On the Intra-annual Variability of Atmospheric Circulation in Mediterranean Region, Int. J. Climatol., 28, 1339–1355.

Luo, D., Gong, T., and Diao, Y.(2007): Dynamics of Eddy-Driven Low-Frequency Dipole Modes. Part III: Meridional Displacement of Westerly Jet Anomalies during Two Phases of NAO, J. Atmos. Sci., 64, 9, 3232–3248.

Newell, R.E., Kidson, J.W., Vincent, D.G., and Boer, G.J.(1974): The General Circulation of the Tropical Atmosphere and Interactions with Extratropical Latitudes, Vols. 1 and 2, The MIT Press, 258–371.

Osborn, T.J., Briffa, K.R., Tett, S.F.B., Jones, P.D., and Trigo, R.M.(1999): Evaluation of the North Atlantic Oscillation as simulated by a climate model, Clim. Dyn., 15, 685–702.

Peixoto, J.P., and Oort, A.H.(1992): Physics of Climate, American Institute of Physics, New York.

Pinto, J.G., Ulbrich, U., Leckebush, G.C., Spangehl, T., Reyes, M., and Zacharias, S.(2007): Changes in storm track and cyclone activity in three SRES ensemble experiments with the ECHAM5/MPI-OM1 GCN, Clim. Dynam., 29, 195–210.

Qian, B., Corte-Real, J., and Xu, H.(2000): Is the North Atlantic Oscillation the most important atmospheric pattern for precipitation in Europe?, J. Geophy. Res., 105, 11901–11910.

Richman, M.B.(1986): Rotation of principal components, Int. J. Climatol., 6, 293–335.

Rivière, G.(2009): Effect of Latitudinal Variations in Low-Level Baroclinicity on Eddy Life Cycles and Upper-Tropospheric Wave-Breaking Processes, J. Atmos. Sci., 66, 1569–1592.

Rodríguez-Puebla, C., Encinas, E. H., and Sáenz, J.(2001): Winter Precipitation over the Iberian Peninsula and its relationship to Circulation Indices, Hydrol. Earth Syst. Sc., 5(2), 233–244.

Rodríguez-Puebla, C., Encinas, A. H., Nieto, S., and Garmendia, J.(1998): Spatial and temporal patterns of annual precipitation variability over the Iberian Peninsula, Int. J. Climatol., 18, 299–316.

Sáenz, J., Zubillaga, J., and Rodríguez-Puebla, C.(2001): Interannual Variability of Winter Precipitation in Northern Iberian Peninsula, Int. J. Climatol., 21, 1503–1513.

Salby, M., and Roger, P.(1996): Fundamentals of Atmospheric Physics, Elsevier, Academic Press.

Saltzman, B.(1962): Empirical Forcing Functions for the Large-Scale Mean Disturbances in the Atmosphere, Geofisica Pura e Applicata, 52, 173–188.

Santos, J., and Corte-Real, J.(2006): Temperature Extremes in Europe and Large-Scale Circulation: HadCM3 future scenarios, Clim. Res., 31, 1, 3–18.

Santos, J., Corte-Real, J., and Leite, S.(2005): Weather regimes and their connection to the winter rainfall in Portugal, Int. J. Climatol., 25, 1, 33–50.

Santos, J., and Leite, S.(2009a): Long-term variability of the temperature time series recorded at Lisbon, J. App. Stat., 36, 3, 323–337.

Santos, J., Andrade, C., Corte-Real, J., and Leite, S.(2009b): The role of large-scale eddies in the occurrence of winter precipitation deficits in Portugal, Int. J. Climatol., 29, 10, 1493–1507.

Santos, J.A., Pinto, J.G., and Ulbrich, U.(2009c): On the development of strong ridge episodes over the eastern North Atlantic, Geophys. Res. Lett., 36, L17804, doi:10.1029/2009GL039086.

Santos, J., Corte-Real, J., and Leite, S.(2007a): Atmospheric Large-scale Dynamics During the 2004–2005 Winter Drought in Portugal, Int. J. Climatol., 27, 5, 571–586.

Santos, J., Corte-Real, J., Ulbrich, U., and Palutikof, J.(2007b): European Winter Precipitation Extremes and Surface Large-Scale Circulation: a Coupled Model and its Scenarios, Theor. Appl. Climatol., 87, 1-4, 85–102.

Savijärvi, H.(1978): The Maintenance Mechanisms of Transient Large-Scale Variations in the Atmosphere. Part I: Potential Temperature and Moisture, J. Atmos. Sci., 45, 1, 29–40.

Sheridan, S.C.(2003): North American weather-type frequencies and teleconnection indices, Int. J. Climatol., 23, 27–45.

Stephenson, D.B., and Held, I.M.(1993): GCM response of northern winter stationary waves and storm tracks to increasing amounts of carbone dioxide, J. Climate, 6, 1859–1870.

Stephenson, D.B., Wanner, H., Brönnimann, S., and Luterbacher, J.(2003): The History of Scientific Research on the North Atlantic Oscillation, Geophys. Monogr., 134, Amer. Geopys. Union, 37–50.

Sutcliffe, R.C.(1947): A contribution to the problem of development. Quart. J. Roy. Meteor. Soc., 73, 370–383.

Tank, A., Wijngaard, J.B., Konnen, G.P., Bohm, R., Demaree, G., Gocheva, A., Mileta, M., Pashiardis, S., Hejkrlik, L., Kern-Hansen, C., Heino, R., Bessemoulin, P., Muller-Westermeier, G., Tzanakou, M., Szalai, S., Palsdottir, T., Fitzgerald, D., Rubin, S., Capaldo, M., Maugeri, M., Leitass, A., Bukantis, A., Aberfeld, R., Van Engelen, A. F. V., Forland, E., Mietus, M., Coelho, F., Mares, C., Razuvaev, V., Nieplova, E., Cegnar, T., Lopez, J. A., Dahlstrom, B., Moberg, A., Kirchhofer, W., Ceylan, A., Pachaliuk, O., Alexander, L. V., and Petrovic, P.(2002): Daily dataset of 20th-century surface air temperature and precipitation series for the European Climate Assessment, Int. J. Climatol., 22, 1441–1453.

Trewartha, G.T., and Horn, L.H.(1980): An Introduction to Climate, McGraw-Hill.

Treidl, R.A., Birch, E.C., and Sajecki, P.(1981): Blocking action in the Northern Hemisphere: a climatological study, Atmosphere-Ocean, 19, 1–23.

Trigo, R.M., and Da Camara, C.(2000): Circulation weather types and their influence on the precipitation regime in Portugal, Int. J. Climatol., 20, 1559–1581.

Trigo, R., Osborn, T., and Corte-Real, J.(2002): The North Atlantic Oscillation influence on Europe: climate impacts and associated physical mechanisms, Clim. Res., 20, 9–17.

Thompson, R., and Green, D.(2004): Mediterranean precipitation and its relationship with sea level pressure patterns, Ann. Geophys.-Italy, 47, 5, 1617–1633.

Ulbrich, U., and Christoph, M.(1999a): A Shift of the NAO and increasing storm track activity over Europe due to anthropogenic greenhouse gas forcing, Clim. Dynam., 15, 551–559.

Ulbrich, U., Christoph, M., Pinto, J.G., and Corte-Real, J.(1999b): Dependence of winter precipitation over Portugal on NAO and baroclinic wave activity, Int. J. Climatol. 19, 379–390.

Ulbrich, U., Pinto, J.G., Kupfer, H., Leckebusch, G.C., Spangehl, T., and Reyers, M.(2008): Changing Northern Hemisphere Storm Tracks in an Ensemble of IPCC Climate Change Simulations, J. Climate, 21, 1669–1679.

Von Storch, H., Zorita, E., and Cubasch, U.(1993): Downscaling of Global Climate Change Estimates to Regional Scales: An Application to Iberian Rainfall in Wintertime, J. Climate, 6, 1161–1171.

Wang, C.(2002): Atlantic Climate Variability and Its Associated Atmospheric Circulation Cells, J. Climate, 15, 1516–1536.

Wallace, J. M., and Gutzler, D.S.(1981): Teleconnections in the geopotential height field during the Northern Hemisphere Winter, Mon. Weather Rev., 109, 784–812.

Wallace, J.M., Lim, G. and Blackmon, M.L.(1988): Relationship between Cyclone Tracks, Anticyclone Tracks and Barocline Wave Guides J. Atmos. Sci., 45, 439–462.

Wallace, J.M., and Hobbs, P.V.(2006): Atmospheric Science: An Introductory Survey, Elsevier.

Wiin-Nielsen, A.(2003): On the Structure of Atmospheric Waves in Middle Latitudes, Atmosfera, 16, 83–102.

Wilks, D.S.(1995): Statistical methods in the atmospheric sciences: An introduction, Academic Press, USA.

WMO(1996): Climatological Normals (CLINO) for the Period 1961–1990, World Meteorological Organization Doc. WMO/OMM, 847, Geneva.

Yin, J.H.(2005): A Consistent Poleward Shift of the Storm Tracks in Simulations of 21st Century Climate, Geophys. Res. Lett., 32, L18701, In press DOI:10.1029/2005GL023684.

Zorita, E., Kharin, V., and von Storch, H.(1992): The atmospheric circulation and sea surface temperature in the North Atlantic area in winter: Their interaction and relevance for Iberian precipitation, J. Climate, 5, 1097–1108.

Index

- convergence of the transient transports of enthalpy, 33
- cyclogenesis, 56, 58

- diabatic heating, 10, 45, 56, 64
- divergence of the eddy-vertical transports of humidity, 55
- divergence of the mean eddy transports of humidity, 53

- Empirical Forcing Function, 2, 5, 6, 11, 64, 74, 80
  - EFF1, 12, 45
  - EFF2, 12, 50, 66
  - EFF3, 12, 68
  - EFF4, 12, 71
  - EFF5, 12
  - EFF6, 12, 71
  - EFF7, 12, 72
- Empirical Forcing Function,EFF1, 64
- energy conservation equation, 9
- Extratropical cyclones, 29, 58

- geopotential mean height, 24, 29

- horizontal transports of, 32
  - enthalpy, 32
  - humidity, 38
  - momentum, 35
  - specific humidity, 38
- humidity advection, 38, 41
- hydrostatic equation, 7

- jet streams, 29, 41, 44
  - sub-polar, 41
  - subtropical, 41

- kinetic energy, 37

- large-scale eddies, 1

- mean eddy-horizontal divergence of, 48
  - enthalpy, 48
- mean eddy-vertical transports of, 48
  - enthalpy, 48
- mean horizontal divergence of, 45
  - enthalpy, 45
  - humidity, 50
- mean vertical divergences transports of humidity, 52
- momentum balance equation, 6
  - meridional, 7
  - zonal, 6

- North Atlantic Oscillation, 1, 19, 21, 22
- North Atlantic ridge, 19, 24, 26, 28, 31, 34, 36, 44, 61

- omega-vertical velocity, 26

- potential temperature, 30
- precipitable water, 21
- precipitation rate, 20
- Principal Component Analysis, 16, 27
  - Empirical Orthogonal Function, 27
  - Empirical orthogonal function, 16
  - LEV diagram, 16
  - Principal components, 16

- rate of heat addition, 7, 13, 56
  - due to conduction and friction, 7
  - due to latent heat release, 7
  - per unit mass due to condensation, 12, 56
  - per unit mass due to radiation, 7

- severe precipitation deficits, 1, 14, 19, 79
- static stability, 6

storm track, 2, 16, 19, 21, 29, 32, 37, 43, 57, 67, 79

t-statistic, 16
  Student's t distribution, 16
time-mean continuity equation, 7
time-mean energy equation, 7

vertical divergence of, 48
vertical enthalpy transport of
  enthalpy, 48
Vorticity, 2, 58
  absolute vorticity, 5
  advection of potential vorticity, 61, 64
  equation of, 5
  Ertel's potential vorticity, 5
  isentropic potential vorticity, 6
  meridional gradient of absolute vorticity, 60
  planetary vorticity, 5
  potential vorticity, 2, 61, 80
  quasi-geostrophic potential vorticity, 7
  relative vorticity, 5, 59
  stationary-eddy potential vorticity, 10, 11
  stretching vorticity, 6
  time-mean potential vorticity equation, 10

water vapour continuity equation, 12, 56
weather regimes, 1
weather systems, 2
winter precipitation, 1

zonal wind, 44

SIDA